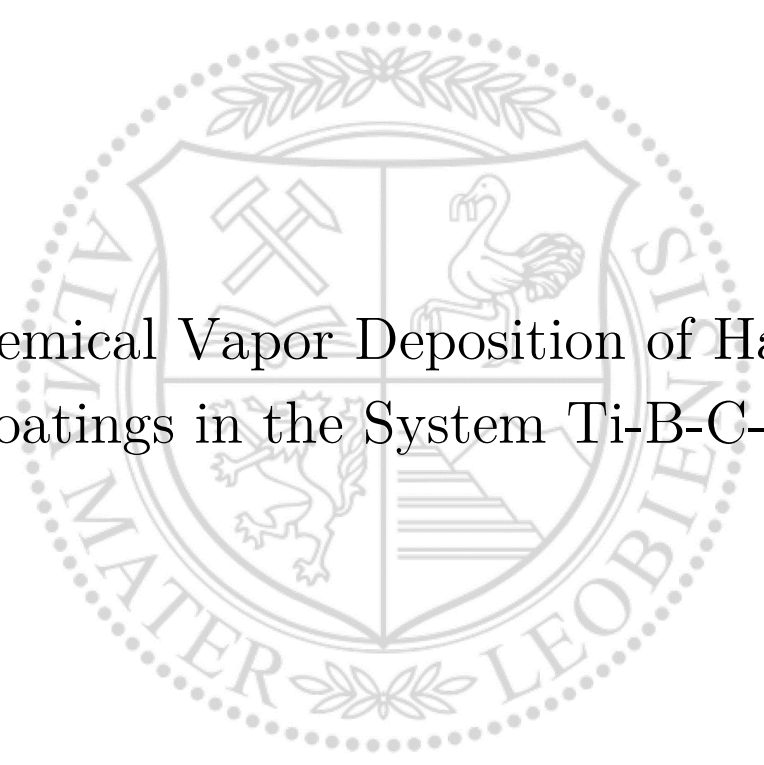




Chair of Functional Materials and Materials Systems

Doctoral Thesis



Chemical Vapor Deposition of Hard
Coatings in the System Ti-B-C-N

Dipl.-Ing. Christina Laura Kainz, BSc

June 2020

AFFIDAVIT

I declare on oath that I wrote this thesis independently, did not use other than the specified sources and aids, and did not otherwise use any unauthorized aids.

I declare that I have read, understood, and complied with the guidelines of the senate of the Montanuniversität Leoben for "Good Scientific Practice".

Furthermore, I declare that the electronic and printed version of the submitted thesis are identical, both, formally and with regard to content.

Date 02.06.2020



Signature Author
Christina Laura, Kainz

The financial support by the Austrian Federal Ministry for Digital and Economic Affairs and the National Foundation for Research, Technology and Development is gratefully acknowledged.

Acknowledgments

First and foremost, I am sincerely grateful to Prof. Dr. Christian Mitterer for the possibility to author this thesis at the Chair of Functional Materials and Materials Systems, for his valuable advice and for the trust he placed in me. *Thank you for discussing your TiBN topic with me and for giving me the opportunity to be a FunkyMate!*

My sincerest gratitude goes to Dr. Nina Schalk for giving me the opportunity to compose this thesis within the scope of her Christian Doppler Laboratory ACCT. I am beyond measure thankful for her patience, valuable advice and countless hours correcting my drafts. Her door was always open and without this work, my passion for research would probably not have grown that strong. *Thank you Nina!*

I also want to thank Dr. Michael Tkadletz for his assistance regarding especially the application of advanced characterization methods. *Thank you for your valuable comments on my drafts and for encouraging me, when I went crazy over the FIB.*

I would also like to thank Prof. Jochen Schneider, PhD, for co-supervising this thesis as my mentor. I really appreciate his feedback during our workshops and his thought-provoking impulses, which helped me to see the woods for the trees.

Gratitude is also due to Dr. Christoph Czettel and Dr. Markus Pohler from Ceratizit Austria. I am grateful for the fruitful discussions during our meetings and for the comfortable working atmosphere.

I also highly appreciate the work of our colleagues from other institutes. I would like to thank Dr. Ilse Papst-Letofsky for her experimental work at the TEM and her expertise in interpreting the results. *Grazie per la buona collaborazione, Dr. Marco Deluca!* And last, but not least, *thank you, Bernhard Sartory, for taking 's nächste bildl.*

Special thanks are due to my student co-workers Thomas Resch (for spending numerous hours at the Accutom cutting my samples) and Alexandra Lechner (for helping me with the cantilevers). I appreciate it!

I would also like to express my sincerest gratitude to my cohort, the FunkyMates. I really enjoyed working with you the last three years and for starting the day with our common coffee

break. My PhD time wouldn't have been the same without the cakes of Flo's mom, Ao's naïve comments and Rafael's Jausenbrett. *Thank you all for just being as you are.*

Ich möchte mich auch bei meiner Familie bedanken, die, im Gegensatz zu mir, nie an meinen akademischen Fähigkeiten gezweifelt hat. Ich hoffe, ihr seid stolz, dass ich nun zu einer richtigen Montanistin werde.

Last, but definitely not least, I want to thank my boyfriend Dr. Michael Burtscher. Thank you for encouraging me to continue climbing the mountain and celebrating with me at the summit. You helped me to remove rocks blocking the way and pulled me back to the trail when my head was up in the clouds.

Content

1.	Introduction	1
2.	Chemical Vapor Deposition.....	3
3.	Coating Growth	7
4.	Hard Coatings	11
4.1.	TiN	12
4.2.	TiBN	13
4.3.	TiCN	15
4.4.	Coating architecture.....	17
5.	Selected Advanced Characterization Techniques for Hard Coatings.....	19
5.1.	Electron energy loss spectroscopy.....	19
5.2.	High energy X-ray diffraction.....	20
5.3.	Micro-mechanical bending tests.....	22
5.4.	Time-domain thermorefectance	23
6.	Summary and Conclusions	27
7.	References	29
8.	Publications.....	35
	Publication I.....	35
	Publication II	59
	Publication III	83
	Publication IV	107

1. Introduction

Today's increasing industrial demand towards higher productivity goes hand in hand with the requirement to improve the wear resistance and cutting performance of tools used in the metal processing sector. A method to noteworthy enhance the lifetime of cutting tools with simultaneous enhancement of cutting speed and feed rates is the application of hard protective coatings on the tool surface [1–3]. Chemical vapor deposition (CVD) is a commonly used method for the preparation of such hard coatings. Here, gaseous precursors form a solid coating on a substrate surface via condensation from the vapor phase [4].

CVD coatings based on TiN have been used for several decades for protection of cemented carbide cutting inserts, for example in milling and turning applications [5]. As hardness, toughness and thermal stability of binary TiN coatings are not sufficient for cutting of advanced steels or Ti-based workpiece materials, addition of alloying elements is crucial to expand their scope of application. Adding C to TiN to obtain TiCN, for instance, is commonly applied in the hard coating industry, which is realized through addition of CH₄ or CH₃CN to the feed gas mixture [6–8]. CVD TiBN or TiBCN coatings are, however, rarely produced due to B related process difficulties, being B diffusion and concomitant brittle W₂CoB₂ phase formation. These B containing coatings are yet promising candidates for cutting applications, as the addition of B to TiN results in a pronounced increase of hardness [9,10]. Furthermore, CVD TiBN is reported to show excellent fracture toughness [11].

Hard yet tough coatings can be realized by a layered combination of two different hard materials. The interfaces between the heterogeneous materials prevent dislocation motion, which improves hardness. Toughening is enhanced, as every interface acts as a possible crack deflection site [12]. Combining a good resistance against both, crack propagation and plastic deformation, such multilayer coatings are reported to exhibit exceptional wear resistance and cutting performance.

In addition to high mechanical loads, protective coatings for metal cutting also need to withstand temperatures of up to 1000 °C [13,14]. For development of suitable future coating materials, it is therefore crucial not only to study their microstructure and mechanical properties at room temperature, but also when exposed to high thermal loads. A further aspect that has to be

taken into account is their thermal conductivity. Ideally, a protective coating should possess a low thermal conductivity out of plane to act as a powerful thermal barrier. In that way, the high thermal load which arises during cutting can be deflected into the chip, which prevents the tool from overheating. In contrast, a high thermal conductivity in plane direction is desirable, as this allows dissipation of the heat throughout the material. Thus, hot spots at critical positions on the cutting insert can be avoided [15].

The aim of the present thesis is to create the scientific basis for designing CVD coatings within the Ti(B,C,N) system towards higher damage tolerance. The influence of B and C addition to TiN was investigated in regard of the effect on microstructure, phase composition and micro-mechanical properties. In addition, TiN/TiBN multilayer coatings were investigated in order to illuminate the influence of the bilayer period on microstructure and fracture behavior. Further, TiCN coatings grown with C₂H₆ were investigated in regard of their fracture behavior and thermal conductivity. The application of the alternative C-feeding precursor C₂H₆ allows to overcome existing issues of established processes, being either high energy consumption and brittle η -phase formation or restriction in the C/(C+N) ratio.

2. Chemical Vapor Deposition

Chemical vapor deposition (CVD) can be summarized in brief to a process, where volatile precursors react at a substrate surface to solid products. The applied precursors can be solid (Zr, Al, Hf), liquid (TiCl_4 , HCl, CH_3CN) or gaseous (H_2 , N_2 , Ar) at room temperature and ambient pressure, but are fed to the reaction chamber in a gaseous modification. Solid precursors are commonly chlorinated for this purpose. As most of the reactions for the formation of the desired molecules are not spontaneous at room temperature, the thermodynamic energy barrier has to be overcome. This is accomplished through the application of plasma, microwave radiation, or, in the industrially most relevant case, elevated temperature [4,16]. The majority of chemical vapor depositions for the hard coating industry takes place at temperatures between 700 and 1100 °C. The deposition temperature can be lowered by reduction of the pressure within the recipient or the use of catalysts. The use of metal organic (MO) precursors in the MO-CVD process furthermore allows lower deposition temperatures due to the higher reactivity of the precursors. Additionally, MO-CVD offers the possibility to achieve epitaxial growth [17]. The proceeding reactions can be essentially split into heterogeneous surface reactions and homogeneous gas phase reactions. While the first ones result in the formation of a coating on the substrate surface, the latter yield finely dispersed powder and are therefore undesired [18].

A schematic representation of an industrial scale thermal CVD plant with its essential parts is given in Fig. 1. The recipient, which is the centerpiece to every CVD plant, is where the desired surface reaction occurs. In addition to hot-wall facilities, where the temperature transfer takes place indirectly, exclusive heating of the substrates is realized in cold-wall reactors. A short path length between outlets and cutting inserts characterizes state of the art centric feed gas systems. This prevents feed gas exhaustion and allows the deposition of a homogeneous coating on the inserts' surface at every position within the recipient [19]. In order to precisely realize the desired chemical composition of the formed coating, computer-monitored mass flow controllers regulate the gas flow to the recipient [20]. Rigorous ecological regulations demand post-treatment of the exhaust gas, which is achieved by an associated gas scrubber. HCl for example, the main byproduct when using chlorinated precursors, has to be neutralized prior to recycling [18].

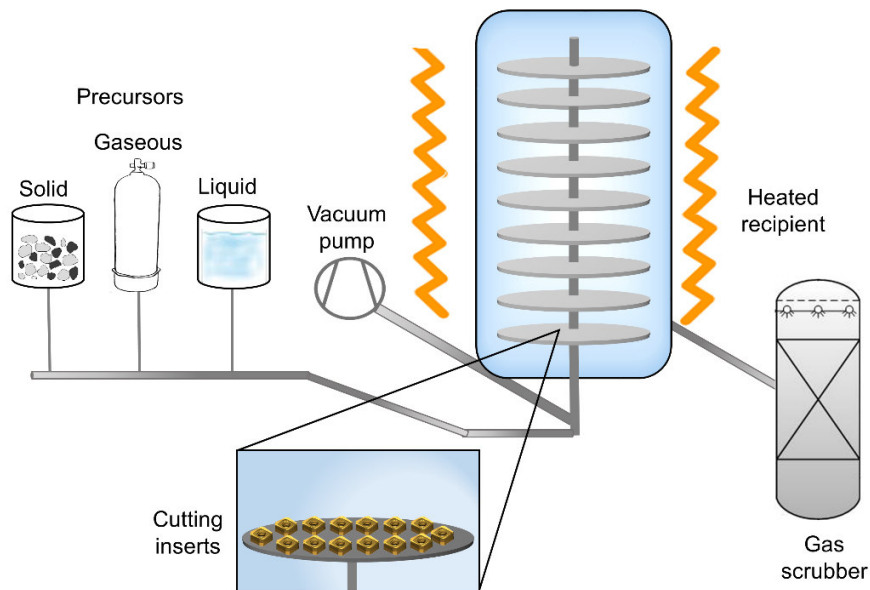


Fig. 1: Schematic representation of an industrial scale thermal CVD plant. On the left hand side, the supply of the precursors in solid, liquid and gaseous modification are shown. The deposition of the hard coating onto the cutting inserts takes place within the heated recipient shown on the right hand side. Additionally, the vacuum pump and the gas scrubber, which allows purification of the exhaust gas, are depicted.

The CVD process has some noteworthy advantages in comparison to physical vapor deposition (PVD). First and foremost, the excellent throwing power should be mentioned. CVD enables to coat geometrical complex samples uniformly with simultaneously high deposition rates [21]. This is in contrast to PVD, where positions out of the line of sight cannot be coated homogeneously [22]. A further positive aspect is the high load capacity of industrial scale CVD plants, where up to 15 000 cutting inserts can be coated within a single process [19]. However, there are also drawbacks related to CVD. The process asks for high security standards due to the fact that many commonly used precursors are toxic, explosive, corrosive or highly flammable. Though the application of vacuum or plasma allows to decrease the deposition temperature to a certain extent, the still high thermal load limits the substrate choice. In PVD, the substrate temperature can be

varied within a wide range; depositions of hard coatings for tools can even be conducted at temperatures as low as 200°C [21].

Formation of a coating on a substrate can be broken down into a sequence of events happening on the surface, which are depicted in Fig. 2. Initially, the precursor molecules need to make their way through the so-called boundary layer towards the reactive surface (1a) [18]. The thickness of this zone is influenced by several deposition parameters, such as temperature, pressure and gas velocity. While the thickness of the boundary layer depends linearly on pressure and temperature, an indirect dependence can be observed on the gas velocity. The thinner the boundary layer, the faster the diffusion through this zone is proceeding [4]. After permeation through the boundary layer, adsorption of the precursor molecules on the surface (2) is needed prior to the desired surface reaction (3). The formed reactant molecules can either desorb from the surface (4b) or undergo nucleation and growth (4a), which eventually results in coating formation. A competing undesired formation of powder through a homogeneous gas phase reaction (1b) is also possible, which occurs favorably at high temperatures and super-saturation of the gas phase [4,18].

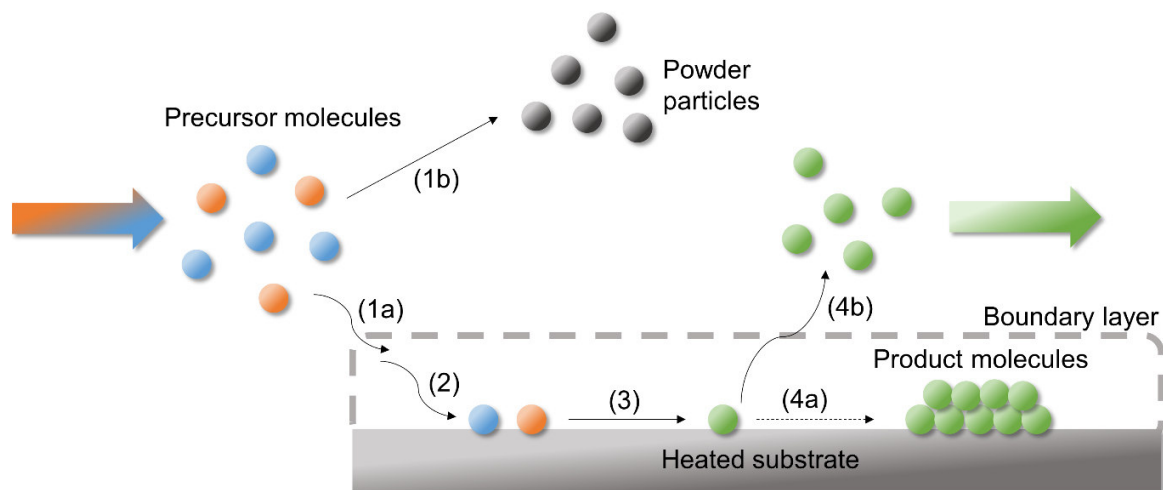


Fig. 2: Overview of involved reactions during coating deposition in a CVD process, redrawn from [18]. A detailed description of each step is given in the main text.

Depending on the applied process pressure and temperature, two different thermodynamic control mechanisms can be identified for the rate determining step: mass transport and surface kinetics. In the first case, the rate constant of the slowest surface reaction exceeds the mass transfer coefficient, which results in a slow transport of the gas through the boundary layer. In the second case, sufficient gas reaches the surface, but the surface reaction proceeds at low velocity. Surface kinetics control is known to offer a more uniform deposition within the recipient, however, higher deposition rates are generally realized in the mass-transport controlled regime [4,23]. An increment of the deposition pressure both strengthens the mass transport controlled regime and shifts the transition to surface kinetics control to lower temperatures [24]. This is accompanied by a decreasing deposition rate R_D , which follows an Arrhenius type law [18]

$$R_D = Ae^{\frac{-E_a}{RT}} \quad (2.1)$$

with A denoting the pre-exponential factor, E_a the activation energy, R the universal gas constant and T the temperature.

Prior to the deposition process, the feasibility of the desired reaction has to be evaluated by thermodynamic calculations in order to apply suitable precursors and deposition conditions. A measure for the spontaneity of the respective reaction is the change in the Gibb's free energy ΔG_r , which is defined as follows:

$$\Delta G_r = \Delta G_r^0 + RT \ln \prod a_i^{v_i}. \quad (2.2)$$

Here, ΔG_r^0 designates the change of the free energy at standard conditions, $\prod a_i^{v_i}$ the product of the activities “ i ” participating in the reaction and v_i the stoichiometric coefficient of the respective species “ i ”. The reaction proceeds spontaneously, if $\Delta G_r^0 < 0$. For a system in equilibrium state, equation 2.2 changes to

$$\Delta G_r^0 = -RT \ln K \quad (2.3)$$

where K is the equilibrium constant [4].

3. Coating Growth

The main steps involved in coating growth during deposition are summarized in Fig. 3 [25]. After condensation from the gas phase (1), the particle is either re-evaporated (2) or diffuses on the substrate surface (3). Adsorption of particles preferably takes place at energy deficient sites, e.g. lattice defects, edges or asperities. Several particles diffusing along the surface may form clusters, which is referred to as nucleation, when they reach a critical size (4). Interaction of the particles with species from the substrate through inter-diffusion can further occur (5). The mobility of the particles, which depends on their kinetic energy and the substrate temperature, defines the time needed for growth and coalescence of the particles. These particles eventually form a uniform coating (6) [21,25,26].

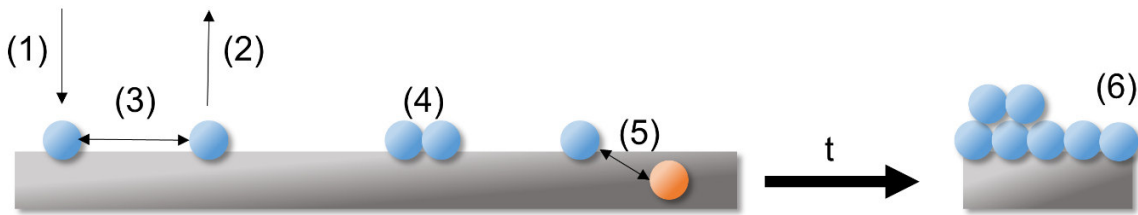


Fig. 3: Processes involved in coating growth, being (1) condensation, (2) re-evaporation, (3) surface diffusion, (4) nucleation and (5) inter diffusion, redrawn from [25].

Coating growth follows one of three main mechanisms, which are illustrated in Fig. 4a. Frank-van der Merwe (or layer-by-layer) growth occurs, when the binding energy between the atoms of the coating and substrate is higher in comparison to homogenous bonding within the coating (1). In the opposite case, Volmer-Weber growth is dominating, where the nucleating species form islands on the surface. Here, the binding energy between the coating forming atoms exceeds the binding towards the substrate (2). Stranski-Krastanov growth constitutes a mixed form of layer and island growth (3). Initially, the binding energy between substrate and coating is higher than within the coating. However, at a later stage of nucleation, island growth becomes more favorable [26].

Temperature, pressure and stoichiometry of the precursors need to be chosen carefully in order to obtain the desired coating morphology. A first guideline to predict the resulting structure from the deposition parameters was published by Movchan and Demchishin within a structure zone model (SZM) [27]. They report on the presence of three different zones, which are influenced by the homologous deposition temperature. An equivalent model for CVD coatings was introduced by Stinton *et al.*, which is shown in Fig. 4b [28]. With decreasing deposition temperature and pressure, the morphology changes from columnar (1), over faceted (2) to small grained globular (3). A low super-saturation of the reactive species in the gas phase is reported to foster epitaxial growth [18]. In addition to temperature, pressure and gas saturation, the morphology also depends on the coating thickness, as the grain size gradually increases with increasing thickness.

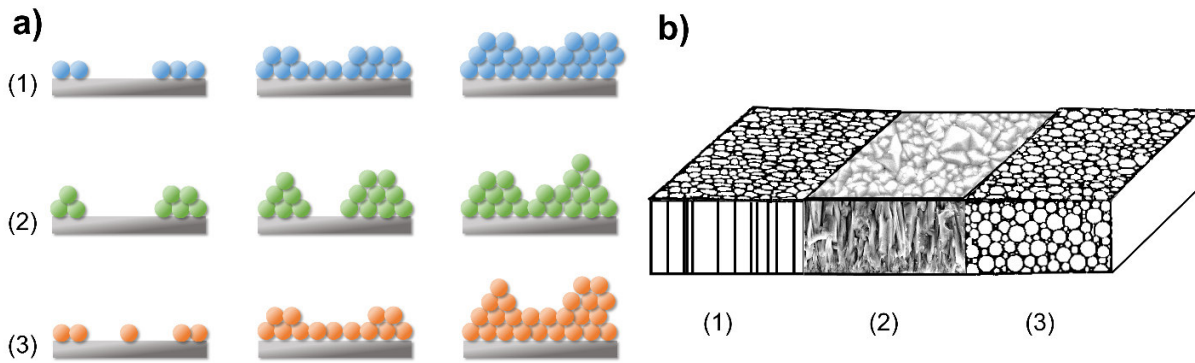


Fig. 4: a) (1) Frank-van der Merwe (layer-by-layer) growth, (2) Volmer-Weber (island) growth and (3) Stranski-Krastanov (combined layer and island) growth, redrawn from [26]; b) Structure zone model for CVD coatings according to Stinton. Depending on the deposition conditions, the coating grows in a (1) columnar, (2) faceted or (3) globular fashion, modified after [28].

Proper adjustment of the deposition process is critical to ensure a uniform coating growth as well as good adhesion between substrate and coating. Stirring of the precursors or alternately reversing their flow directions offers a possibility to overcome starvation of the feed gas. Proper coating adhesion is favored in the absence of both, contaminants at the substrate and corrosive residues from the precursors. The aforementioned depletion of one or more precursors as well as homogeneous gas phase reactions should further be prevented when aiming for a good adhesion [18]. Beside the deposition parameters, the chemical composition and surface morphology of the substrate

are decisive for the nucleation process. Thus, they often pre-determine the coating growth and properties. For the coatings studied within this thesis, cemented carbide consisting of hard WC particles and tough Co binder was used as substrate material. The properties of the adjacent coatings may be noteworthy influenced by size and orientation of the WC grains as well as the amount of Co binder within the substrate [29]. The latter one for instance affects the thermal expansion coefficient of the cemented carbide, which in turn determines the tensile crack network within the coating formed during cooling down from the deposition temperature [30].

4. Hard Coatings

In order to satisfy today's industrial demands, processing tools for the metal cutting sector have to be continuously improved. High cutting speed and feed rates are required to go hand in hand with low tool wear and economic considerations. Therefore, hard protective coatings are frequently applied on cutting tools in order to simultaneously improve their cutting performance and life time. A high hot hardness is a decisive property of the substrate material, for which cemented carbide is commonly used [31]. Sufficient hardness with concomitant toughness is crucial for the applied coating. Furthermore, the coating needs to feature high oxidation resistance, good adhesion to the substrate and ideally a pleasant color to enhance merchantability. In addition to nitride based coatings, CVD Al_2O_3 is a top seller in the metal cutting industry. This is reasoned by its resistance against chemical and thermal attack due to the already oxidized state of this compound and its high hardness at elevated temperatures [32]. Both, nitride and oxide-based hard coatings are characterized by a mixed bonding character [33]. As can be seen in Fig. 5, the central position and therefore partial behavior of metallic, covalent and ionic bonding character explains the exceptional properties of TiN based species.

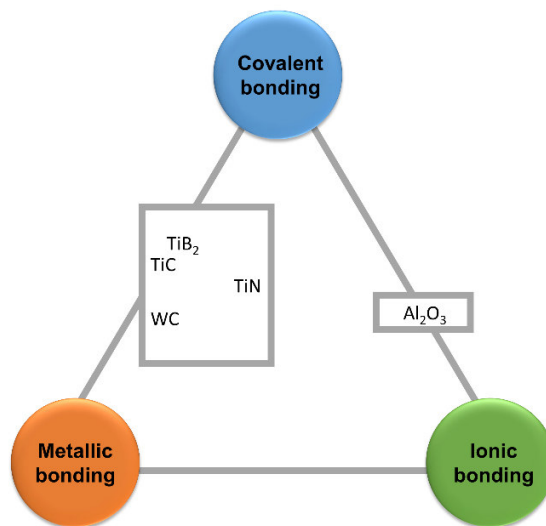


Fig. 5: Overview of the possible types of bonding in materials and the fractional bonding character of selected ceramics, redrawn from [33].

4.1. TiN

The use of TiN in the metal processing industry has established more than four decades ago and it still has significant technical relevance [5]. Applied as base layer, TiN serves as diffusion barrier between coating and substrate to prevent decarburization. Due to its golden color it is furthermore used as wear marker and for decorative purposes. TiN is commonly prepared by both, CVD and PVD and crystallizes in the face-centered cubic (fcc) NaCl structure [34]. Therein, the Ti atoms occupy the Na positions, as can be seen in Fig. 6a. The lattice parameter of stoichiometric TiN amounts to 4.242 Å [35]. Using a precursor mixture comprising TiCl₄, N₂ and H₂, TiN coatings are obtained by CVD following equation 4.1:



Additionally, Ar is fed to the recipient in order to act as carrier gas and to provide a sufficiently high overall gas flux for the reaction to proceed. Wagner *et al.* deposited CVD TiN coatings at temperatures between 800 and 1050°C and found that the activation energy of the reaction is 110 kJ/mol. This high value indicates that within the investigated temperature regime, the reaction is surface kinetics controlled [5]. Thus, the low velocity of the chemical reaction allows deposition of homogeneous coatings independent on the substrate geometry [18]. The presence of Cl within TiN based coatings is on the one hand reported to deteriorate the hardness and fracture stress. On the other hand, Cl has a positive effect on the friction behavior [36–38]. In modern deposition plants, the incorporation of Cl can be controlled in order to meet the demands for the given application [39,40]. As shown in Fig. 6b and c, CVD TiN is characterized by a competitive columnar growth of the crystals and a star-shaped pyramidal surface morphology. According to Cheng *et al.*, these structures arise from the presence of multiple twinned crystals growing preferred along five (111) twin planes [41]. One shortcoming of CVD TiN coatings is their mechanical behavior. With an indentation hardness of 18 to 25 GPa, their resistance against plastic deformation is not sufficient for cutting of many common workpiece materials [5,36,42]. Also the low fracture toughness, accounting for 2 to 3 MPam^{1/2}, should be pointed out in this context. Furthermore, the thermal stability of TiN is poor, as oxidation starts at roughly 550 °C [43,44]. During cutting of steel, this temperature, however, can be easily exceeded [13]. In order to improve both the mechanical and

thermal stability of TiN, several modifications to this coating system are reported in literature. Addition of further elements, such as B, C, Al or Si, noteworthy improves the overall performance of TiN through formation of a solid solution and grain refinement [8,9,45,46]. Sophisticated design of the coating architecture by applying multilayers represents another approach to counteract the insufficiencies of TiN (compare section 4.4.).

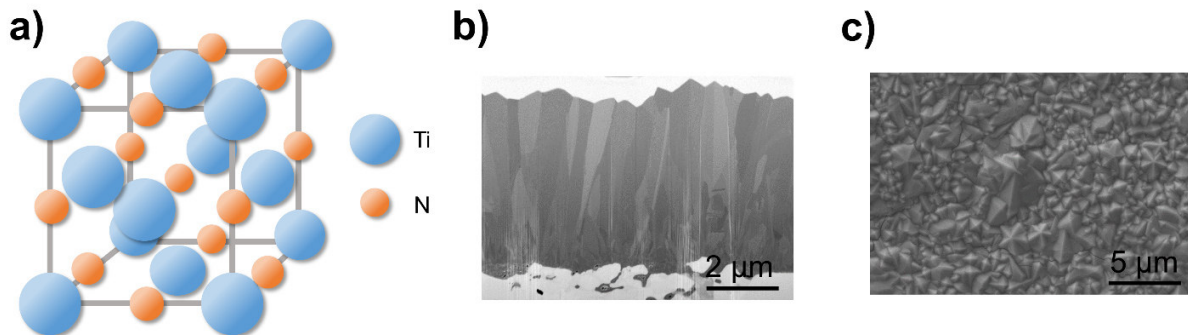


Fig. 6: (a) Crystal structure of fcc TiN according to [34], and the (b) cross-section [own work] and (c) surface morphology of a TiN coating grown by CVD [own work].

4.2. TiBN

While the presence of impurities or dopants commonly results in a reduction of the grain size, this is especially true for the effect of B on a coating [47,48]. Already small amounts (0.3 at.%) of B within TiN coatings are reported to result in grain refinement and concomitant increment of hardness by ~30 % [9]. The resulting nanocrystalline structure is characterized by exceptional mechanical properties. In literature, different statements on the phase composition in CVD TiBN coatings were presented. Wagner *et al.* and Holzschuh report on the formation of a hexagonal (h)-TiB₂ phase already at small amounts of B within the coating [9,45]. Peytavy *et al.* speak in favor of the presence of ternary fcc-TiBN [49]. A third interpretation was presented by Dreiling *et al.*, who reported on amorphous TiB at B contents < 18 at.% and h-TiB₂ in coatings with a higher B content [50]. The ternary phase diagram of Ti-B-N according to Nowotny *et al.* is shown in Fig. 7 [51]. The positions of stoichiometric TiN, TiB₂, TiB and BN are depicted as well as the tie lines enclosing the three-phase-field TiN-TiB₂-BN. The B containing coatings investigated within this thesis are all located in close vicinity to the TiN-TiB₂ tie line, either in the two- or three-phase-field.

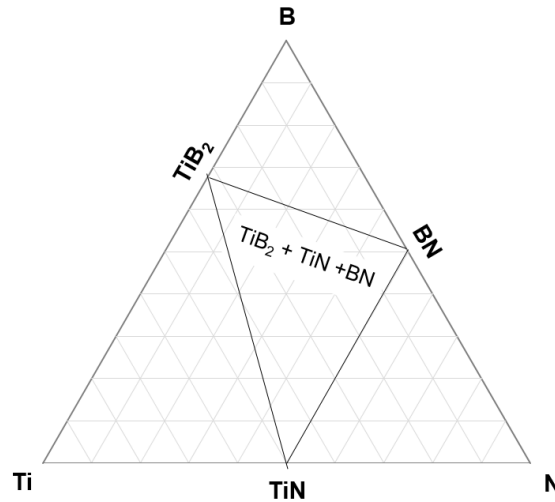


Fig. 7: Ternary phase plot of Ti-B-N with the respective phase fields, redrawn from [51].

The addition of small amounts of BCl_3 to the feed gas mixture used for TiN allows to deposit TiBN. Due to the reactivity of BCl_3 , high accuracy in regard of the flow rate of each precursor is crucial to obtain coatings with the desired elemental composition. Depending on the feed gas composition, the formation of TiB_2 and TiB follows the reactions 4.2 and 4.3, respectively.



In addition to the aforementioned improvement of the hardness, ternary TiBN coatings outperform TiN also in regard of toughness, strength, thermal stability and cutting performance [9,52,53]. The beneficial influence of B on the micro-mechanical properties of TiN is outlined within publication I and II. However, the presence of B has one major drawback, being the diffusion of this highly mobile element into the substrate. Within the commonly used WC substrate, B is reported to form a brittle W_2CoB_2 phase, which deteriorates the performance of the tool during application [45,54]. Therefore, a baselayer underneath B containing coatings is crucial for their applicability in the cutting industry. TiN is commonly used for this purpose. However, for TiBN coatings with a high B content or when h-TiB₂ is applied, poor adhesion to the baselayer is observed [55]. The reason for this is the mismatch in crystal structure, stresses and crystal size between TiN and TiB₂. CVD TiB₂ is reported to be nanocrystalline with compressive residual stresses of ~2GPa, while the columnar TiN grown by CVD exhibits tensile residual stresses of ~500 MPa. The adhesion problem

can be circumvented by a graded coating architecture with a step-wise increasing B content or by application of a multilayered coating design [42,56].

4.3. TiCN

CVD α -Al₂O₃, one of the most abundant coating materials in the metal cutting industry, is commonly applied within a multilayer stack of TiN-TiCN-Al₂O₃. Within this multilayer, TiN serves as baselayer and TiCN provides a mechanical support for the α -Al₂O₃ top-layer [57]. According to Ivashchenko *et al.*, TiN and TiC show complete miscibility in the whole composition range [58]. Therefore, TiCN exists as fcc-structured solid solution (Fig. 8a), which explains its superior hardness in comparison to TiN [59]. The lattice parameter increases linearly with increasing C/(C+N) ratio from 4.24 Å in TiN to 4.33 Å in TiC [35,60,61]. There are two industrially relevant processes for the deposition of CVD TiCN [62]. In the high temperature (HT) process, CH₄ is used as C feeding precursor. Here, the temperatures commonly exceed 950 °C, which is why this process is economically and ecologically less popular. Furthermore, formation of the brittle η -phase is an issue when using the HT process. The major advantage of using CH₄ is the possibility to vary the C/(C+N) ratio freely from pure TiN to pure TiC. This is not possible in the moderate temperature (MT) process, when solely CH₃CN is used with no additional C containing precursor. At the applied temperature of ~850 °C, the chemical bonding within CH₃CN limits the C/(C+N) ratio to ~0.67 [63,64]. However, the lower temperatures (< 900 °C) needed for this process make it industrially more relevant [6,57].

A major issue related to CVD TiCN-Al₂O₃ coatings are thermal cracks (Fig. 8b), which form during cooling in the deposition process due to emerging tensile residual stress [65]. This stress is evoked by the difference of the thermal expansion coefficient (TEC_{25-1000 °C}) between α -Al₂O₃ ($8.3 \times 10^{-6} \text{ K}^{-1}$), TiCN and the cemented carbide substrate [4]. The TEC_{25-1000 °C} of TiCN depends on the chemical composition and amounts to $8\text{--}9.6 \times 10^{-6} \text{ K}^{-1}$ [61]. This applies as well to the cemented carbide substrate, where TEC_{20-800 °C} decreases from $6.6 \times 10^{-6} \text{ K}^{-1}$ to $5.4 \times 10^{-6} \text{ K}^{-1}$ when reducing the Co content from 15 to 6 wt.% [30]. As cracks allow O penetration into TiCN or even the substrate, they are related to accelerated wear of the tool [66,67]. One possibility to tailor the stress state and thus the emerging crack network is by post-deposition treatments like dry- or wet-blasting, where

compressive residual stress is induced in the coating [68]. Stylianou *et al.* showed that the TEC mismatch of cemented carbide substrate and TiCN- Al_2O_3 coatings can be tailored by the Co content in the substrate [30]. Using ZrCN instead of TiCN or increasing the C/(C+N) ratio in TiCN constitute further possibilities to prevent the occurrence of cracks in the coating [37]. The application of C_2H_6 as C feeding precursor for the production of TiCN allows both, low deposition temperatures and adjustment of the C/(C+N) ratio [10,69]. Despite these advantages, little is known on the use of this precursor. Thus, CVD TiCN coatings prepared with C_2H_6 have been investigated in publication IV in regard of their microstructure and fracture-mechanical behavior.

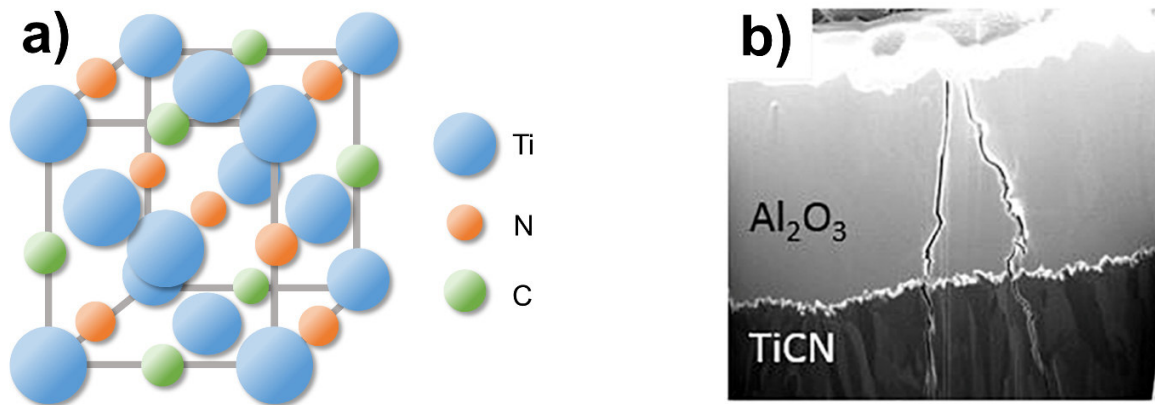


Fig. 8: (a) Crystal structure of fcc-TiCN according to [59] and (b) cross-sectional cracks through $\alpha\text{-Al}_2\text{O}_3$ and MT-TiCN [68].

A combination of solid-solution and Hall-Petch hardening is achieved in quaternary CVD TiBCN coatings, which thus exhibit high hardness of up to 33 GPa [10]. The deposition of TiBCN through CVD is reported using CH_3CN , CH_4 and C_2H_6 . Czettel *et al.* showed that with increasing B content in the coating, a more pronounced defect density and higher tensile residual stress are observed. They furthermore report on a superior cutting performance obtained for coatings with low amounts of B in comparison to ternary TiCN [6,10].

4.4. Coating architecture

Hard yet tough materials can be composed following the design rules from nature, where layered structures possess superior mechanical properties [70,71]. Using such a layered material architecture enables to improve the wear resistance of hard coatings in real-life applications, which relies on the structural and compositional heterogeneity of these materials [72]. Both, the superior properties of alternating hard and soft layers as well as the combination of two hard materials with different stiffness are reported to be beneficial [73]. The hardness increase in layered materials relies on the restriction of grain growth at the respective interface and the concomitant Hall-Petch hardening. Furthermore, the interfaces impede dislocation movement and therefore improve the material's strength [74]. According to Holleck *et al.*, toughness enhancement in multi-layered materials relies on manifold phenomena, which are schematically depicted in Fig. 9. First and foremost, the crack deflection (1) at the interfaces should be mentioned, which retards crack propagation through the material. Second, the interface may form a void during cracking, which results in a reduction of the stress concentration (2). Dissipation of energy along the interface and concomitant stress relaxation (3) further reduce the tendency of fracturing. Finally, the aforementioned restriction of grain growth is reported to favor crack splitting [12,73]. As the number of individual layers increases, the interface volume as site for energy dissipation gains more importance. Materials, where the single layer thickness is in the range of the lattice constant are called super-lattices, provided that the following preconditions are fulfilled: The respective constituents need to exhibit similar atomic radii, a comparable bonding character, a low discrepancy in the lattice parameter and they have to be isostructural [12,74].

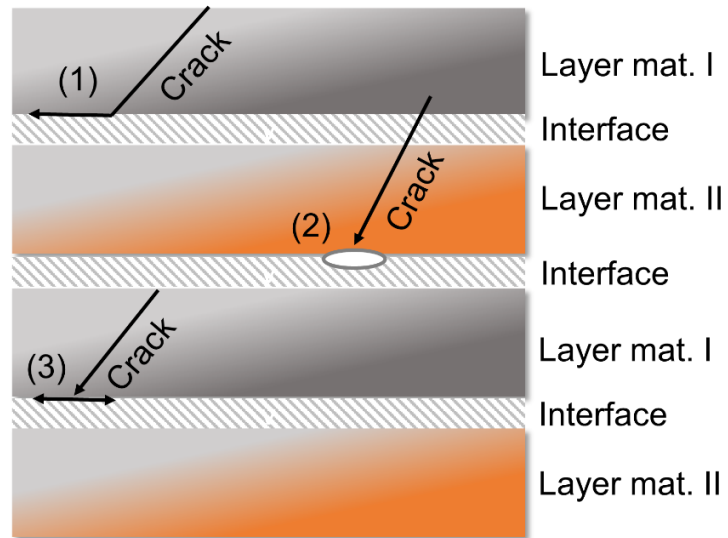


Fig. 9: Toughening mechanisms in a multi-layered material, being (1) crack deflection, (2) interface opening and (3) nano-plasticity, redrawn from [73].

5. Selected Advanced Characterization Techniques for Hard Coatings

5.1. Electron energy loss spectroscopy

Knowledge on the elemental and phase composition is of major importance for the understanding of a material. Glow discharge optical emission spectroscopy or energy dispersive X-ray spectroscopy allow elemental quantification in the bulk of the coating. However, characterization methods with a higher resolution are crucial to investigate the spatial composition of nanocomposite materials such as TiBN and TiBCN coatings [75,76]. Allowing to study both, the elemental components and binding state at single-atom level, makes electron energy loss spectroscopy (EELS) a powerful material characterization method. EELS spectra show the energy distribution of electrons, which have passed a sample inelastically [77]. It is thus possible to draw conclusions on the bonding and nearest neighbors of the analyzed atoms, their electronic structure as well as on the sample thickness [78]. The necessary components of an EELS spectrometer are incorporated into a transmission electron microscope (TEM) and are depicted in Fig. 10a.

An EELS spectrum can be divided in a low-loss and a high-loss region. The low-loss region provides information on the valence-band electrons and incorporates the intense zero-loss peak and the plasmon peak. The high-loss region includes the ionization edges characteristic for each element and binding state as a function of the energy loss [77]. Exemplary for an EELS spectrum, the ionization edges of B K, C K, N K, O K and Ti L_{23} recorded from a PVD TiBN coating are shown in Fig. 10b [79]. While for light elements, electrons from the K shell are analyzed, the outer L or M shells are used in case of heavy elements. The reason for this is that the energy required to remove an electron from a respective shell increases with atomic mass, which results in a loss of intensity in the EELS spectrum. The ionization edges are not sharp peaks, but rather show an oscillatory fine structure in the respective energy loss region. These oscillations, which rely on the nearest neighbors of the respective atom, are denoted as the electron energy loss near edge fine-structure (ELNES). The ELNES can be considered as the chemical fingerprint of a material and therefore allows to deduce the phase composition at the investigated position [80]. TiN coatings show a pronounced double peak in the Ti L_{23} edge at ~ 460 eV and two additional smaller ones at ~ 480 and 500 eV,

which are not affected by alloying small amounts of C or B to the material [11]. The two characteristic peaks at the N K edge between 390 and 420 eV do not shift significantly with addition of B or C, however, the peaks broaden with increasing energy loss [81]. According to Gupper *et al.*, the reason is scattering from the first and second atomic neighbor [79]. Ternary TiCN coatings exhibit a similar C K ionization edge as pure TiC, with the characteristic signals at ~285 and 300 eV [82]. In order to understand the phase composition of coatings in the Ti(B,C,N) system, the B K edge is most feasible for investigation due to the compound dependent shape of this edge. It is not only possible to differentiate between TiB₂, B₂O₃ and BN, also the amorphous TiB shows a different edge compared to TiB₂. However, it has to be kept in mind that the co-existence of phases with similar ELNES complicates the interpretation due to an overlap of the signals.

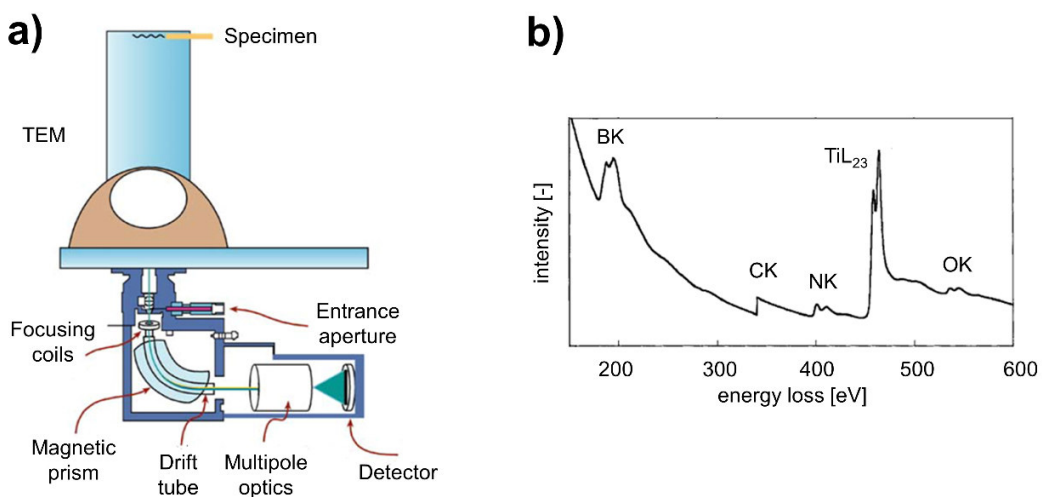


Fig. 10: a) Schematic of an EELS spectrometer with all necessary components [77]. b) EELS spectrum of a CVD TiBN coating including the B K, C K, N K, TiL₂₃ and O K edge [79].

5.2. High energy X-ray diffraction

Though conventional X-ray diffraction (XRD) allows to gain detailed insight into the microstructure of materials, there exist various restrictions. A site-specific investigation, which is especially important in multilayered or composite materials, is difficult to realize by conventional XRD. As hard coatings for metal cutting applications are subjected to high temperatures, also their properties at elevated thermal loads are of interest. However, studying the microstructure as a

function of the temperature is very time consuming using lab-scale XRD due to the low brilliance. Furthermore, in-situ combination with other characterization methods, such as differential scanning calorimetry (DSC) or nanoindentation, are hardly applicable. All of the aforementioned issues can be overcome when conducting measurements at a high energy XRD (HE-XRD) beamline at a synchrotron radiation facility.

In addition to the radiation source, several further hardware components are necessary for performing the HE-XRD experiment, being X-ray optics, sample holders and detectors, to name but a few (Fig. 11a). Two-dimensional flat panel area detectors allow to collect the whole range of the Debye-Scherrer rings at once. After azimuthal integration of these rings, a multitude of information can be gained from the 2D-diffractograms. From the positions of the Bragg-reflections in the reciprocal space, conclusions on the qualitative phase composition can be drawn [83]. Taking into account also the intensity of the respective reflections allows to conduct a quantitative phase analysis using the Rietveld method [84,85]. The distortion of the rings provides insight into the strain of the material, which can be assessed using the $\sin^2\psi$ method [86]. Provided that the X-ray elastic constants are known, the stress of the material can be calculated. The evolution of the in-plane residual strain of a CVD TiN as a function of the temperature is shown in Fig. 11b.

In addition to investigations of the microstructure at elevated temperatures (see publication III), HE-XRD can also be combined with other techniques for in-situ experiments. Saringer *et al.* investigated the temperature-dependent phase composition of a CVD TiAlN coating in a combined approach of HE-XRD and differential scanning calorimetry [88]. Zeilinger *et al.* illuminated the stress distribution in a TiN coating during nanoindentation and Erdely *et al.* conducted tensile loading tests to study the deformation of an intermetallic γ -TiAl based alloy [89,90].

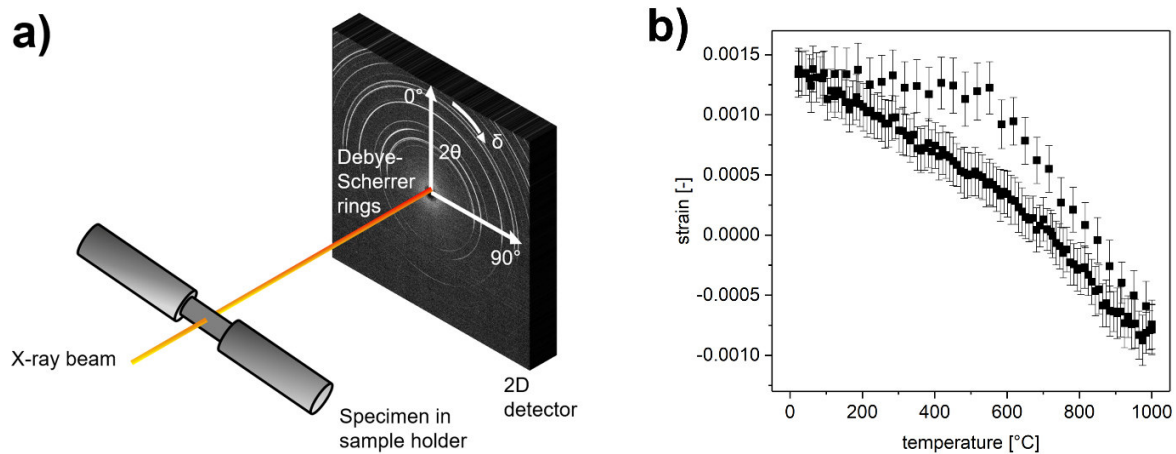


Fig. 11: a) Schematic of the measurement set-up used for HE-XRD [87]. b) Temperature dependent evolution of the residual stress in a CVD TiN coating [own work].

5.3. Micro-mechanical bending tests

Hardness and Young's modulus of hard coatings are today easily accessible by means of nanoindentation. However, the performance of a coating in cutting application not only depends on its resistance to plastic deformation. The fracture toughness, denoted by the critical stress intensity factor K_{IC} , is a further decisive parameter when assessing the suitability of a coating for metal cutting. A higher K_{IC} value is correlated with a higher ductility of the material, allowing for a better resistance against crack initiation and propagation in comparison to a brittle material [12]. Though standardized methods exist for determination of the fracture toughness of macroscopic samples, evaluating this parameter in coatings is still challenging [91]. Modern focused ion beam (FIB) workstations, however, allow to fabricate micro or even nano-sized bending specimens. These micro-cantilevers are subjected to fracture in-situ or ex-situ within a nanoindenter to record the load-displacement curve prior to fracture. Evaluation of unnotched specimen allows to determine the fracture stress and Young's modulus of the coating. Testing bending beams featuring a sharp notch in close vicinity to the cantilever beam support enables to calculate the fracture toughness [92,93].

In order to obtain feasible fracture data, special care needs to be taken during both, fabricating and testing of the micro-cantilevers. First, a pre-crack exhibiting a depth of roughly one third of the cantilever height with thin material bridges to the beam support are favorable to thick

bridges and a shallow pre-crack. This is due to a more stable crack after failure of the bridges. Furthermore, rounded ends in the pre-crack due to over-fibbing are disadvantageous and may result in an underestimation of the fracture toughness. Choosing displacement over load controlled indentation during testing of the specimen is favorable. Otherwise, catastrophic failure of the specimen may occur as soon as the crack is initiated, which results in overestimating the fracture toughness [94].

Nitride-based hard coatings generally exhibit, due to their ionic bonding part, low ductility in comparison to metals. Thus, several approaches have been reported to increase their fracture toughness. Here, the application of a multilayered coating architecture should be mentioned in the first place. Zeilinger *et al.* reported on a noteworthy enhancement of the K_{IC} value of multilayered CrN-Cr coatings in comparison to binary CrN. While the ceramic CrN provided the coating with high hardness, the metallic Cr enabled a better toughness. The authors furthermore observed that a decrement in the bilayer period further enhanced the fracture toughness [89]. This is reasoned by the fact that each interface between a ceramic and metallic layer acts as possible crack deflection site, which retards both crack initiation and propagation [12]. A further possibility to increase the fracture toughness of a ceramic coating by multilayering is achieved by the aforementioned superlattice effect [95]. The addition of further elements to originally brittle binary nitrides constitutes another approach to increase the fracture toughness. The critical stress intensity of TiN can be noteworthy improved by addition of Si, B and C as shown by Bartosik *et al.* and in publication II and IV [11,96].

5.4. Time-domain thermorefectance

The heat barrier potential of hard coatings is of major importance for the thermal management of the tool during cutting, as they need to withstand temperatures of up to 1000 °C [14,15]. Heat distribution within a material can be quantified using the thermal conductivity. In order to dissipate the heat off the contact zone, a high thermal conductivity in plane is favorable. Contrarily, a low thermal conductivity is desired out of plane as this allows deflection of the heat into the chip and thus prevention of substrate overheating [15]. Time-domain thermorefectance

(TDTR) is a state of the art method for determination of the thermal conductivity [97,98]. TDTR measurements rely on a pulsed pump-probe laser system; the measurement set-up is simplified depicted in Fig. 12 [99]. There, the pump beam heats the material surface, which results in a slight increase of the temperature. With a delay in the range of picoseconds, the probe beam hits the sample and is reflected. This allows to obtain the thermal transient data, thus the change in the sample temperature resulting from impact of the pump beam. Commonly, ~ 70 nm thin Al is used as transducer layer, as the temperature dependent optical reflectance of this material is well known. It is thus possible to derive the thermal diffusivity from the time dependent temperature gradient [98]. The thermal conductivity κ is thus obtained following

$$\kappa = \alpha \rho c_p, \quad (5.1)$$

where α denotes the thermal diffusivity, ρ the density and c_p the heat capacity of the material [100]. The information depth depends on the thermal conductivity, which is obtained by fitting of the data with a mathematical multilayer model. Crucial input parameters for this model are thickness, heat capacity and thermal conductivity of all layers within the system. In order to obtain feasible results, TDTR measurements ask for a smooth surface morphology and absence of pores in the sample.

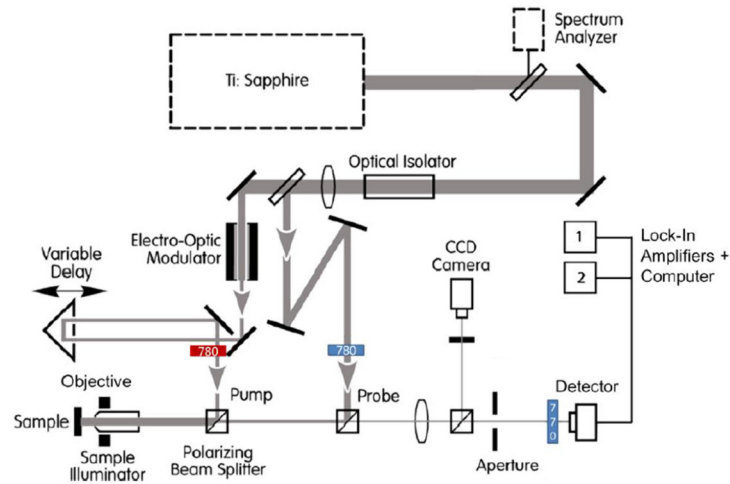


Fig. 12: Schematic view of a TDTR measurement set-up [99].

Variations in the thermal conductivity result from differences in the phonon scattering. A small grained morphology and high defect density are reported to result in an increased phonon scattering in comparison to a large grained and defect free material and thus in a lower thermal conductivity [101]. Measurement of the thermal conductivity can therefore shed light on the change in grain size and defect density upon e.g. annealing or addition of further elements to binary ceramics. Ternary and quaternary ceramics (e.g. TiCN or TiBCN) generally exhibit a lower thermal conductivity than binary ones (e.g. TiN) due to alloy scattering [102]. The composition dependent change of the phonon scattering in CVD Ti(B,C,N) coatings was studied within publication III and IV.

6. Summary and Conclusions

The aim of the present thesis was to establish design rules for damage tolerant CVD coatings in the Ti(B,C,N) system with simultaneously outstanding hardness, superior fracture toughness and ideal thermo-physical properties for metal cutting. Within publication I, the influence of the bilayer period in multilayered TiN/TiBN coatings on the (micro-)mechanical properties was assessed. The findings emphasize that the multilayers not only exhibit superior hardness and fracture toughness in comparison to binary TiN, the coating with the lowest bilayer period also outperforms the already hard and tough monolithic TiBN coating. Publication II demonstrates that the addition of C to TiN and TiBN and the resulting formation of a TiCN-based solid-solution noteworthy alters the coating morphology and properties. The presence of C results in an increase of the fracture stress and suppresses the formation of amorphous TiB in TiBCN. Due to the fine grained morphology, B containing coatings are superior in regard of hardness and fracture toughness, with the highest values observable in quaternary TiBCN. Within publication IV it is shown that the use of C₂H₆ as C feeding precursor enables the deposition of TiCN coatings over a broad compositional range, which is not possible when using CH₃CN. The lower deposition temperature needed in comparison to the application of the high temperature process speaks for this method also in regard of economy and sustainability. An increasing C/(C+N) ratio is accompanied by a more pronounced <110> orientation. The mechanical properties and thermal conductivity are more favorable for TiCN coatings in comparison to binary TiN. High energetic X-ray diffraction using synchrotron radiation allows to monitor the thermal stability, lattice strain and thermal expansion coefficient of coatings in the Ti(B,N) system up to 1000 °C (Publication III). The evaluation proved that TiN, TiB₂ and the four investigated ternary TiBN coatings are thermally stable in Ar within the tested temperature range. As the B content in the coatings increases, a lower discrepancy between the thermal expansion coefficient of substrate and coating was observed, which is desirable in regard of thermal crack suppression. To the best of the author's knowledge, up to now, no reports exist on the determination of the thermal expansion coefficient on intact, i.e. not powdered coatings. The investigations within publication III allow to close this gap, where the obtained data are verified by measurements on powdered samples of TiN and TiB₂. In addition, the out-of-plane thermal conductivity decreases

with increasing B content. Thus, B rich coatings offer a higher potential to prevent overheating of the substrate.

The combination of the investigations performed within this thesis create for the first time the scientific basis to tailor microstructure and properties of CVD coatings within the Ti(B,C,N) system towards higher toughness and at the same time outstanding hardness and superior thermo-physical properties, which enables to design damage tolerant coatings to maximize the real-life cutting performance.

7. References

- [1] T. Cselle, A. Barimani, Surf. Coat. Technol. 76-77 (1995) 712–718.
- [2] T. Cselle, New Directions in Drilling, Dry and Near-dry Machining Will Impact High Productivity Drilling in the Next Decade, Manufacturing Engineering, SME, Dearbron, MI, 1995.
- [3] R. Dubach, H. Curtins, H. Rechberger, Surf. Coat. Technol. 94–95 (1997) 622–626.
- [4] H.O. Pierson, Handbook of chemical vapor deposition, 2nd ed., Noyes Publications, Norwich NY, 1999.
- [5] J. Wagner, C. Mitterer, M. Penoy, C. Michotte, W. Wallgram, M. Kathrein, Int. J. Refract. Met. Hard Mater. 26 (2008) 120–126.
- [6] H. Holzschuh, Int. J. Refract. Met. Hard Mater. 20 (2002) 143–149.
- [7] I. Dreiling, A. Haug, H. Holzschuh, T. Chassé, Surf. Coat. Technol. 204 (2009) 1008–1012.
- [8] J. Wagner, C. Mitterer, M. Penoy, C. Michotte, W. Wallgram, M. Kathrein, Proceedings of the 16th International Plansee Seminar 2005, Vol. 2, p. 917-931.
- [9] J. Wagner, D. Hochauer, C. Mitterer, M. Penoy, C. Michotte, W. Wallgram, M. Kathrein, Surf. Coat. Technol. 201 (2006) 4247–4252.
- [10] C. Czettel, C. Mitterer, M. Penoy, C. Michotte, M. Kathrein, Surf. Coat. Technol. 215 (2013) 127–132.
- [11] C. Kainz, N. Schalk, M. Tkadletz, C. Mitterer, C. Czettel, Thin Solid Films 688 (2019) 137283.
- [12] Y.X. Wang, S. Zhang, Surf. Coat. Technol. 258 (2014) 1–16.
- [13] G. List, G. Sutter, A. Bouthiche, Int. J. of Mach. Tool. Manu. 54-55 (2012) 1–9.
- [14] I. Krajinović, W. Daves, M. Tkadletz, T. Tepperneegg, T. Klünsner, N. Schalk, C. Mitterer, C. Tritremmel, W. Ecker, C. Czettel, Surf. Coat. Technol. 304 (2016) 134–141.
- [15] P.H.M. Böttger, L. Braginsky, V. Shklover, E. Lewin, J. Patscheider, D.G. Cahill, M. Sobiech, J. Appl. Phys. 116 (2014) 13507.
- [16] H. Frey, Vakuumbeschichtung 1, Plasmaphysik – Plasmadiagnostik – Analytik, VDI Verlag, Düsseldorf, 1995.

- [17] J.L. Zilko, Metal Organic Chemical Vapor Deposition: Technology and Equipment, in: K. Seshan (Ed.), Handbook of Thin Film Deposition Processes and Techniques, William Andrew, Norwich NY, 2001, pp. 151–203.
- [18] K.L. Choy, Prog. Mater. Sci. 48 (2003) 57–170.
- [19] Mohn, E., Bonetti, R., H. Wiprachtiger, J. Phys. Colloques 50 (1989) C5 811–819.
- [20] H. Czirchos, M. Hennecke, Hütte, Das Ingenieurwesen, Springer–Verlag Berlin, Heidelberg, 2004.
- [21] R.F. Bunshah (Ed.), Handbook of Hard Coatings, Noyes Publications, Park Ridge, New Jersey, 2001.
- [22] D.M. Mattox, Handbook of Physical Vapor Deposition (PVD) Processing, William Andrew, Norwich NY, 2010.
- [23] J.-H. Park, T.S. Sudarshan (Eds.), Chemical Vapor Deposition, ASM International, Russel Township, 2001.
- [24] J.-O. Carlsson, Thin Solid Films 130 (1985) 261–282.
- [25] H. Lüth, Solid Surfaces, Interfaces and Thin Films, Springer Verlag, Berlin, Heidelberg, 2010.
- [26] M. Ohring, The Materials Science of Thin Films – Deposition and Structure, Academic Press, San Diego, 2002.
- [27] B.A. Movchan, A.V. Demchishin, Fiz. Metal. Metalloved. 28 (1969) 653–660.
- [28] D.P. Stinton, T.M. Bessman, R. Lowden, Cer. Bul. 67 (1988) 350–355.
- [29] T. Csanádi, M. Bl'anda, N.Q. Chinh, P. Hvizdoš, J. Dusza, Acta Mater. 83 (2015) 397–407.
- [30] R. Stylianou, D. Velic, W. Daves, W. Ecker, A. Stark, N. Schell, M. Tkadletz, N. Schalk, C. Czettl, C. Mitterer, Int. J. Refract. Met. Hard Mater. 86 (2020) 105102.
- [31] W. Wallgram, U. Schleinkofer, Synthesis, structure, and behaviour of a new CVD TiB₂ coating with extraordinary properties for high performance applications, in: L.S. Sigl, P. Rödhammer, H. Wildner (Eds.), 17th Int. Plansee Seminar, Reutte, Austria, p. HM32.
- [32] M. Rebelo de Figueiredo, M.D. Abad, A.J. Harris, C. Czettl, C. Mitterer, P. Hosemann, Thin Solid Films 578 (2015) 20–24.
- [33] H. Holleck, Surf. Coat. Technol. 43/44 (1990), 245–258.

- [34] A.N. Christensen, V. Romano, R. Hesse, A.F. Andresen, P. Fischer, *Acta Chem. Scand.* 29a (1975) 563–564.
- [35] International Centre for Diffraction Data, PDF-2 Release, Card number 00-038-1420, 2018.
- [36] M. Stoiber, E. Badisch, C. Lugmair, C. Mitterer, *Surf. Coat. Technol.* 163–164 (2003) 451–456.
- [37] I. El Azhari, J. García, F. Soldera, S. Suarez, E. Jiménez-Piqué, F. Mücklich, L. Llanes, *Int. J. Refract. Met. Hard Mater.* 86 (2020) 105050.
- [38] I. El Azhari, J. Barrirero, J. García, F. Soldera, L. Llanes, F. Mücklich, *Scripta Mater.* 162 (2019) 335–340.
- [39] Y.J. Liu, H.J. Kim, Y. Egashira, H. Kimura, H. Komiyama, *J. Am. Ceram. Soc.* 79/5 (1996) 1335.
- [40] C. Czettel, *Design of CVD Coatings for Cutting Tools*, Ph.D. Thesis, Leoben, 2013.
- [41] H.-E. Cheng, M.-H. Hon, *J. Appl. Phys.* 79 (1996) 8047–8053.
- [42] M. Tkadletz, N. Schalk, C. Mitterer, J. Keckes, M. Pohler, C. Czettel, *Int. J. Refract. Met. Hard Mater.* 71 (2018) 280–284.
- [43] W.D. Münz, *J. Vac. Sci. Technol. A* 4 (1998) 2717.
- [44] C.W. Kim, K.H. Kim, *Thin Solid Films* 307 (1997) 113–119.
- [45] H. Holzschuh, *Thin Solid Films* 469–470 (2004) 92–98.
- [46] J. Wagner, V. Edlmayr, M. Penoy, C. Michotte, C. Mitterer, M. Kathrein, *Int. J. Refract. Met. Hard Mater.* 26 (2008) 563–568.
- [47] M. Kathrein, W. Schintlmeister, W. Wallgram, U. Schleinkofer, *Surf. Coat. Technol.* 163–164 (2003) 181–188.
- [48] S. Ruppi, A. Larsson, *J. Vac. Sci. Technol. A* 21, 66 (2003).
- [49] J.L. Peytavy, A. Lebugle, G. Montel, *High Temperatures – High Pressures* 10 (1978) 341–345.
- [50] I. Dreiling, C. Raisch, J. Glaser, D. Stiens, T. Chassé, *Surf. Coat. Technol.* 206 (2011) 479–486.
- [51] H. Nowotny, F. Benesovsky, C. Brukl, O. Schob, *Monatsh. Chem.* 92 (1961) 403–414.

- [52] C. Kainz, N. Schalk, M. Tkadletz, C. Mitterer, C. Czettl, *Surf. Coat. Technol.* 370 (2019) 311–319.
- [53] P. Wolff, Department of Materials Technology, Technische Universität Bergakademie Freiberg (2002).
- [54] R. Bonetti, H.E. Hintermann, *J. Electrochem. Soc.* 124 (1977) C298.
- [55] C. Czettl, J. Thurner, U. Schleinkofer, *Int. J. Refract. Met. Hard Mater.* 71 (2018) 330–334.
- [56] M. Stoiber, S. Perlot, C. Mitterer, M. Beschliesser, C. Lugmair, R. Kullmer, *Surf. Coat. Technol.* 177–178 (2004) 348–354.
- [57] S. Rупpi, *Surf. Coat. Technol.* 202 (2008) 4257–4269.
- [58] V.I. Ivashchenko, P.E.A. Turchi, A. Gonis, L.A. Ivashchenko, P.L. Skrynskii, *Metall. Mater. Trans. A* 37 (2006) 3391–3396.
- [59] G. Levi, W.D. Kaplan, M. Bamberger, *Mater. Lett.* 35 (1988) 344–350.
- [60] International Centre for Diffraction Data, PDF–2 Release, Card number 00–032–1383, 2018.
- [61] C. Saringer, C. Kicking, F. Munnik, C. Mitterer, N. Schalk, M. Tkadletz, *Thin Solid Films* 688 (2019) 137307.
- [62] S. Rупpi, *J. Phys. IV France* 11 (2001) 847–859.
- [63] A. Larsson, S. Rупpi, *Thin Solid Films* 402 (2002) 203–210.
- [64] R. Bonetti, H. Wiprachtiger, E. Mohn, *Metal. Powder. Rep.* 45 (1990) 837.
- [65] D. Hochauer, C. Mitterer, M. Penoy, C. Michotte, H.P. Martinz, M. Kathrein, *Surf. Coat. Technol.* 203 (2008) 350–356.
- [66] D. Hochauer, C. Mitterer, M. Penoy, S. Puchner, C. Michotte, H.P. Martinz, H. Hutter, M. Kathrein, *Surf. Coat. Technol.* 206 (2012) 4771–4777.
- [67] X. Chen, H. Liu, Q. Guo, S. Sun, *Int. J. Refract. Met. Hard Mater.* 31 (2012) 171–178.
- [68] M. Gassner, N. Schalk, M. Tkadletz, C. Czettl, C. Mitterer, *Int. J. Refract. Met. Hard Mater.* 81 (2019) 1–6.
- [69] C. Kainz, N. Schalk, M. Tkadletz, M. Winkler, C. Czettl, *Surf. Coat. Technol.* 394 (2020) 125868.

- [70] A. Zeilinger, R. Daniel, M. Stefanelli, B. Sartory, L. Chitu, M. Burghammer, T. Schöberl, O. Kolednik, J. Keckes, C. Mitterer, *J. Phys. D: Appl. Phys.* 48 (2015) 295303.
- [71] M. Meindlhumer, J. Zalesak, R. Pitonak, J. Todt, B. Sartory, M. Burghammer, A. Stark, N. Schell, R. Daniel, J.F. Keckes, M. Lessiak, A. Köpf, R. Weißenbacher, J. Keckes, *Nanoscale* 11 (2019) 7986–7995.
- [72] R. Daniel, M. Meindlhumer, W. Baumegger, J. Zalesak, B. Sartory, M. Burghammer, C. Mitterer, J. Keckes, *Acta Mater.* 122 (2017) 130–137.
- [73] H. Holleck, V. Schier, *Surf. Coat. Technol.* 76-77 (1995) 328–336.
- [74] J.S. Koehler, *Phys. Rev. B* 2 (1970) 547–551.
- [75] C. Mitterer, P.H. Mayrhofer, M. Beschliesser, P. Losbichler, P. Warbichler, F. Hofer, P.N. Gibson, W. Gissler, H. Hruby, J. Musil, J. Vlček, *Surf. Coat. Technol.* 120-121 (1999) 405–411.
- [76] X. Chen, S. Ma, K. Xu, P.K. Chu, *Vacuum* 86 (2012) 1505–1512.
- [77] D.B. Williams, C.B. Carter, *Transmission electron microscopy: A textbook for materials science*, 2nd ed., Springer, New York, 2008.
- [78] R.F. Egerton, *Rep. Prog. Phys.* 72 (2009) 16502.
- [79] A. Gupper, A. Fernández, C. Fernández-Ramos, F. Hofer, C. Mitterer, P. Warbichler, *Monatsh. Chem.* 133 (2002) 837–848.
- [80] V.J. Keast, A.J. Scott, R. Brydson, D.B. Williams, J. Bruley, *J. Microsc.* 203 (2001) 135–175.
- [81] C. López-Cartes, D. Martínez-Martínez, J.C. Sánchez-López, A. Fernández, A. García-Luis, M. Brizuela, J.I. Oñate, *Thin Solid Films* 515 (2007) 3590–3596.
- [82] C. Mirguet, L. Calmels, Y. Kihn, *Micron* 37 (2006) 442–448.
- [83] R.E. Dinnebier, A. Leineweber, J.S.O. Evans, *Rietveld refinement: Practical powder diffraction pattern analysis using TOPAS*, De Gruyter, Berlin, Boston, 2019.
- [84] H.M. Rietveld, *Acta Cryst.* 22 (1967) 151–152.
- [85] H.M. Rietveld, *J. Appl. Crystallogr.* 2 (1969) 65–71.
- [86] U. Welzel, J. Ligot, P. Lamparter, A.C. Vermeulen, E.J. Mittemeijer, *J. Appl. Crystallogr.* 38 (2005) 1–29.

- [87] C. Kainz, N. Schalk, M. Tkadletz, C. Saringer, M. Winkler, A. Stark, N. Schell, J. Julin, C. Czettel, *Surf. Coat. Technol.* 384 (2020) 125318.
- [88] C. Saringer, M. Tkadletz, A. Stark, N. Schell, C. Czettel, N. Schalk, *Surf. Coat. Technol.* 374 (2019) 617–624.
- [89] A. Zeilinger, J. Todt, C. Krywka, M. Müller, W. Ecker, B. Sartory, M. Meindlhumer, M. Stefenelli, R. Daniel, C. Mitterer, J. Keckes, *Sci. Rep.* 6 (2016) 22670.
- [90] P. Erdely, P. Staron, E. Maawad, N. Schell, H. Clemens, S. Mayer, *Acta Mater.* 158 (2018) 193–205.
- [91] C28 Committee, *Test Methods for Determination of Fracture Toughness of Advanced Ceramics at Ambient Temperature*, ASTM International, West Conshohocken, PA.
- [92] D. Di Maio, S.G. Roberts, *J. Mater. Res* 20 (2005) 299–302.
- [93] K. Matoy, H. Schönherr, T. Detzel, T. Schöberl, R. Pippan, C. Motz, G. Dehm, *Thin Solid Films* 518 (2009) 247–256.
- [94] S. Brinckmann, K. Matoy, C. Kirchlechner, G. Dehm, *Acta Mater.* 136 (2017) 281–287.
- [95] R. Hahn, M. Bartosik, R. Soler, C. Kirchlechner, G. Dehm, P.H. Mayrhofer, *Scripta Mater.* 124 (2016) 67–70.
- [96] M. Bartosik, R. Hahn, Z.L. Zhang, I. Ivanov, M. Arndt, P. Polcik, P.H. Mayrhofer, *Int. J. Refract. Met. Hard Mater.* 72 (2018) 78–82.
- [97] Y.K. Yee, S.L. Singer, W. Kim, J.M.O. Zide, L. Hong, D.G. Cahill, A. Majumdar, A.C. Gossard, *J. Appl. Phys.* 105, 054303 (2009).
- [98] D.G. Cahill, *Rev. Sci. Instr.* 75 (2004) 5119.
- [99] M. Winkler, *Nanostructured thermoelectrics: Bi₂Te₃ / Sb₂Te₃ based superlattice systems fabricated by MBE and sputtering*, Ph.D. Thesis, Tübingen, 2014.
- [100] R.B. Bird, W.E. Stewart, E.N. Lightfoot, *Transport phenomena*, 2nd ed., Wiley, New York, 2007.
- [101] M.K. Samani, X.Z. Ding, N. Khosravian, B. Amin-Ahmadi, Y. Yi, G. Chen, E.C. Neyts, A. Bogaerts, B.K. Tay, *Thin Solid Films* 578 (2015) 133–138.
- [102] T. Hori, J. Shiomi, *Sci. Technol. Adv. Mater.* 20 (2019) 10–25.

Publication I

Microstructure and mechanical properties of CVD TiN/TiBN multilayer coatings

Christina Kainz, Nina Schalk, Michael Tkadletz, Christian Mitterer,
Christoph Czettl

Surface & Coatings Technology 370 (2019) 311-319



Microstructure and mechanical properties of CVD TiN/TiBN multilayer coatings

Christina Kainz¹, Nina Schalk¹, Michael Tkadletz², Christian Mitterer², Christoph Czettel³

¹ Christian Doppler Laboratory for Advanced Coated Cutting Tools at the Department of Materials Science, Montanuniversität Leoben, Franz-Josef-Straße 18, 8700 Leoben, Austria

² Department of Materials Science, Montanuniversität Leoben, Franz-Josef-Straße 18, 8700 Leoben, Austria

³ Ceratizit Austria GmbH, Metallwerk-Plansee-Straße 71, 6600 Reutte, Austria

Keywords: Multilayer, TiBN, CVD, TEM, Micromechanical testing

Abstract

Application of a multilayered coating architecture based on two alternating hard materials provides a strategy to enhance the mechanical properties of hard coatings for the metal cutting industry. Within this work, the mechanical behavior of CVD TiN/TiBN multilayer coatings was correlated with their microstructure and compared to the respective single-layers. Multilayers with different bilayer periods (1400, 800, 300 and 200 nm) were prepared in an industrial-scale thermal CVD plant by alternate variation of the feed gas composition. Complementary X-ray diffraction, Raman spectroscopy and transmission electron microscopy investigations confirmed a dominating face-centered cubic TiN structure, accompanied by hexagonal TiB₂ and amorphous TiB in the B containing coatings. The addition of B and a decreasing bilayer period resulted in a decreasing grain size and increasing hardness. Micromechanical bending tests revealed an increase of strength and fracture toughness with addition of B and increasing layer number. While the highest strength was observed in a TiBN single-layered coating, the multilayered TiN/TiBN with a bilayer period of 200 nm was the hardest and at the same time toughest of the investigated coatings.

1. Introduction

The demand for high cutting speed and feed rates and simultaneous cost efficiency in the metal cutting industry requires, besides substrate materials with high hot hardness, sophisticated coating materials [1,2]. Hard, wear-resistant TiN coatings have been used for more than 40 years to improve the cutting performance and lifetime of cemented carbide cutting inserts [3]. In addition to solid solution strengthening, further hardening of TiN coatings can be realized by grain refinement through addition of dopants such as B [2]. TiBN coatings are commonly applied for cutting of Ti alloys due to their high hardness at elevated temperatures combined with good oxidation and wear resistance [2,4]. Therefore, extensive research has been performed with special regard to the nanocomposite nature of TiBN, which can be prepared by both, physical or chemical vapor deposition (CVD) [5–8].

In addition to multiphase or nanocomposite coatings, multilayers provide a possibility to attain properties difficult to achieve with a conventional single-layer approach [9]. Hardening in multilayers results from prevention of dislocation movement due to interfaces. Toughening is mainly achieved by crack deflection at the interfaces of adjacent layers [10]. Hard yet tough coatings are reported to offer superior wear resistance in real-life applications compared to brittle hard coatings. They may be realized by a multilayer combination of two different hard materials [11]. Though the proficient properties of TiN and TiBN qualify them as suitable candidates for high performance multilayers in cutting applications, few reports have been published so far on CVD TiN/TiBN multilayers [12–15]. Further, no literature can be found where the relationship between the microstructure and the fracture behavior on the microscopic scale with respect to the bilayer period λ is discussed for the given coating system.

Thus, the aim of the present work is to illuminate the effects of B addition and λ in CVD multilayer coatings with alternating TiN and TiBN layers on the chemical and crystallographic structure as well as on the micromechanical properties. The combinatorial application of sophisticated characterization techniques like transmission electron microscopy and bending tests performed on free-standing coating micro-cantilevers enabled both a detailed insight into the

microstructure of the investigated coatings and the identification of the coating with the most favorable mechanical properties for cutting applications.

2. Experimental methods

Coating depositions were carried out in an industrial-scale thermal CVD plant. A gas mixture of TiCl_4 , H_2 , N_2 , BCl_3 and Ar was used to synthesize TiN and TiBN single-layer and TiN/TiBN multilayer coatings. 6, 12, 24 and 40-layered coatings of alternating TiN and TiBN were prepared by interruption of the BCl_3 feed gas flow, whereas the uppermost layer was TiN. Within the B containing layers, the BCl_3 content in the feed gas was adjusted to 0.15 vol.%. In order to prevent B diffusion into the substrate, the coatings were deposited on a $\sim 0.5 \mu\text{m}$ thick TiN base-layer. The process temperature and pressure were held constant throughout the deposition at $900 \text{ }^\circ\text{C}$ and 930 mbar, respectively. The total thickness of the investigated coatings was between 4 and $5 \mu\text{m}$. Therefore, bilayer periods of ~ 1400 , 800, 300 and 200 nm for the 6, 12, 24 and 40 layered coatings, respectively, were obtained. The multilayer coatings are named accordingly to the respective bilayer period. As substrate material, cemented carbide cutting inserts in SEKN 1203 AF-G3 geometry (according to ISO 1832) with 87 wt.% WC, 9 wt.% Co and 4 wt.% mixed carbides were used.

The elemental composition of the coatings was determined by glow discharge optical emission spectroscopy (GDOES) using a Jobin-Yvon Horiba JY10000 spectroscope. Isostatic hot pressed reference materials of different compositions were used for calibration. Surface and cross section morphology of the single- and multilayer coatings was evaluated using a field emission gun scanning electron microscope (SEM) of type Zeiss Auriga. Crystallographic analyses were conducted by X-ray diffraction (XRD) with a Bruker AXS D8 Advance diffractometer in grazing incidence geometry (incidence angle 2°). Residual stresses were determined using the $\sin^2\psi$ method in Ω mode on the (422) reflection with Cu-K_α radiation [16]. In the used set-up, the Bragg angle 2θ was kept constant between 124.5 and 127° . The inclination angle of the sample surface normal in regard to the diffraction vector (ψ) was varied in 14 steps from 0 to 58.5° . ψ angles were chosen in that way that the resulting $\sin^2\psi$ values featured equidistant steps of roughly 0.05. Elastic constants taken from ref. [17] were subsequently used to obtain the stress from the measured strain [18]. Texture analysis

was carried out in Bragg-Brentano geometry and preferred orientation was evaluated by texture coefficients (TC) from the intensities $I(hkl)$ of the measured peaks according to [19]. Texture-free intensities $I_0(hkl)$ of face-centered cubic (fcc) TiN were taken from the ICDD file # 00-038-1420. A total of $n=7$ peaks were included in the analysis, i.e. (111), (200), (220), (311), (331), (420) and (422). To gain deeper insight into the microstructure of the multilayers, lamellae for transmission electron microscopy (TEM) were prepared by focused ion beam (FIB) milling using an Orsay Physics Cobra Z-05 device. The lamellae were investigated with an FEI Tecnai F20 microscope equipped with a Schottky field emitter (200 kV). For the N K jump ratio micrographs, the pre-edge micrographs were recorded at 385 eV and the post-edge images at 411 eV. Electron energy loss spectroscopy (EELS) was executed in imaging mode. The C2 aperture, objective aperture and entrance aperture for the high resolution Gatan imaging filter were set to 150 μm , 70 μm and 3 mm, respectively. Selected area electron diffraction (SAED) was done using an FEI Tecnai 12 microscope operating with an LaB_6 cathode (120 kV). The camera length was set to 1000 mm and the diffraction aperture to 6 μm . Complementary information on the phase composition was gained by cross-sectional μ -Raman spectroscopy using a LabRAM HR800 spectrometer from Horiba Jobin-Yvon. The device was equipped with a frequency-doubled Nd-YAG laser ($\lambda=514.5$ nm). The measurement was performed applying a step size of 250 nm and a spot size of 750 nm.

Coating hardness and Young's modulus were determined by nanoindentation using an Ultra Micro Indentation System (UMIS) from Fischer-Cripps Laboratories operating with a diamond Berkovich tip. Prior to indentation, the surface of the coatings was polished to obtain a smooth surface for a reasonable measurement. To keep the penetration depths <10 % of the film thickness and therefore exclude substrate effects, a plateau test from 10 to 30 mN with a step size of 1 mN was carried out. Data evaluation was conducted accordingly to the method of Oliver and Pharr [20]. In order to gain insight into the fracture behavior of the coatings, micromechanical tests were executed. Two sets of freestanding bending beams, i.e. notched and unnotched, were prepared by FIB machining on an FEI DualBeam Versa 3D device. The dimensions were adjusted to a bending length of ~ 9 μm and a cross-section of $\sim 3 \times 3$ μm^2 . Unnotched beams served for the determination of the fracture stress. Fracture toughness was evaluated on samples with a sharp notch, located in a

distance of $\sim 1 \mu\text{m}$ from the cantilever beam support. The planned indentation position was marked by a reticule with the FIB. The bending beams were imaged by scanning probe microscopy using a Hysitron TriboIndenter TI950 and a spheroconical tip. Loading of the bending beams was done at a rate of $1600 \mu\text{N/s}$. Taking into account the cantilever geometry and measured load-displacement curve, data analysis was performed accordingly to the method of Matoy *et al.* [21]. In order to gain statistical reliable data, a minimum of each three notched and unnotched beams were tested for every coating system. Depth of the notch and fracture cross sections were evaluated by post-mortem analysis using SEM.

3. Results and discussion

3.1. Microstructure and chemical composition

The elemental analysis of the single-layer coatings showed a stoichiometric composition for fcc-TiN and a mean composition of 5 at.% B, 48 at.% Ti and 47 at.% N for TiBN. Therefore, the composition of the investigated TiBN coating lies within the section TiN-TiB₂-BN in the ternary phase diagram [22], close to the tie-line of TiN-TiB₂. Since the deposition parameters for TiN and TiBN in the single- and multilayer coatings were the same, the composition of the respective layers in the multilayer system was assumed to be equal to the respective single-layer coating.

The surface morphology of the TiN single-layer (Fig. 1a) is characterized by star-shaped and pyramidal grains, which is in accordance to the findings of Wagner *et al.* [23]. These star-shaped crystals have been suggested to originate from the formation of twinned nuclei at the given comparatively low deposition temperature. V-shaped columnar grains, typical for competitive growth, of $\sim 0.5 \mu\text{m}$ in-plane and a few μm in growth direction can be observed in the cross-section of TiN (Fig. 1d). The TiBN single-layer displays a similar, although finer structure compared to TiN, which is accompanied by needles (Fig. 1b). The fine grained cross-section of TiBN in Fig. 1e reveals a pronounced decrease in crystallite size compared to TiN, which is in good agreement with the existing literature [2,5,7,8,15]. Fig. 1c depicts, representative for the TiN/TiBN multilayers, the surface of the coating with $\lambda=1400 \text{ nm}$, showing a similar surface morphology as single-layered TiBN but without any needles. The cross-section micrograph, shown in Fig. 1f, reveals that the large

columnar TiN grains are interrupted by small crystallites in the TiBN layers, followed by a renewed growth of columnar grains in the subsequent TiN layer.

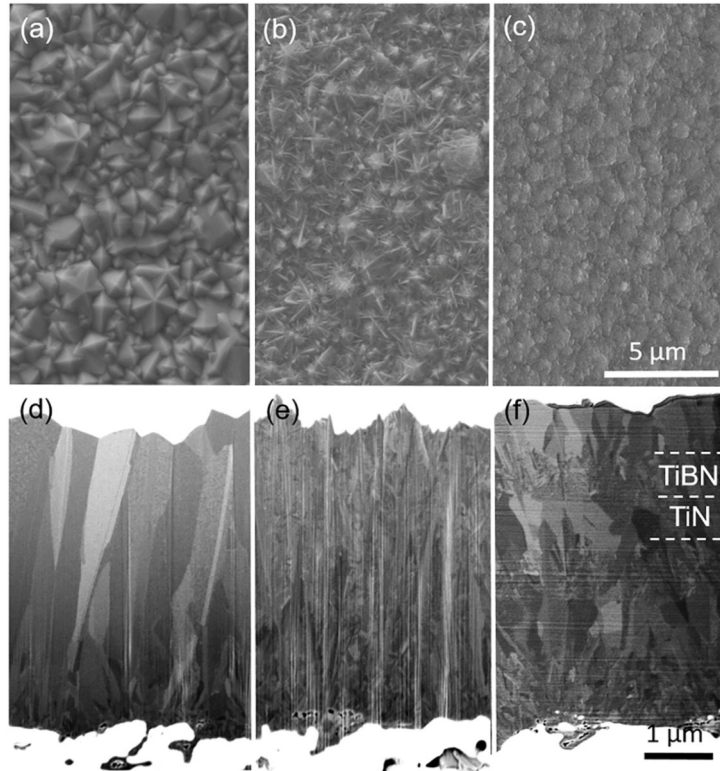


Fig. 1: SEM surface (top) and cross-section morphology (bottom) of (a,d) the TiN and (b,e) the TiBN (5 at.% B) single-layers and (c,f) the TiN/TiBN coating with $\lambda=1400$ nm representative for the multilayers.

In Fig. 2a, the X-ray diffractograms of the coatings are summarized. In the following, the multilayer coatings are named TiN/TiBN with the respective layer number. Standard peak positions of fcc-TiN and hexagonal (h) TiB₂ are marked by dashed lines [24,25]. All reflections of the TiN single-layer correspond to the respective ICDD pattern. The additional small peak at $2\theta=34.6^\circ$, which is observed in the TiBN single-layer and in the multilayers, can be assigned to the (100) reflection of h-TiB₂. No indication for crystalline BN is apparent in any of the investigated coatings. The lattice parameter - determined by Rietveld refinement - of the herein investigated TiBN single-layer does with 4.25 Å not differ noteworthy from the one of fcc-TiN (4.24 Å). Though the given diffractograms speak against the incorporation of B within the fcc-TiN grains, it cannot fully be

ruled out. With respect to the phase composition of TiBN coatings with B contents of ~5 at.%, different conclusions can be found in the existing literature. While Holzschuh and Wagner *et al.* described the formation of h-TiB₂ within TiBN coatings already at low B contents [26,27], Peytavy *et al.* reported a substitution of N by B in fcc-TiN to obtain fcc-Ti(B,N) [28]. In another approach, Dreiling *et al.* suggested the formation of amorphous TiB at B contents ≤18 at.%, which was reinforced by Raman spectroscopy [29]. Fig. 2b summarizes the influence of B addition and λ on the full width at half maximum (FWHM) of the X-ray diffraction peaks and the residual stresses. The evaluation of the FWHM, conducted on the (220) peak, confirms the microstructural changes with addition of B and variation of λ . While the sharp diffraction peaks of TiN originate from the coarse grained microstructure, peak broadening in TiBN is due to the smaller size of coherently diffracting domains [27,30]. Rietveld refinement indicated a noteworthy reduced crystallite size of the fcc-phase in the TiBN coating compared to that of the binary TiN coating. Although less pronounced compared to the distinct FWHM increase with addition of B, peak broadening can also be observed with decreasing λ in the multilayers (Fig. 2b). This is associated with the rising number of interfaces, at which grain growth is interrupted, as can be seen from the SEM cross-section of the multilayer coating with $\lambda=1400$ nm in Fig. 1c. The tensile residual stresses increase from 433 ± 7 MPa in TiN to 890 ± 28 MPa in TiBN; the stresses in the multilayer coatings spread between these values. Initially, a decrease of λ results in an increase of the residual stresses, from 492 ± 32 MPa in the coating with $\lambda=1400$ nm to 684 ± 16 MPa in the one with $\lambda=300$ nm. For the coating with $\lambda=200$ nm, a slightly decreased tensile stress is observed. According to Holleck, different mechanisms have to be taken into account in the evaluation of stresses within multilayer coatings [31]. First, the difference in thermal expansion coefficients of TiN (9.4×10^{-6} K⁻¹) compared to TiB₂ ($\sim 7.4\times 10^{-6}$ K⁻¹) provokes thermal stresses at the interfaces. These are further accompanied by the stresses between the TiN base layer and cemented carbide ($\sim 5.8\times 10^{-6}$ K⁻¹) [32–35]. In addition, residual stresses at the various interfaces of TiN and TiB₂ have to be taken into account as well. The texture of the herein investigated coatings changes with the addition of B from texture-free for TiN to a preferred (110) orientation (TC=2.9) for TiBN. No pronounced influence of λ on the texture is observed in the multilayers, as all of them exhibit a preferred (110) orientation (TC=3.3±0.2).

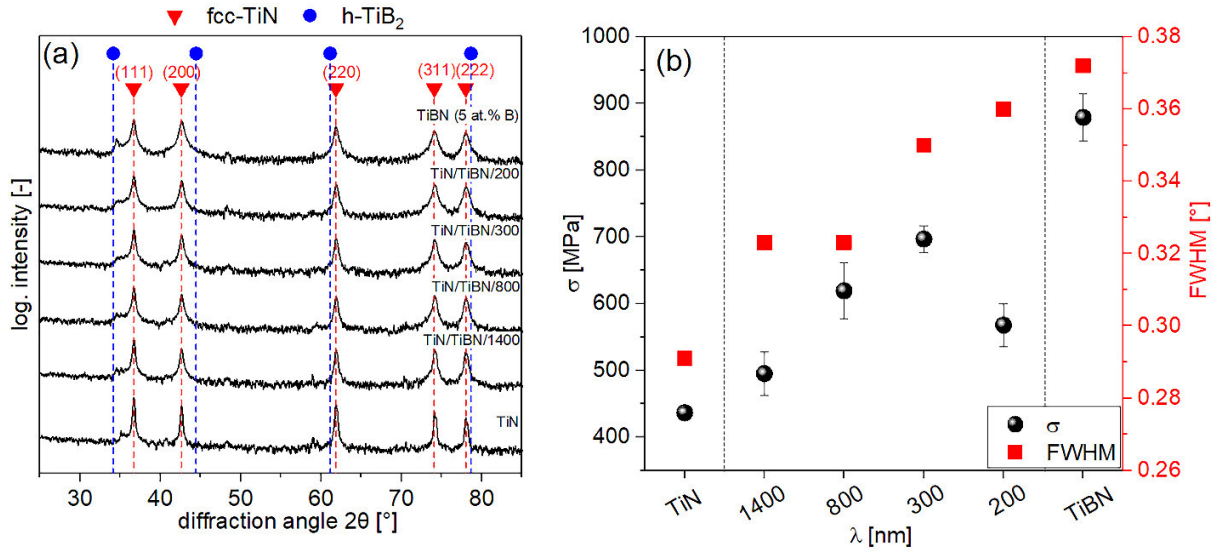


Fig. 2: a) Grazing incidence X-ray diffractograms and (b) FWHM and residual stresses of TiN and TiBN single-layers and TiN/TiBN multilayers.

To further illuminate the microstructure and phase composition of the multilayers, TEM analyses were performed. In Fig. 3 the related bright field (BF) TEM micrographs and the N K jump-ratios of the respective multilayer coatings are shown. The bright layers in the N K jump ratio micrographs correspond to a higher concentration of N and therefore to TiN. The in plane grain size decreases with decreasing λ from 140 ± 50 nm in the coating with $\lambda = 1400$ nm to 75 ± 10 nm in the one with $\lambda = 200$ nm. The observed behavior is in good accordance with the decreasing out-of-plane grain size with decreasing λ observed in the evolution of the FWHM in the XRDs.

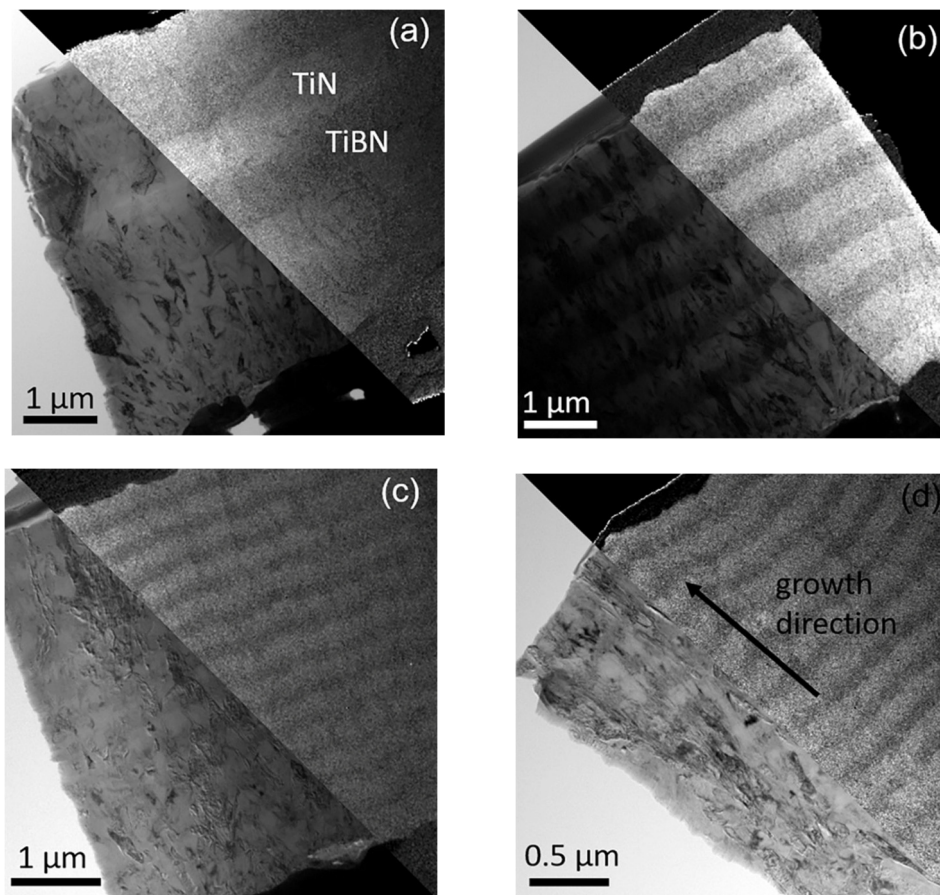


Fig. 3: BF-TEM micrographs (left) and NK jump-ratios (right) of the TiN/TiBN coatings with $\lambda =$ (a) 1400, (b) 800, (c) 300 and (d) 200 nm.

The electron energy loss near edge structure (ELNES) of the Ti $L_{2,3}$ and N K-edge of the coating with $\lambda = 1400$ nm, which is representative for the multilayers, is given in Fig. 4a. The presented patterns correspond to signals recorded in a TiN and a TiBN layer, respectively. The Ti $L_{2,3}$ and N K-edge can be unambiguously related to TiN [29,36,37]. From the B K-edge, shown in the insert in Fig. 4a, presence of B within the TiN layers can be concluded. Owing to the highly diffusive nature of B, diffusion from TiBN into TiN layers is not surprising. A further aspect that has to be taken into account is the residence of BCl_3 in the CVD recipient. Though the flow of the B precursor was interrupted in the TiN layers, remnants of BCl_3 in the gas compartment can still be incorporated into the coating. In addition, B carryover from TiBN into TiN layers during FIB preparation cannot entirely be excluded. In addition to the lower intensity of B in TiN compared to TiBN, a difference in the peak shape is apparent in Fig. 4a. It is therefore assumed, that the B atoms

in TiN and those in TiBN exist in a different chemical nature. While the B in TiN is incorporated as free B, comparison of the B K-edge of the TiBN layers with those reported in literature indicates the presence of TiB in the given coatings [36]. On the other hand, the signal could also result from a superimposition of the patterns from free B, TiB₂ and/or TiB. In good accordance to the XRD results, no indication for BN was found. The SAED patterns of the multilayer coatings showed spotty rings, which are characteristic for a polycrystalline sample with comparatively coarse grains (Fig. 4b and c). The d-spacings can nevertheless be assigned to the reported fcc-TiN phase and are in good agreement with the findings from XRD. The weak diffuse ring in the center of the pattern indicates the presence of an additional non-crystalline phase.

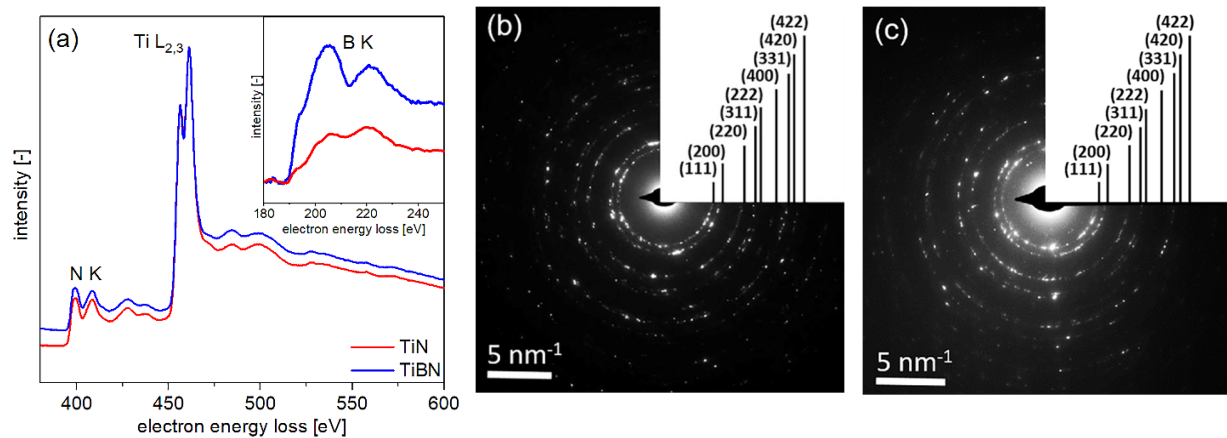


Fig. 4: TEM investigation of the TiN/TiBN multilayer coating with $\lambda=1400$ nm: (a) N K, Ti L_{2,3} edge and B K edge. SAED patterns with respective observed crystal planes of the multilayer coatings with (b) $\lambda=1400$ nm and (c) $\lambda=200$ nm.

Cross-sectional μ -Raman spectroscopy was used as a complementary method to XRD and TEM for the investigation of the phase composition within the system Ti-B-N. While detection of TiB upon XRD or SAED is not possible due to its amorphous nature, it is reported to result in a distinct signal in the Raman spectrum [29]. Fig. 5 shows the cross-sectional Raman spectra of single-layered TiN and TiBN as well as the respective layers within the multilayer coating with $\lambda=1400$ nm. The Raman signals at 220 cm⁻¹, 312 cm⁻¹ and 552 cm⁻¹ are attributed to the transversal acoustical, longitudinal acoustical and transversal optical mode, respectively, of TiN. The additional

peak at 350 cm^{-1} in the TiBN single-layer can be assigned to TiB, as the presence of h-TiB₂ should result in an additional peak at $\sim 660\text{ cm}^{-1}$ [29,38]. Formation of this compound is reported at low partial pressure of BCl₃ with a comparable feed gas composition as described in the present work [29,39]. The Raman spectrum of a TiBN layer within the multilayer coating with $\lambda=1400\text{ nm}$ displays a shoulder at 350 cm^{-1} , indicating the presence of small amounts of TiB also in the investigated multilayer coatings. The lower intensity of the characteristic peak for TiB in the TiBN layer within the multilayer coating compared to monolayered TiBN is assumed to result from the step size (250 nm) and spot size (750 nm), which does not allow to fully exclude influences from the neighboring TiN layers. Complementary XRD, ELNES, SAED and Raman spectroscopy have to be taken into consideration in order to clarify the phase composition in TiBN. Crystallographic investigations corroborate the assumption that additional phases (TiB, TiB₂) to fcc-TiN are formed. Nevertheless, residual free B in fcc-TiN cannot entirely be excluded. The signal of TiB in the Raman spectrum accompanied by the diffuse ring observed in the SAED confirm the formation of amorphous TiB, while XRD clearly displays the presence of h-TiB₂. Thus, it is concluded that the herein investigated TiBN coating consists to the most part of fcc-TiN and, to a small extent, of amorphous TiB and h-TiB₂.

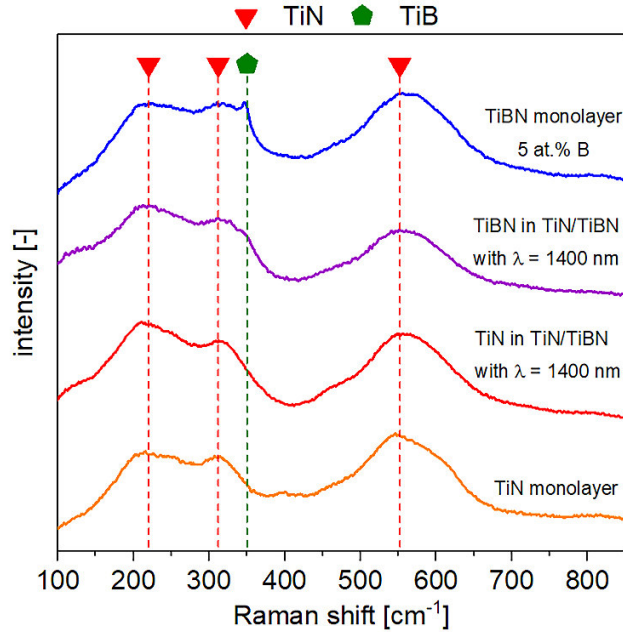


Fig. 5: Cross-sectional μ -Raman spectra of TiN and TiBN single-layers and the TiN/TiBN multilayer coating with $\lambda=1400$ nm.

3.2. Mechanical properties

Fig. 6a shows exemplary load-displacement curves, here recorded at 20 mN, of the six investigated coatings. The contact depth decreases both with addition of B to TiN and with decreasing bilayer period, indicating a higher resistance to plastic deformation. This trend is reinforced by the obtained values of coating hardness of the given samples shown in Fig. 6b. The pronounced hardness increase with addition of B is extensively discussed in the existing literature [2,26,27]. The rise in hardness from 18 ± 2 GPa for TiN to 29 ± 1 GPa for TiBN stems from the smaller crystallite size and consequently is a result of the Hall-Petch effect [40,41]. According to Barna *et al.*, highly-mobile dopants like B may segregate at the grain boundaries of the majority phase, where they prevent coalescence through formation of their own phase [42]. The decrement of λ results in a slight increase of hardness from 28 ± 3 GPa in the multilayered coating with the highest λ to 31 ± 2 GPa in the one with the lowest λ . However, the high distribution of the measurement values does not allow for a clear statement on the evolution of the hardness as a function of λ . The

prevention of dislocation motion at the increasing number of interfaces should result in strengthening with decreasing λ . Providing that sharp interfaces are present, bilayer periods of a few nm may enable the formation of superlattices, which may offer ultra-hardness [43]. However, a limitation in CVD is given due to the time needed for the gas exchange, which leads to the formation of less well-defined interfaces. Therefore, λ of the here investigated multilayer coatings was chosen within a range, where both the beneficial effects of low layer thickness and limitation arising from the deposition technique were considered. For the coatings with $\lambda=1400$ nm and $\lambda=700$ nm, the indentation depth was too low to cross the first interface between TiN and TiBN. Therefore, the high hardness measured within the indented TiN layer is most probably a result from the observed presence of small amounts of B within this layer. The Young's modulus stays in the magnitude reported for fcc-TiN with the addition of B and slightly decreases with reduction of λ . This behavior is associated with the increasing number of grain boundaries at the layer interfaces and the resulting higher porosity as λ decreases. The hardness to modulus ratio (H^3/E^2), which is related to the elastic strain to failure, allows a rough estimation of the fracture toughness [11]. Fig. 6c depicts the assessment of the H^3/E^2 -ratio of the investigated coatings. Both the addition of B and a decrease of λ result in a pronounced increase of the described ratio. The underlying phenomena, which influence the fracture toughness, are discussed in the following.

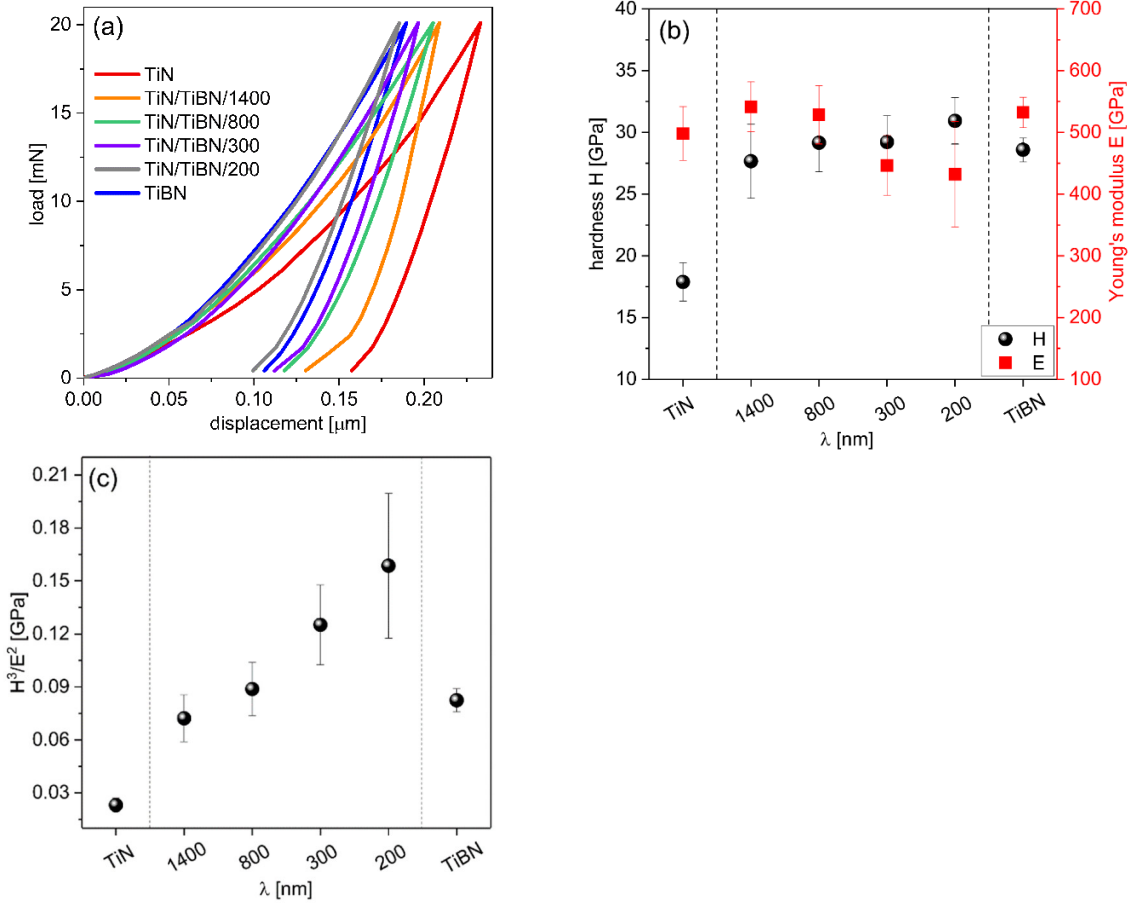


Fig. 6: (a) Exemplary load-displacement curves of TiN and TiBN single-layers and TiN/TiBN multilayers recorded at a load of 20 mN. (b) Evolution of hardness and Young's modulus as a function of the bilayer period in comparison to the respective single-layers. (c) The H^3/E^2 ratio as a measure of the resistance to plastic deformation for the TiN and TiBN single-layers and the TiN/TiBN multilayers.

In order to gain knowledge on the material properties at microscopic length scales, micromechanical tests with freestanding bending beams were performed. The geometry of an unnotched FIB fabricated specimen, which were used for the investigation of the fracture stress, is depicted in Fig. 7a. The used experimental setup further allows to determine the fracture toughness of the investigated samples, for which a sharp notch was implemented by FIB milling. Both, fracture stress and toughness were evaluated at the sudden end of the load-displacement curve, where failure of the micro-cantilevers occurred. Fig. 7b displays the evolution of the fracture properties of

single-layered TiN and TiBN as well as TiN/TiBN multilayers. The fracture stress increases from 3.9 ± 0.5 GPa in single-layered TiN to 7.3 ± 0.1 GPa in TiBN. Daniel *et al.* reported the strength of TiN coatings prepared by magnetron sputtering to be between 1.6 and 2.9 GPa depending on density and grain boundary design [44]. The higher strength value of TiN in the present work can be assigned to the different deposition technique and the dense microstructure resulting from the given deposition parameters. While TiN, TiB and TiB₂ all possess mixed ionic-covalent bonding character, the covalent bond fraction is higher in Ti-B compared to Ti-N. This is reflected by the higher strength of TiBN compared to TiN coatings. The maximum fracture stress in the multilayer coatings slightly increases with decreasing λ from a minimum value of 4.7 ± 0.5 GPa in the coating with $\lambda=800$ nm to 5.8 ± 0.5 GPa in the one with $\lambda=200$ nm. Thus, the strength of all multilayers spreads between the values observed in single layered TiN and TiBN. Despite the small increment of fracture stress with increasing layer number, the strength is obviously much more affected by the chemical composition compared to the layered architecture. The fracture strain of the single- and multilayer coatings, which corresponds to the ultimate strain of the cantilever before fracture, is roughly ~ 1 % for all of them. This low value is explained by the high Young's modulus and the brittle material properties of the herein investigated coatings.

Fracture toughness is of major importance in order to meet the high demands for hard coatings in metal cutting applications. In accordance with the improved hardness and strength with addition of B, the fracture toughness obtained from load-displacement curves for notched bending beams increases from 2.2 ± 0.4 MPa m^{1/2} for TiN to 5.0 ± 0.3 MPa m^{1/2} for TiBN. The improved fracture toughness of TiBN is associated with the presence of additional B-rich phases and the associated observed grain refinement. The superior fracture toughness in multilayer coatings relies on the deflection of cracks at the various interfaces of adjacent layers and the resulting delayed failure [10]. The increase of fracture toughness with decreasing λ verifies the energy dissipation on the crack tip between the respective layers. For the investigated specimens, the highest fracture toughness was observed in the multilayer with $\lambda=200$ nm showing a K_{IC} value of 5.8 ± 0.5 MPa m^{1/2}. The other multilayers display a fracture toughness lower than the one observed in single-layered TiBN. The H^3/E^2 -ratio therefore allowed a good estimation on the effect of B addition and

multilayering on the elastic strain to failure. Nevertheless, the H^3/E^2 -estimation indicated a higher fracture toughness compared to single-layered TiBN already in the coating with $\lambda=800$ nm. This mismatch though is not surprising owing to the different measurement principles, i.e. nanoindentation and micromechanical bending tests. Post-mortem analysis of the fracture cross-sections, which are displayed in Fig. 7c, allow a deeper insight into the failure mechanisms. Though all of the herein investigated coatings are ceramics and therefore generally display brittle material behavior, differences in the fracture cross-sections enable to explain the varying K_{IC} values. The fracture morphology of TiN suggests an inter-columnar fracture mechanism along the columnar TiN grain boundaries. This behavior is in accordance with the observations of Bhowmick *et al.* and results from the low cohesive energy between the individual columnar TiN grains [45,46]. In contrast, in single-layered TiBN crack propagation through the coating is inhibited by the small-grained structure, which is also true for the multilayers with low λ . Within these coatings, the blurred fracture morphology can be associated with an onset of ductile fracture behavior.

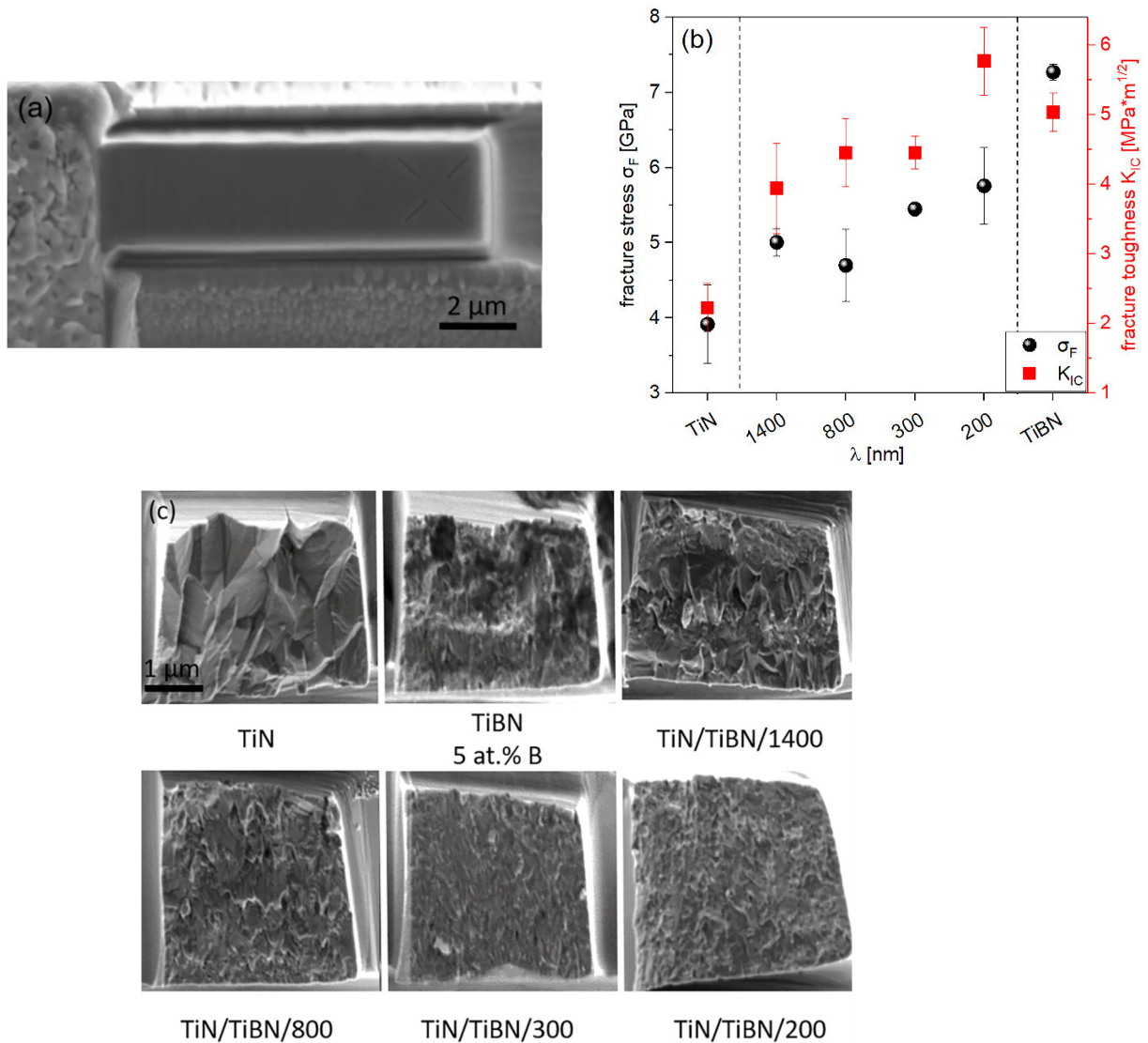


Fig. 7: (a) SE micrograph of an unnotched bending beam in top view. (b) Fracture stress and toughness of TiN and TiBN single-layers and the TiN/TiBN multilayers. (c) SE micrographs of post-mortem fracture cross-sections of unnotched bending beams.

4. Conclusions

Single-layered TiN and TiBN as well as four TiN/TiBN multilayers with different bilayer period λ (1400, 800, 300 and 200 nm) were grown by thermal CVD and their microstructure, phase composition and mechanical properties were investigated. The phase composition of TiBN layers within a multilayer stack was examined using a combinatorial approach of X-ray diffraction, ELNES

analysis, selected area electron diffraction and Raman spectroscopy and was found to consist of primarily fcc-TiN, co-existing with small amounts of h-TiB₂ and amorphous TiB. While the Young's modulus decreased with decreasing λ , both B addition and increasing layer number resulted in an increase of hardness. Miniature bending tests indicated a stronger dependence of the micromechanical properties on the phase composition compared to the coating architecture. Although less pronounced compared to the distinct increase with addition of B, an increase of the strength was observed with decreasing λ in the multilayers. The fracture toughness showed a strong dependence, both on the elemental composition and the layered coating architecture and was highest in the coating with $\lambda=200$ nm. Complementary nanoindentation and micromechanical bending tests lead to the conclusion that TiN/TiBN multilayers with small λ might offer high performance gains in cutting applications compared to single-layered TiN and TiBN.

Acknowledgements

The authors want to thank Bernhard Sartory (Materials Center Leoben) for the FIB and Dr. Walter Costin (Materials Center Leoben) for SEM work. Further, Dr. Marco Deluca (Materials Center Leoben) is acknowledged for the cross-sectional μ -Raman measurement, Gerhard Hawranek (Montanuniversität Leoben) for SEM work and Dr. Ilse Letofsky-Papst (Graz University of Technology) for the TEM investigations. The financial support by the Austrian Federal Ministry for Digital and Economic Affairs and the National Foundation for Research, Technology and Development is gratefully acknowledged.

References

- [1] W. Wallgram, U. Schleinkofer, Synthesis, structure, and behaviour of a new CVD TiB₂ coating with extraordinary properties for high performance applications, in: L.S. Sigl, P. Rödhammer, H. Wildner (Eds.), 17th Int. Plansee Seminar, Reutte, Austria, p. HM32.
- [2] H. Holzschuh, Thin Solid Films 469–470 (2004) 92–98.
- [3] W. Schintlmeister, W. Wallgram, J. Kanz, K. Gigl, Wear 100 (1984) 153–169.
- [4] P.H. Mayrhofer, M. Stoiber, C. Mitterer, Scripta Mater. 53 (2005) 241–245.

-
- [5] C. Mitterer, P.H. Mayrhofer, M. Beschliesser, P. Losbichler, P. Warbichler, F. Hofer, P.N. Gibson, W. Gissler, H. Hruby, J. Musil, J. Vlček, *Surf. Coat. Technol.* 120–121 (1999) 405–411.
- [6] P.H. Mayrhofer, C. Mitterer, *Surf. Coat. Technol.* 133–134 (2000) 131–137.
- [7] P. Losbichler, C. Mitterer, P.N. Gibson, W. Gissler, F. Hofer, P. Warbichler, *Surf. Coat. Technol.* 94–95 (1997) 297–302.
- [8] H. Holzschuh, Moderate Temperature CVD Coatings in the Ti–B–N system, in: G. Kneringer, P. Rödhammer, H. Wildner (Eds.), in: 16th International Plansee Seminar, Plansee Holding AG, Reutte, 2005, p. HM59.
- [9] L. Hultman, J. –E. Sundgren, Structure/Property Relationships for Hard Coatings, in: R.F. Bunshah (Ed.), *Handbook of Hard Coatings*, Noyes Publications, Park Ridge, New Jersey, 2001.
- [10] Y.X. Wang, S. Zhang, *Surf. Coat. Technol.* 258 (2014) 1–16.
- [11] A. Leyland, A. Matthews, *Wear* 246 (2000) 1–11.
- [12] M. Stoiber, E. Badisch, C. Lugmair, C. Mitterer, *Surf. Coat. Technol.* 163–164 (2003) 451–456.
- [13] M. Stoiber, C. Mitterer, T. Schoeberl, E. Badisch, G. Fontalvo, *J. Vac. Sci. Technol. B* 21 (2003) 1084–1091.
- [14] M. Stoiber, S. Perlot, C. Mitterer, M. Beschliesser, C. Lugmair, R. Kullmer, *Surf. Coat. Technol.* 177–178 (2004) 348–354.
- [15] M. Tkadletz, N. Schalk, C. Mitterer, J. Keckes, M. Pohler, C. Czettl, *Int. J. Refract. Met. Hard Mater.* 71 (2018) 280–284.
- [16] U. Welzel, J. Ligot, P. Lamparter, A.C. Vermeulen, E.J. Mittemeijer, *J. Appl. Crystallogr.* 38 (2005) 1–29.
- [17] J. Almer, U. Lienert, R.L. Peng, C. Schlauer, M. Odén, *J. Appl. Phys.* 94 (2003) 697–702.
- [18] I.C. Noyan, J.B. Cohen, *Residual Stress: Measurement by Diffraction and Interpretation*, Springer–Verlag, New York, 1987.
- [19] M.H. Müller, W.P. Chernock, P.A. Beck, *Trans. Metall. Soc. AIME.* 212 (1958) 39–40.
- [20] W.C. Oliver, G.M. Pharr, *J. Mater. Res.* 7 (1992) 1564–1583.
- [21] K. Matoy, H. Schönherr, T. Detzel, T. Schöberl, R. Pippan, C. Motz, G. Dehm, *Thin Solid Films* 518 (2009) 247–256.

- [22] H. Nowotny, F. Benesovsky, C. Brukl, O. Schob, *Monatsh. Chem.* 92 403–414.
- [23] J. Wagner, C. Mitterer, M. Penoy, C. Michotte, W. Wallgram, M. Kathrein, *International Journal of Refractory Metals and Hard Materials* 26 (2008) 120–126.
- [24] International Centre for Diffraction Data, PDF–2 Release, Card number 00–038–1420, 2018.
- [25] International Centre for Diffraction Data, PDF–2 Release, Card number 03–065–1073, 2018.
- [26] H. Holzschuh, *Int. J. Refract. Met. Hard Mater.* 20 (2002) 143–149.
- [27] J. Wagner, D. Hochauer, C. Mitterer, M. Penoy, C. Michotte, W. Wallgram, M. Kathrein, *Surf. Coat. Technol.* 201 (2006) 4247–4252.
- [28] J.L. Peytavy, A. Lebugle, G. Montel, *High Temperatures – High Pressures* 10 (1978) 341–345.
- [29] I. Dreiling, C. Raisch, J. Glaser, D. Stiens, T. Chassé, *Surf. Coat. Technol.* 206 (2011) 479–486.
- [30] B.D. Cullity, *Elements of X-ray Diffraction*, Addison–Wesley, Reading Massachusetts, 1978.
- [31] H. Holleck, M. Lahres, P. Woll, *Surf. Coat. Technol.* 41 (1990) 179–190.
- [32] R.G. Munro, *J. Res. Natl. Inst. Stand. Technol.* 105 (2000) 709–720.
- [33] H.O. Pierson, *Handbook of refractory carbides and nitrides: properties, characteristics, processing, and applications*, Noyes Publications, New York, 1996.
- [34] S. Madtha, C. Lee, K.S. Ravi Chandran, *J. Am. Ceram. Soc.* 91 (2008) 1319–1321.
- [35] H. Wang, T. Webb, J.W. Bitler, *Int. J. Refract. Met. Hard Mater.* 49 (2015) 170–177.
- [36] A. Gupper, A. Fernández, C. Fernández–Ramos, F. Hofer, C. Mitterer, P. Warbichler, *Monatsh. Chem.* 133 (2002) 837–848.
- [37] C. López–Cartes, D. Martínez–Martínez, J.C. Sánchez–López, A. Fernández, A. García–Luis, M. Brizuela, J.I. Oñate, *Thin Solid Films* 515 (2007) 3590–3596.
- [38] I. Dreiling, A. Haug, H. Holzschuh, T. Chassé, *Surf. Coat. Technol.* 204 (2009) 1008–1012.
- [39] M. Nadal, T. Grenet, F. Teyssandier, *J. Phys. IV France* 03 (C5) (1993) 809–814.
- [40] E.O. Hall, *Proc. Phys. Soc. Lond.* 64 (1951) 747–753.
- [41] N.J. Petch, *J. Iron Steel Inst. London.* 173 (1953) 25–28.
- [42] P.B. Barna, M. Adamik, J. Lábár, L. Kövér, J. Tóth, A. Dévényi, R. Manaila, *Surf. Coat. Technol.* 125 (2000) 147–150.
- [43] S. Zhang, D. Sun, Y. Fu, H. Du, *Surf. Coat. Technol.* 167 (2003) 113–119.

-
- [44] R. Daniel, M. Meindlhumer, W. Baumegger, J. Zalesak, B. Sartory, M. Burghammer, C. Mitterer, J. Keckes, *Acta Mater.* 122 (2017) 130–137.
- [45] S. Bhowmick, Z.-H. Xie, M. Hoffman, V. Jayaram, S.K. Biswas, *J. Mater. Res.* 19 (2004) 2616–2624.
- [46] A. Zeilinger, J. Todt, C. Krywka, M. Müller, W. Ecker, B. Sartory, M. Meindlhumer, M. Stefenelli, R. Daniel, C. Mitterer, J. Keckes, *Sci. Rep.* 6 (2016) 22670.

Publication II

The Effect of B and C Addition on Microstructure and Mechanical Properties of TiN Hard Coatings grown by Chemical Vapor Deposition

Christina Kainz, Nina Schalk, Michael Tkadletz, Christian Mitterer, Christoph Czettl

Thin Solid Films 688 (2019) 137283



The Effect of B and C Addition on Microstructure and Mechanical Properties of TiN Hard Coatings grown by Chemical Vapor Deposition

Christina Kainz^{1*}, Nina Schalk¹, Michael Tkadletz², Christian Mitterer², Christoph Czettel³

¹ Christian Doppler Laboratory for Advanced Coated Cutting Tools at the Department of Materials Science, Montanuniversität Leoben, Franz Josef Straße 18, 8700 Leoben, Austria

² Department of Materials Science, Montanuniversität Leoben, Franz Josef Straße 18, 8700 Leoben, Austria

³ Ceratizit Austria GmbH, Metallwerk Plansee Straße 71, 6600 Reutte, Austria

Keywords: CVD, Ti(B,C)N, hard coatings, TEM, micro-mechanical testing

Abstract

Incorporation of additional elements into TiN grown by chemical vapor deposition (CVD) provides an opportunity to enhance the performance of hard coatings used for the protection of cutting tools in the demanding metal processing industry. Within the present work, the hardness, Young's modulus and fracture behavior of CVD coatings within the quaternary system Ti(B,C)N are correlated with their chemical composition and microstructure. TiN, TiBN, TiCN and TiBCN coatings were prepared in an industrial-scale thermal CVD plant by variation of the precursors. X-ray diffraction revealed the majority phase to be face-centered cubic within all investigated coatings, accompanied by small amounts of hexagonal TiB₂ in both B-containing coatings and amorphous TiB in TiBN. Transmission electron microscopy unveiled grain refinement and an increment of structural defects, when B, C or a combination thereof is added to TiN. Complementary nanoindentation and micro-mechanical bending tests identified the quaternary TiBCN as the optimum choice with respect to hardness (32.2 ± 1 GPa), Young's modulus (587 ± 29 GPa) and fracture stress (8.5 ± 0.4 GPa). Fracture toughness was superior in the B containing coatings compared to TiN and TiCN with the highest value observed in TiBN (5.0 ± 0.3 MPa m^{1/2}). A post-mortem elevation profile of micro beams' fracture cross-sections verified, that within the B

containing coatings the crack is deflected more effectively normal to the crack propagation direction in comparison to TiN and TiCN.

1 Introduction

As a reaction to increasing industrial demands, the continuing development of sophisticated hard protective coatings for the metal cutting industry is crucial. Both, physical and chemical vapor deposition (CVD) are well suited to grow protective hard coatings onto cemented carbide indexable inserts, where they significantly increase the tool's application performance [1]. Although TiN coatings offer chemical stability and good wear resistance, strengthening is necessary for machining of advanced steel or Ti-based workpiece materials [2]. Therefore, over the last decades a variety of possible additional elements to TiN has been reported in literature. The required improvement of hardness is achieved through grain refinement, as obtained with addition of B or Si [3,4] or through solid solution strengthening by adding C or Al [5,6]. While a smooth nano-scaled microstructure can be observed in TiBN within a broad composition range, the microstructure of CVD TiCN is highly affected by the ratio of C/(C+N). Here, a high N content results in a globular structure, whereas C rich TiCN coatings are characterized by columnar grains [7]. A combinatorial approach of both B and C addition in CVD Ti(B,C)N was reported by Holzschuh *et al.*, who correlated the chemical composition of quaternary TiBCN coatings with their performance in cutting tests [8]. Czettel *et al.* found the microstructure of CVD TiBCN coatings to be defect-controlled and reported a hardness increase compared to TiCN already for small amounts of B [9]. Consequential to their promising mechanical properties and versatile microstructures, literature on CVD TiBN, TiCN and TiBCN coatings is comprehensive [5,8,10]. However, the existing reports focus only on comparisons within one of the mentioned coating systems, but are lacking a correlation between the presence of B, C or a combination thereof and their mutual influence on the coating properties within CVD Ti(B,C)N coatings.

Thus within this work, a juxtaposition of TiN, TiBN, TiCN and TiBCN with respect to their composition-dependent microstructure, mechanical properties and microscopic fracture behavior is presented. The complementary use of crystallographic, microscopic and spectroscopic

characterization methods allowed a detailed insight into the microstructure and phase composition of Ti(B,C)N coatings. In addition to the composition-dependent hardness of the coatings, micromechanical bending tests were applied to identify the strongest and toughest of the investigated samples.

2 Experimental details

TiN, TiBN, TiCN and TiBCN coatings were deposited in an industrial-scale thermal CVD plant. A gas mixture of TiCl₄, H₂, N₂ and Ar was used to synthesize TiN. While for the deposition of TiBN BCl₃ was added, CH₄ was used as C precursor in order to prepare a TiCN coating. TiBCN was obtained through the simultaneous use of all aforementioned precursors. Within the B-containing coatings, the BCl₃ gas flow was adjusted to ~0.2 vol.%, while for the C containing samples a CH₄ fraction of ~6 vol% within the feed gas was applied. All coatings were deposited at a temperature of ~925 °C and a base pressure of 930 mbar onto a ~0.5 μm thick TiN base layer. The total coating thicknesses were between 4 and 5 μm. Coatings were grown on cemented carbide cutting inserts in SEKN 1203 geometry (according to ISO 1832) with a composition of 87 wt.% WC, 9 wt.% Co and 4 wt.% mixed carbides.

The elemental composition of the TiN and TiCN coatings was determined by a combination of energy and wavelength dispersive X-ray spectroscopy (EDX, WDX) with an Oxford Instruments INCA and an Oxford Instruments INCAWave extension to a Zeiss EVO50 scanning electron microscope (SEM). Within this combined measurement, the elemental composition of Ti was determined using EDX, while for the lighter elements N and C WDX was applied. C was quantified in comparison to five Fe-C alloys with known composition, Ti using the pure element, N by means of TiN and B in comparison to TiB₂ coating standards calibrated by elastic recoil detection analysis (ERDA). The composition of the B containing coatings was additionally evaluated by ERDA using a 43 MeV ³⁵Cl⁷⁺ ion beam, due to the higher accuracy especially for light elements [11]. The morphologies of surface and cross-section of the coatings were surveyed by an in lens detector using a field emission gun SEM of type Zeiss Auriga. Phase analysis and residual stress evaluation was conducted by X-ray diffraction (XRD) using a Bruker AXS D8 Advance diffractometer with Cu-K_α

radiation. Measurements in grazing incidence geometry with an incidence angle of 3° were applied to illuminate the microstructure of the coatings. Recording the diffraction data in Bragg-Brentano geometry allowed the assessment of the preferred orientation using texture coefficients [12]. There, texture-free intensities $I_0(hkl)$ of face-centered cubic (fcc) TiN and fcc-TiCN were used [13,14]. In both cases, seven reflections were considered for calculation, i.e. (111), (200), (220), (311), (331), (420) and (422). The residual stress was determined using the $\sin^2\psi$ method on the same diffractometer. For this purpose, the measurement was conducted in iso-inclination set-up on the (422) peak [15]. Recording of Raman spectra using a LabRAM HR800 spectrometer from Horiba Jobin-Yvon with a frequency-doubled Nd-YAG laser ($\lambda = 514.5$ nm) provided supplementary information on the phase composition. Lamellae for the transmission electron microscopic (TEM) investigations were prepared by focused ion beam (FIB) milling in a FIB/SEM dual beam microscope of type Nova200 from FEI. The lamellae were investigated using a FEI Tecnai F20 energy-filtered microscope, which was equipped with a Schottky field emitter operating at a voltage of 200 kV. In order to obtain the electron energy loss spectra (EELS) of the respective coatings, the device was operated in imaging mode.

Indentation hardness and Young's modulus were measured using a UMIS nanoindenter from Fischer-Cripps Laboratories with a diamond Berkovich indenter. A plateau test was carried out in a load range between 30 and 10 mN with an increment of 1 mN. Data was analyzed accordingly to the Oliver and Pharr method [16]. Bending tests, performed on free-standing micro-cantilevers, were conducted to gain insight into the fracture behavior of the coatings. For that purpose, the cutting inserts were initially mechanically cut and the cross-section was ion sliced using an IonSlicer 4000+ by Hitachi. The bending beams were fabricated using a FEI DualBeam Versa 3D FIB device, equipped with an Everhart-Thornley detector. Removal of coating material around and substrate material underneath the bending beam was realized by FIB milling at a current of 3 nA. Special emphasis was laid on avoiding the presence of coating inherent tensile cracks within the test specimen. Cleaning from re-deposited material and adjustment of the precise beam dimensions was realized with a cutting current of 1 nA. A minimum of three notched and unnotched specimen each, featuring a bending length of ~ 9 μm and a cross-section of $\sim 3 \times 3$ μm^2 , were tested to obtain reasonable

statistics. Fracture stress of the coatings was determined using the unnotched beams. Beams with a sharp notch, which was introduced $\sim 1 \mu\text{m}$ away from the cantilevers' support, provided conclusions on the fracture toughness of the investigated samples. Using a Hysitron TriboIndenter TI950, equipped with a sphero-conical diamond tip (radius = 700 nm), the micro cantilevers were tested applying a load-controlled function. Verification of the depth of the FIB-made notch and analysis of the fracture cross-section morphology were done by post mortem SEM investigations using the above mentioned Zeiss Auriga field emission gun SEM. With respect to the bending beams' geometries and the recorded load-displacement curves, data analysis was conducted accordingly to the method proposed by Matoy *et al.* [17]. A three dimensional visualization of the crack propagation was realized applying the software package Alicona MEX by overlaying three SEM micrographs recorded at different tilting angles. The average elevation profiles of the fracture cross-sections were obtained by cross-sectional line scans at three different positions on one tested micro-beam specimen for each coating.

3 Results and discussion

3.1 Microstructure and chemical composition

The elemental compositions of the coatings are listed in Table 1. While the B content of TiBN measured by WDX (5 at.%) correlated well with the results obtained through ERDA (7 at.%), a significant discrepancy between WDX (1 at.%) and ERDA (6 at.%) was observable for TiBCN. Since ERDA is assumed to be more precise for the determination of light elements, in the following, the composition of TiBN and TiBCN refers to this measurement. For the B free coatings, in-house standards allowed to determine the composition with a high degree of accuracy (compare section 2).

Table 1: Elemental composition of the investigated coatings.

	TiN	TiCN	TiBN		TiBCN	
	EDX/WDX	EDX/WDX	EDX/WDX	ERDA	EDX/WDX	ERDA
Ti [at.%]	50	52	51	46	46	41
N [at.%]	50	34	44	47	34	32
C [at.%]	—	14	—	—	19	21
B [at.%]	—	—	5	7	1	6

For the investigated TiBN coating, the addition of 7 at.% B to TiN has no noteworthy influence on the stoichiometric ratio between Ti and N. The composition of this sample lies close to the quasi-binary tie line of TiN-TiB₂ within the ternary phase field of TiN-TiB₂-BN [18]. Contrary, the addition of C results in a significant decrease of the N content in favor of C, which is due to the formation of a TiCN solid solution, where C replaces N in the unit cell. According to the C, N and B content in the coatings, the normalized composition of TiCN and TiBCN is TiC_{0.3}N_{0.7} and TiB_{0.1}C_{0.36}N_{0.54}, respectively. Hence, the addition of B to TiCN results in an increase of the C/(C+N) ratio. Furthermore, the presence of B decreases the Ti content within the coatings, which is reflected in a slight sub-stoichiometry in TiBN and a pronounced one in TiBCN. A possible explanation for this could be, that B provokes the presence of metal vacancies in coatings within the system Ti(B,C)N. As a consequence of the thermodynamic stability of the applied CH₄ precursor, the nominal C-content in TiCN and TiBCN is low compared to literature values of coatings prepared with CH₃CN in the medium temperature CVD process [19,20].

The change in the elemental composition is already reflected by variations in the color of the coatings, as shown within the inserts in Fig. 1. While the addition of B to the golden TiN results in a bronze tint of the coating, TiCN displays a black metallic hue and TiBCN is grey colored. The SEM micrographs in Fig. 1 provide insights into the surface and cross-section morphologies of the coatings. TiN is characterized by a surface morphology consisting of star shaped and pyramidal crystals (Fig. 1a), as was also reported by Wagner *et al.* for CVD TiN deposited at comparable

temperatures [5]. The FIB cross-section reveals a competitive grain growth with columnar grains of about $0.5\ \mu\text{m}$ in-plane grain width, which in growth direction partly extend over the whole coating thickness. The surface of TiBN (Fig. 1b) resembles the one of TiN accompanied by fine needles. A fine grained morphology with herringbone features can be observed in the cross-section of TiBN, which is in good accordance with the well-reported nanocrystallinity of TiBN [21–23]. Estimation of the grain size from the SEM cross-sectional micrographs is not possible for TiBN due to the small grained morphology, which is also true for TiBCN. Albeit less pronounced compared to TiBN, TiCN as well displays finer grains compared to TiN. From the globular cross-sectional morphology shown in Fig. 1c, the grain size can be estimated to roughly $170\ \text{nm}$. Facetted grains, which shape the surface morphology of this coating, were also reported by Cheng *et al.* for a C-content and deposition temperature comparable to the one applied within the present work [7]. Fig. 1d displays the hillock surface morphology of TiBCN with needles similar to the ones observed in the top-view micrograph of TiBN. From the cross-section, a combined morphology between the herringbone structure of TiBN and the globular grains of TiCN can be observed. The presence of CH_4 in the feed gas resulted in a decrease of the deposition rate, from $2.06\pm 0.03\ \mu\text{m}/\text{h}$ and $2.10\pm 0.08\ \mu\text{m}/\text{h}$ for TiN and TiBN, respectively, to $1.91\pm 0.09\ \mu\text{m}/\text{h}$ for TiCN and $1.75\pm 0.12\ \mu\text{m}/\text{h}$ for TiBCN.

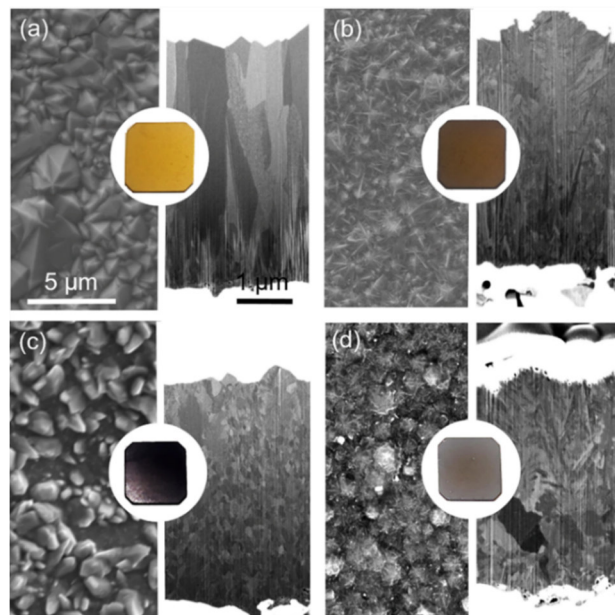


Fig. 1: Photographs and SEM images of surface and FIB cross-section morphologies of a) TiN, b) TiBN, c) TiCN and d) TiBCN.

The microstructural and phase analysis was done by XRD and the obtained diffractograms are summarized in Fig. 2. Standard peak positions of fcc-TiN, fcc-TiC and hexagonal (h)-TiB₂ are added to the diffractograms as dashed lines [13,24,25]. All peaks observed in the TiN coating can be assigned to the fcc-TiN phase [24]. Peak broadening of TiN is lowest within all the here investigated samples, which correlates well with the coarse grained microstructure of this coating evident from Fig. 1a. The smaller grain size and increase in micro strains of TiBN is reflected in a more pronounced peak broadening (Fig. 2) [26]. The additional small peak at $2\theta = 34.6^\circ$ can be assigned to h-TiB₂, as previously reported [21,27]. A detailed Rietveld peak refinement showed, that the lattice parameter is largely unaffected by the addition of B, yielding about 4.24 Å. Compared to TiN and TiBN, a peak shift in the diffractograms is observable in the C-containing coatings, resulting from the formation of a TiCN solid solution. Assuming that the lattice parameter exhibits a Vegard's like behavior between pure TiN and TiC, the measured lattice parameter of 4.27 Å of TiCN is in good agreement with the C to N ratio mentioned in Table 1 [13,25]. Addition of B to TiCN again results in grain refinement, as confirmed by the more pronounced peak broadening. Ancillary to the fcc-TiCN phase, formation of the h-TiB₂ phase can be assumed, but is obviously less distinct compared to TiBN. While this becomes obvious already from a qualitative comparison of the two B containing coatings presented in Fig. 2, Rietveld refinement showed a noteworthy decreased phase fraction of h-TiB₂ in TiBCN (< 1 wt.%) compared to TiBN (~7 wt.%). Peak fitting by Rietveld refinement reinforced the trend of the observed peak broadening: TiN and TiCN exhibit coarser grains in comparison to the B containing counterparts. While the given trend is reliable, absolute values need to be interpreted with caution, as the fit was conducted on coatings and not on powdered samples. For that reason, actual values are not given here. The additional presence of amorphous TiB in the investigated TiBN coatings was verified by Raman spectroscopy [27]. On the contrary, the characteristic Raman signal for TiB at 350 cm⁻¹ could not be observed in the quaternary TiBCN coating, which is in good agreement with Raman studies of CVD TiBCN conducted by other authors [28]. The absence of this phase is assumed to be attributed to thermodynamic limitations as soon as C is present in the system.

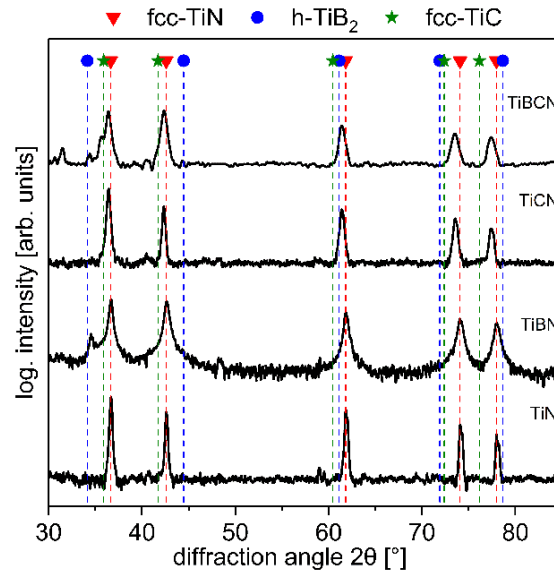


Fig. 2: Grazing incidence X-ray diffractograms of the investigated $Ti(B,C)N$ coatings.

Detailed microstructural investigations by TEM, shown in Fig. 3, allowed to take a further step towards a solid understanding of the influence of B and C on the microstructure of $Ti(B,C)N$ coatings. The microstructure of the coarse grained TiN (Fig. 3a) is characterized by a low number of defects, which is illustrated in the high magnification image in the insert. Addition of both, B and C, to TiN results in a significant increase of the defect density within the coatings, which is observable from the high magnification micrographs in the inserts of Fig. 3b-d. The needle-like appearance of TiBN (Fig. 3b) correlates well with the surface morphology observed by SEM (Fig. 1b). In contrast to coarse grained TiN and TiCN, a reasonable estimation of the grain size from the SEM images was not possible for the B containing coatings. However, TEM micrographs allowed to estimate the grain size to roughly 60 nm and 50 nm for TiBN and TiBCN, respectively.

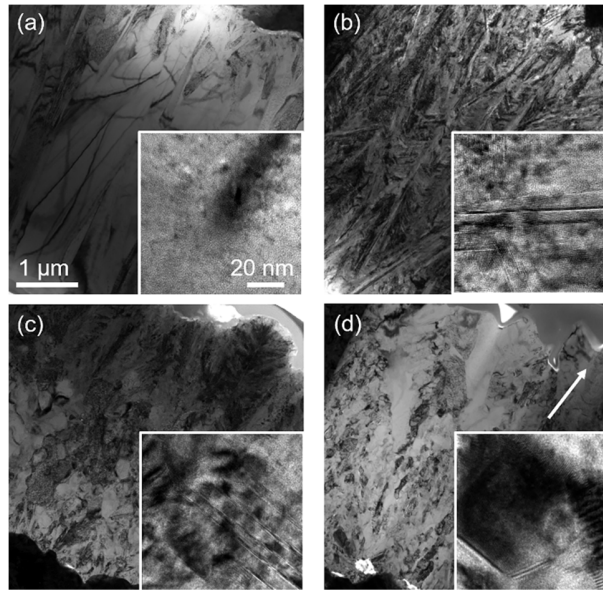


Fig. 3: TEM micrographs of the investigated $Ti(B,C)N$ coatings. Overview: Bright field (BF) TEM micrographs of a) TiN , b) $TiBN$, c) $TiCN$ and d) $TiBCN$ coatings. The white arrow indicates the growth direction. Inserts: BF images at higher magnifications reveal increased incidence of defects, when B or C is added to TiN .

The electron energy loss near edge structure (ELNES) of Ti, N, C and B recorded for the four different coatings allows further conclusions on phase composition and is presented in Fig. 4. While the recorded Ti $L_{2,3}$ and the N K ELNES resemble those of pure TiN (Fig. 4a), the fine structures of the B K and C K-edge verify the presence of additional species [29]. In comparison with measurements reported by Gupper *et al.*, the shape and peak maxima of the B K-edge of $TiBN$ (Fig. 4b) speak in favor of a superimposition of amorphous TiB and $h-TiB_2$ [30]. The different shape of the B K fine structure recorded for $TiBCN$ compared to $TiBN$ underlines the difference in the phase composition of the ternary and quaternary B containing coatings. Taking into account the lack of the characteristic Raman signal for TiB , the weak intensity of the $h-TiB_2$ phase observed by XRD and the elemental composition of $TiBCN$, the incorporation of B into the fcc- $TiCN$ lattice can reasonably be assumed. The fact that the $TiCN$ lattice is stronger distorted than that of TiN (compare Fig. 3a and c) may explain the stronger tendency of B incorporation into the lattice of $TiBCN$ in comparison to $TiBN$. However, the low intensity of the B K edge within the quaternary coating and the lack of distinctive peaks do not allow an unambiguous statement on phase

composition. The C K ELNES recorded for TiCN and TiBCN (Fig. 4c) do not vary significantly from each other and are in good agreement with the energy position and relative intensities of TiC reported in literature [31]. Site specific determination of the composition was realized through conduction of an EELS line scan including two neighboring grains and their grain boundary within each scan. No significant difference of the B content within the grains compared to that of the grain boundaries was observable for the investigated TiBN. This finding also applies for the distribution of B and C within TiCN and TiBCN.

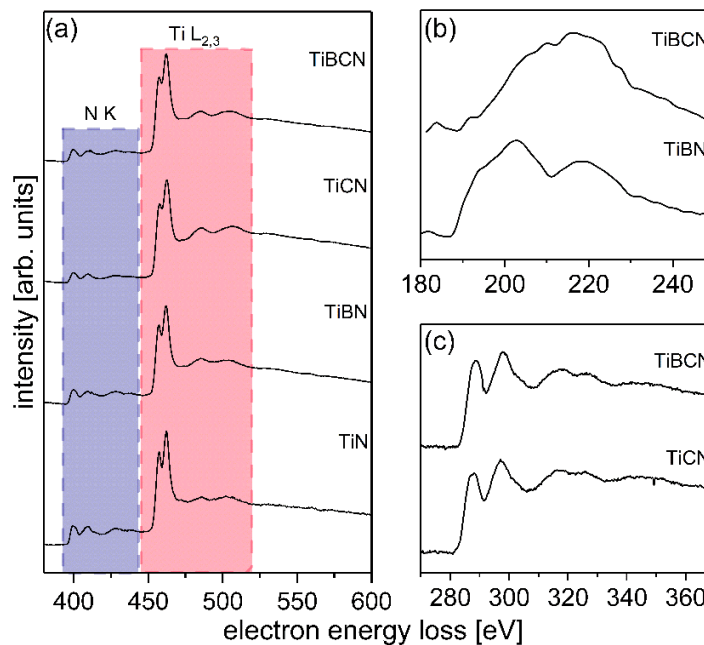


Fig. 4: Normalized ELNES of the investigated $Ti(B,C)N$ coatings. (a) Comparison between the $Ti L_{2,3}$ (red) and $N K$ (blue), (b) the $B K$ and (c) the $C K$ -edge.

3.2 Mechanical properties

Hardness, Young's modulus and residual stresses of the investigated coatings are summarized in Fig. 5. B addition to TiN results in a pronounced hardness increase from 18 ± 2 GPa for TiN to 29 ± 1 GPa for TiBN. This is on the one hand reasoned by Hall-Petch hardening as a result of grain refinement with addition of B [8,22,32,33]. Furthermore, the higher covalent bonding fraction due to formation of a B-containing fcc-TiN based solid solution, incorporated hard B-containing phases and

increased defect density are suggested to positively affect the coating hardness [34]. The intermediate grain size and defect density of TiCN is reflected by a moderate hardness of 25 ± 1 GPa. Among the investigated coatings, the highest hardness was observed for TiBCN (32 ± 1 GPa), which is attributed to the most pronounced defect density, smallest grain size and highest fraction of covalent bonding partners. Both, the apparent trend and the absolute values of the hardness are in good agreement with results on CVD Ti(B,C)N coatings reported by other authors [5,8,9,21]. The conducive effect of additional elements on TiN is also reflected by the Young's modulus, where again TiBCN displays the topmost value of 587 ± 29 GPa. According to the hardness to modulus ratio (H^3/E^2), the presence of additional elements in TiN-based coatings positively affects the resistance to plastic deformation [35]. An increase of H^3/E^2 by a factor of 2.18 for TiCN, 3.57 for TiBN and 4.20 for TiBCN compared to TiN indicates a beneficial resistance to dislocation movement in the ternary and quaternary coatings. The presence of B results in a significant increase of the tensile residual stresses compared to the B free counterparts (see Fig. 5). While the stresses of TiN and TiCN account only for 437 ± 7 and 413 ± 18 MPa, respectively, values of 879 ± 36 MPa in TiBN and 897 ± 87 MPa in TiBCN were determined. It is suggested, that the smaller grain size and the thus higher number of grain boundaries in the B containing coatings entails an increase of tensile stress. This is attributed to the higher fraction of grain boundaries resulting in an increase of the thermal expansion coefficient (TEC) [36]. As a result, a more pronounced mismatch of the TECs of TiN ($9.3\times 10^{-6}/\text{K}$) and TiCN ($\sim 8.0\times 10^{-6}/\text{K}$) in comparison to that of the cemented carbide substrate ($\sim 5.2\times 10^{-6}/\text{K}$) [37,38] is caused. The higher stresses in the B containing coatings furthermore suggests that these coatings withstand the cooling step during the deposition without crack formation in comparison to TiN and TiCN.

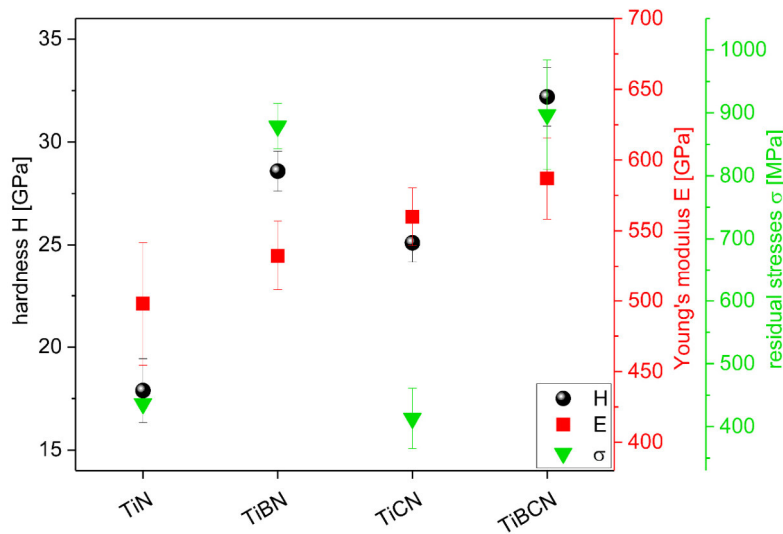


Fig. 5: Hardness, Young's modulus and residual stresses of the investigated Ti(B,C)N coatings.

Bending tests on free-standing coating micro-cantilevers were conducted to investigate the effect of B and C addition on the fracture behavior of CVD TiN coatings. An exemplary unnotched micron-sized fracture-mechanical sample used for the investigation of the fracture stress is depicted in Fig. 6a. Testing of bending beams featuring a sharp notch allowed to assess the fracture toughness of the investigated coatings [17]. Both, fracture stress and toughness were determined at the maximum load applied, where failure of the bending beams was signified through the sudden drop of the load-displacement curve. All recorded curves reflect linear elastic bending behavior until fracture, as one would expect for brittle ceramic materials. The increase of the fracture stress with addition of B and C to TiN is clearly evident from the exemplary load displacement curves depicted in Fig. 6b. The coatings' strength increases from 3.9 ± 0.5 GPa in TiN to 7.3 ± 0.1 GPa and 8.1 ± 0.6 GPa in TiBN and TiCN, respectively. Taking into account different deposition techniques and test set-ups, these values are in reasonable agreement with data reported in literature [39,40]. Going hand in hand with the topmost hardness and Young's modulus, TiBCN with a fracture stress of 8.5 ± 0.4 GPa outperforms the binary and ternary coatings. The beneficial influence of C and B on the coatings' strength can be ascribed to Hall Petch strengthening, an increased fraction of covalent bonding character within the fcc-TiN based solid solution, the formation of hard B-containing phases and defect hardening. In accordance to the brittle nature of ceramic materials, the fracture strain is ~ 1 % for TiN and TiBN and ~ 2 % for the C containing coatings.

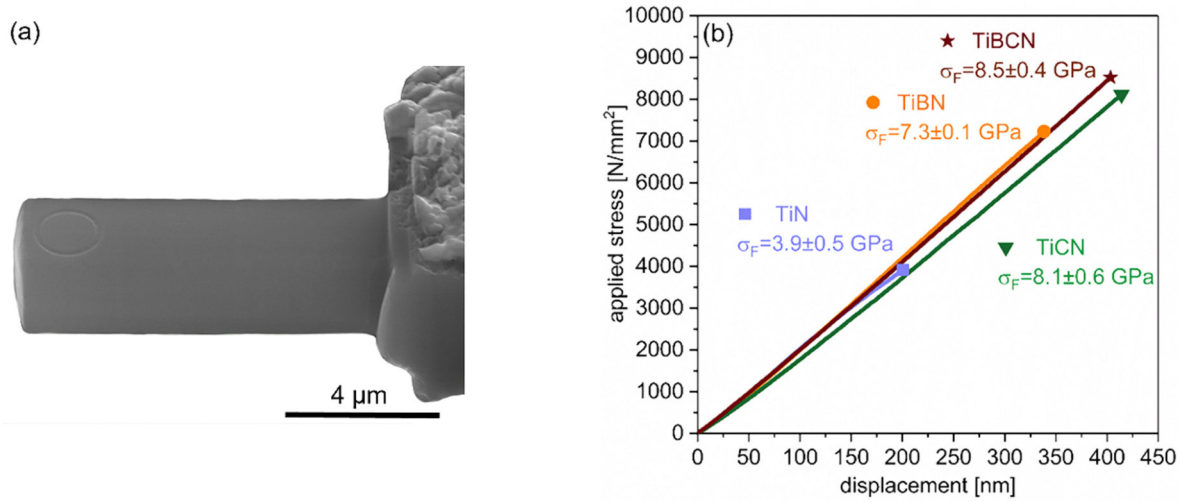


Fig. 6: (a) SEM image of an exemplary unnotched bending beam (TiBCN) used for the determination of the fracture stress. The image was obtained using a FEI DualBeam FIB Versa 3D. The circle at the edge of the beam was added by FIB milling to facilitate subsequent identification of the planned indentation position with the nanoindenter tip. (b) Exemplary load-displacement curves of unnotched micro-cantilever beam specimens.

In addition to hardness, Young's modulus and strength, also high fracture toughness is beneficial for coatings being applied in metal cutting. All of these mentioned properties are enhanced by the addition of C to TiN. Hereafter, the stress intensity factor K_{IC} , calculated accordingly to ref. [41], is used as a measure for the fracture toughness. As can be seen in Fig. 7a, the K_{IC} value increases from 2.2 ± 0.4 MPa m^{1/2} for TiN to 3.7 ± 0.7 MPa m^{1/2} for TiCN, which is ascribed to the observed grain refinement. An even more pronounced enhancement of the fracture toughness can be observed with the addition of B. TiBN displays a K_{IC} value (5.0 ± 0.3 MPa m^{1/2}) comparable to the one of TiBCN (4.9 ± 0.4 MPa m^{1/2}), which again reflects the beneficial influence of grain refinement. Additionally, the higher fraction of grain boundaries, which represent amorphous and probably ductile fractions within the microstructure, are assumed to foster relaxation of the stress around the crack tip [42]. A further aspect, that has to be taken into account, is the difference in the preferred orientation of the B containing coatings in comparison to TiN and TiCN. The expressiveness of the texture coefficient in (110) orientation is significantly stronger for TiBN (2.9) and TiBCN (2.6) compared to TiN (1.3) and TiCN (1.9). In accordance to observations by Daniel *et al.*, TiN based

coatings featuring a higher amount of grains orientated in this direction seem to display a higher fracture toughness compared to their un- or differently textured counterparts [43].

A closer examination of the two-dimensional fracture cross-sections of the unnotched beams shown in Fig. 7b depicts qualitative differences in the cleavage of the four different coatings. The coarse fracture cross-section of TiN goes hand in hand with the observed big columnar grains of TiN (see Fig. 1a), which in turn determine the fracture strength and toughness of the coatings. The post mortem morphology of the fracture cross-section of a TiN bending beam suggests intergranular fracture as a result of a lower cohesive energy of the boundaries between the TiN columns [44]. The intermediate K_{IC} value of TiCN and the superior ones of TiBN and TiBCN go hand in hand with the decreasing grain size observable from the post mortem micrographs of the fracture cross-sections. The three-dimensional depiction of the fracture cross section presented in Fig. 7c allows a more detailed explanation of crack propagation within the tested bending beams. The quantitative roughness profiles of the four different depictions can be considered as a measure of the distance the crack had to travel through the coating prior to fracture. A more pronounced difference of the peak to valley height P_z indicates a stronger deflection of the crack, a more pronounced increase of the formed fracture surface and consequentially a retained crack propagation. The mean P_z (Fig. 7a) increases from 68 ± 3 nm and 79 ± 1 nm in TiN and TiCN, respectively, to 114 ± 5 nm in TiBN and 126 ± 16 nm in TiBCN, which is good agreement with the observed increment of the K_{IC} values and the decrement of the grain size.

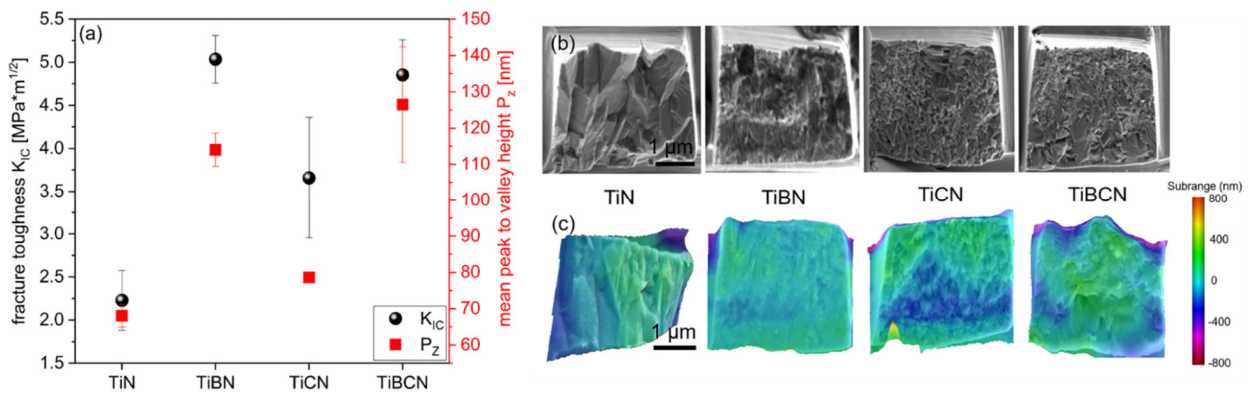


Fig. 7: (a) K_{IC} values and roughness of the investigated $\text{Ti}(B,C)\text{N}$ coatings. Post-mortem fracture cross-sections investigated by SEM of one representative tested bending beam each in (b) two and (c) three-dimensional representation. It should be noted, that the positions depicted in the three-dimensional representation are not identical to the ones of the two-dimensional ones.

4 Conclusions

TiN, TiBN, TiCN and TiBCN coatings were grown by thermally activated CVD and their microstructure, phase composition and mechanical properties were evaluated and compared to each other. All coatings investigated are dominated by fcc-TiN based phases. In addition, low fractions of amorphous TiB and h-TiB₂ were detected in TiBN, while the formation of these B rich phases seems to be inhibited for incorporation of B into the fcc-TiCN lattice in TiBCN. The addition of B resulted in a significant increase of the tensile residual stresses, which is related to the higher fraction of grain boundaries and the concomitant higher mismatch of the thermal expansion coefficients of coating and substrate. Addition of C to TiN entailed an increased hardness, Young's modulus, strength and fracture toughness through formation of a TiCN solid solution, coincident smaller globular grains and higher fraction of covalent bonding character. This beneficial effect on hardness and fracture toughness was even more pronounced for the B containing coatings, which is further reinforced by the more pronounced fracture resistant (110) crystal orientation. Concluding, the present study verifies, that the addition of B, C or a combination thereof results in an enhancement of the mechanical properties and identifies TiBCN as the most promising coating.

Acknowledgements

The authors want to thank Bernhard Sartory and Dr. Walter Costin (Materials Center Leoben) as well as Martina Dienstleder (FELMI-ZFE) for SEM/FIB work. Gerhard Hawranek (Montanuniversität Leoben) is acknowledged for performing the EDX/WDX measurements. Special thanks go to Dr. Ilse Letofsky-Papst (Graz University of Technology) for conducting the TEM measurement and for subsequent discussion of the results. We are grateful to Dr. Marco Deluca (Materials Center Leoben) for his assistance in Raman spectroscopy and valuable discussions on the topic. Thanks are also due to Dr. Jaako Julin (Helmholtz-Zentrum Dresden Rossendorf) for execution of the ERDA measurement. The financial support by the Austrian Federal Ministry for Digital and Economic Affairs and the National Foundation for Research, Technology and Development is gratefully acknowledged.

References

- [1] K. Bobzin, N. Bagcivan, P. Immich, S. Bolz, R. Cremer, T. Leyendecker, Mechanical properties and oxidation behaviour of (Al,Cr)N and (Al,Cr,Si)N coatings for cutting tools deposited by HPPMS, *Thin Solid Films* 517 (2008) 1251–1256.
- [2] W. Schintlmeister, W. Wallgram, J. Kanz, K. Gigl, Cutting tool materials coated by chemical vapour deposition, *Wear* 100 (1984) 153–169.
- [3] P.H. Mayrhofer, C. Mitterer, High-temperature properties of nanocomposite TiBN and TiBC coatings, *Surf. Coat. Technol.* 133–134 (2000) 131–137.
- [4] I. Endler, M. Höhn, J. Schmidt, S. Scholz, M. Herrmann, M. Knaut, Ternary and quaternary TiSiN and TiSiCN nanocomposite coatings obtained by Chemical Vapor Deposition, *Surf. Coat. Technol.* 215 (2013) 133–140.
- [5] J. Wagner, C. Mitterer, M. Penoy, C. Michotte, W. Wallgram, M. Kathrein, Structure and properties of CVD $\text{TiC}_x\text{N}_{1-x}$ coatings, *Proceedings of the 16th International Plansee Seminar 2005*, Vol. 2, p. 917–931.
- [6] J. Wagner, V. Edlmayr, M. Penoy, C. Michotte, C. Mitterer, M. Kathrein, Deposition of Ti–Al–N coatings by thermal CVD, *Int. J. Refract. Met. Hard Mater.* 26 (2008) 563–568.

- [7] D. -J. Cheng, W. -P. Sun, M. -H. Hon, The morphology and structure of chemically vapour-deposited Ti(C,N) coatings, *Thin Solid Films* 146 (1987) 45–53.
- [8] H. Holzschuh, Chemical-vapor deposition of wear resistant hard coatings in the Ti-B-C-N system: properties and metal-cutting tests, *Int. J. Refract. Met. Hard Mater.* 20 (2002) 143–149.
- [9] C. Czettel, C. Mitterer, M. Penoy, C. Michotte, M. Kathrein, C₂H₆ as precursor for low pressure chemical vapor deposition of TiCNB hard coatings, *Surf. Coat. Technol.* 215 (2013) 127–132.
- [10] C. Czettel, C. Mitterer, U. Mühle, D. Rafaja, S. Puchner, H. Hutter, M. Penoy, C. Michotte, M. Kathrein, CO addition in low-pressure chemical vapour deposition of medium-temperature TiC_xN_{1-x} based hard coatings, *Surf. Coat. Technol.* 206 (2011) 1691–1697.
- [11] N.P. Barradas, C. Jeynes, Advanced physics and algorithms in the IBA DataFurnace, *Nucl. Instrum. Methods Phys. Res B* 266 (2008) 1875–1879.
- [12] M.H. Müller, W.P. Chernock, P.A. Beck, Comments on Inverse Pole Figure Methods, *Trans. Metall. Soc. AIME.* 212 (1958) 39–40.
- [13] International Centre for Diffraction Data, PDF-2 Release, Card number 00-038-1420, 2018.
- [14] International Centre for Diffraction Data, PDF-2 Release, Card number 01-071-6059, 2018.
- [15] I.C. Noyan, J.B. Cohen, *Residual Stress: Measurement by Diffraction and Interpretation*, Springer-Verlag, New York, 1987.
- [16] W.C. Oliver, G.M. Pharr, An improved technique for determining hardness and elastic modulus using load and displacement sensing indentation experiments, *J. Mater. Res.* 7 (1992) 1564–1583.
- [17] K. Matoy, H. Schönherr, T. Detzel, T. Schöberl, R. Pippan, C. Motz, G. Dehm, A comparative micro-cantilever study of the mechanical behavior of silicon based passivation films, *Thin Solid Films* 518 (2009) 247–256.
- [18] H. Nowotny, F. Benesovsky, C. Brukl, O. Schob, Die Dreistoffe: Titan-Bor-Kohlenstoff und Titan-Bor-Stickstoff, *Monatsh. Chem.* 92 403–414.

- [19] H. Holzschuh, Moderate Temperature CVD Coatings in the Ti–B–N system, in: G. Kneringer, P. Rödhammer, H. Wildner (Eds.), in: 16th International Plansee Seminar, Plansee Holding AG, Reutte, 2005, p. HM59.
- [20] A. Paseuth, H. Fukui, S. Okuno, H. Kanaoka, Y. Okada, Microstructure, mechanical properties, and cutting performance of $\text{TiC}_x\text{N}_{1-x}$ coatings with various x values fabricated by moderate temperature chemical vapor deposition, *Surf. Coat. Technol.* 260 (2014) 139–147.
- [21] J. Wagner, D. Hochauer, C. Mitterer, M. Penoy, C. Michotte, W. Wallgram, M. Kathrein, The influence of boron content on the tribological performance of Ti–N–B coatings prepared by thermal CVD, *Surf. Coat. Technol.* 201 (2006) 4247–4252.
- [22] H. Holzschuh, Deposition of Ti–B–N (single and multilayer) and Zr–B–N coatings by chemical vapor deposition techniques on cutting tools, *Thin Solid Films* 469–470 (2004) 92–98.
- [23] C. Mitterer, P.H. Mayrhofer, M. Beschliesser, P. Losbichler, P. Warbichler, F. Hofer, P.N. Gibson, W. Gissler, H. Hruby, J. Musil, J. Vlček, Microstructure and properties of nanocomposite Ti–B–N and Ti–B–C coatings, *Surf. Coat. Technol.* 120–121 (1999) 405–411.
- [24] International Centre for Diffraction Data, PDF–2 Release, Card number 03–065–1073, 2018.
- [25] International Centre for Diffraction Data, PDF–2 Release, Card number 01–071–0298, 2018.
- [26] B.D. Cullity, *Elements of X–ray Diffraction*, Addison–Wesley, Reading Massachusetts, 1978.
- [27] C. Kainz, N. Schalk, M. Tkadletz, C. Mitterer, C. Czettl, Microstructure and mechanical properties of CVD TiN/TiBN multilayer coatings, *Surf. Coat. Technol.* (to be published)
- [28] I. Dreiling, D. Stiens, T. Chassé, Raman spectroscopy investigations of $\text{TiB}_x\text{C}_y\text{N}_z$ coatings deposited by low pressure chemical vapor deposition, *Surf. Coat. Technol.* 205 (2010) 1339–1344.
- [29] C. López–Cartes, D. Martínez–Martínez, J.C. Sánchez–López, A. Fernández, A. García–Luis, M. Brizuela, J.I. Oñate, Characterization of nanostructured Ti–B–(N) coatings produced by direct current magnetron sputtering, *Thin Solid Films* 515 (2007) 3590–3596.
- [30] A. Gupper, A. Fernández, C. Fernández–Ramos, F. Hofer, C. Mitterer, P. Warbichler, Characterization of Nanocomposite Coatings in the System Ti–B–N by Analytical Electron Microscopy and X–Ray Photoelectron Spectroscopy, *Monatsh. Chem.* 133 (2002) 837–848.

- [31] C. Mirguet, L. Calmels, Y. Kihn, Electron energy loss spectra near structural defects in TiN and TiC, *Micron* 37 (2006) 442–448.
- [32] E.O. Hall, The Deformation and Ageing of Mild Steel: III Discussion of Results, *Proc. Phys. Soc. Lond.* 64 (1951) 747–753.
- [33] N.J. Petch, The Cleavage Strength of Polycrystals, *J. Iron Steel Inst. London.* 173 (1953) 25–28.
- [34] N. Schalk, J. Keckes, C. Czettl, M. Burghammer, M. Penoy, C. Michotte, C. Mitterer, Investigation of the origin of compressive residual stress in CVD TiB₂ hard coatings using synchrotron X-ray nanodiffraction, *Surf. Coat. Technol.* 258 (2014) 121–126.
- [35] A. Leyland, A. Matthews, On the significance of the H/E ratio in wear control: a nanocomposite coating approach to optimised tribological behaviour, *Wear* 246 (2000) 1–11.
- [36] R. Daniel, D. Holec, M. Bartosik, J. Keckes, C. Mitterer, Size effect of thermal expansion and thermal/intrinsic stresses in nanostructured thin films: Experiment and model, *Acta Mater.* 59 (2011) 6631–6645.
- [37] H.O. Pierson, *Handbook of refractory carbides and nitrides: properties, characteristics, processing, and applications*, Noyes Publications, New York, 1996.
- [38] K. Wokulska, Thermal expansion of whiskers of Ti(C,N) solid solutions, *J. Alloys Compd.* 264 (1998) 223–227.
- [39] S. Massl, W. Thomma, J. Keckes, R. Pippan, Investigation of fracture properties of magnetron-sputtered TiN films by means of a FIB-based cantilever bending technique, *Acta Mater.* 57 (2009) 1768–1776.
- [40] I. El Azhari, J. Garcia, M. Zamanzade, F. Soldera, C. Pauly, L. Llanes, F. Mücklich, Investigations on micro-mechanical properties of polycrystalline Ti(C,N) and Zr(C,N) coatings, *Acta Mater.* 149 (2018) 364–376.
- [41] T.H. Courtney, *Mechanical Behavior of Materials*, McGraw–Hill, Boston, 2000.
- [42] Y.X. Wang, S. Zhang, Toward hard yet tough ceramic coatings, *Surf. Coat. Technol.* 258 (2014) 1–16.

-
- [43] R. Daniel, M. Meindlhumer, W. Baumegger, J. Zalesak, B. Sartory, M. Burghammer, C. Mitterer, J. Keckes, Grain boundary design of thin films, *Acta Mater.* 122 (2017) 130–137.
- [44] R. Daniel, M. Meindlhumer, W. Baumegger, J. Todt, J. Zalesak, T. Ziegelwanger, C. Mitterer, J. Keckes, Anisotropy of fracture toughness in nanostructured ceramics controlled by grain boundary design, *Mater. Des.* 161 (2019) 80–85.

Publication III

Thermo-physical properties of Ti(B,N) coatings grown by chemical vapor deposition

Christina Kainz, Nina Schalk, Michael Tkadletz, Christian Saringer,
Markus Winkler, Andreas Stark, Norbert Schell, Jaako Julin, Christoph Czettl

Surface & Coatings Technology 384 (2020) 125318



Thermo-physical properties of coatings in the Ti(B,N) system grown by chemical vapor deposition

Christina Kainz¹, Nina Schalk¹, Michael Tkadletz², Christian Saringer¹, Markus Winkler³, Andreas Stark⁴, Norbert Schell⁴, Jaakko Julin⁵, Christoph Czettel⁶

¹ *Christian Doppler Laboratory for Advanced Coated Cutting Tools at the Department of Materials Science, Montanuniversität Leoben, Franz-Josef-Straße 18, 8700 Leoben, Austria*

² *Department of Materials Science, Montanuniversität Leoben, Franz-Josef-Straße 18, 8700 Leoben, Austria*

³ *Department Thermal Energy Converters, Fraunhofer Institute for Physical Measurement Techniques IPM, Heidenhofstraße 8, 79110 Freiburg, Germany*

⁴ *Institute of Materials Research, Helmholtz-Zentrum Geesthacht, Max-Planck-Straße 1, 21502 Geesthacht, Germany*

⁵ *Institute of Ion Beam Physics and Materials Research, Helmholtz-Zentrum Dresden-Rossendorf, Bautzner Landstraße 400, 01328 Dresden, Germany*

⁶ *Ceratizit Austria GmbH, Metallwerk-Plansee-Straße 71, 6600 Reutte, Austria*

Keywords: Chemical vapor deposition, X-ray diffraction, Ti(B,N), thermal conductivity, strain

Abstract

Hard protective coatings are commonly subjected to temperatures exceeding 1000 °C, which has significant influence on their thermo-physical properties and the associated performance in application. Within the present work, temperature dependent physical properties of coatings within the Ti(B,N) system grown by chemical vapor deposition were correlated with their chemical composition. High-energy X-ray diffraction experiments in inert atmosphere proved that TiN, TiB₂ and ternary TiB_xN_y coatings with varying B contents are thermally stable up to 1000 °C. In-plane strains of TiN and TiB_xN_y coatings diminish during heating, whereas TiB₂ exhibits compressive strain enhancement up to the deposition temperature. Nanocrystalline TiB₂ exhibits more pronounced grain growth during annealing compared to coarse grained columnar TiN. Within the

investigated coatings, the mean thermal expansion coefficient decreases as the B content increases. The same trend was observed for the thermal conductivity, which correlates with the grain size of the coatings.

1. Introduction

Ternary TiB_xN_y coatings are commonly used for the protection of tools during metal cutting, as they are reported to show high hardness, combined with excellent wear resistance and oxidation stability [1,2]. The outstanding properties of TiB_xN_y coatings are mainly attributed to their nanocrystallinity and nanocomposite structure consisting of face centered cubic (fcc) TiN and hexagonal (h) TiB_2 . A vast number of publications is dedicated to TiB_xN_y coatings with different B contents prepared by physical vapor deposition [3–6]. However, it is also possible to deposit TiB_xN_y using chemical vapor deposition (CVD), where the B content is adjusted by the relative amount of the B precursor in the feed gas. Microstructure, mechanical properties, tribological behavior as well as cutting performance of CVD Ti(B,N) have been investigated in the past [7,8]. The hardness of coatings within the Ti(B,N) system is reported to increase with B addition, with the hardest being TiB_2 . However, a significant hardness drop was observed by Tkadletz *et al.* at a B content of ~45 at.%. This deterioration of the hardness was correlated with the transition from a fcc TiN dominating structure to sub-stoichiometric h $\text{TiB}_{2-x}\text{N}_y$ [7,9]. In CVD TiB_xN_y coatings with B contents <18 at.%, amorphous TiB was observed by Dreiling *et al.*, who reported that this compound improves the oxidation resistance within the Ti(B,N) system [10].

As protective coatings for cutting applications are subjected to temperatures, which may exceed 1000 °C, their thermal stability is of major importance [11]. In order to prevent the underlying tool from overheating, the coating should additionally exhibit good heat barrier properties. Ideally, the film should possess a low thermal conductivity out-of-plane to protect the substrate from overheating and a high one in-plane to dissipate the heat from the contact zone [12]. A further aspect that has to be considered is the mismatch in thermal expansion coefficient of coating and substrate, which should favorably be low. Otherwise cracks may arise during cooling or application, which

fosters oxidation and wear [13]. However, detailed information on the thermo-physical properties of CVD coatings in the Ti(B,N) system is missing in literature.

Thus, the goal of this work is to provide a summary on the thermo-physical properties of CVD coatings ranging from pure TiN over ternary TiB_xN_y coatings with different composition to pure TiB_2 . High energy X-ray diffraction (HE-XRD) at a synchrotron radiation source was used to monitor the phase stability, thermal expansion and lattice strain of the different phases in the coatings as a function of the temperature. Additionally, the thermal conductivity of the coatings was evaluated as a function of B content in order to assess their potential use as heat barriers.

2. Experimental methods

Coating depositions were carried out in a SuCoTec SCT600 TH industrial-scale thermal CVD plant using a gas mixture comprising TiCl_4 , H_2 , N_2 and Ar to synthesize TiN. BCl_3 was supplied additionally in the depositions of the B containing coatings and N_2 was omitted to obtain pure TiB_2 . Further details on the deposition conditions can be found in ref. [14]. The resulting coating thickness ranged from 4.0 to 7.1 μm and the growth rate was between 0.76 and 1.64 $\mu\text{m}/\text{h}$. Cemented carbide cutting inserts with 92 wt.% WC, 6 wt.% Co and 2 wt.% mixed carbides in SNUN geometry (ISO 1832) served as substrate. In order to prevent B diffusion into the substrate, a ~ 0.2 μm thick TiN base layer was applied underneath the B containing coatings. TiN and TiB_2 were additionally deposited onto Fe foil. In order to obtain TiN and TiB_2 powders, the Fe substrates were then dissolved in an aqueous solution of HNO_3 (20 vol. %) at 70 °C for 1 h.

The chemical composition of the B containing coatings was determined by means of elastic recoil detection analysis (ERDA) using a 43 MeV $^{35}\text{Cl}^{7+}$ ion beam and a Bragg ionization chamber in 30 ° angle with respect to the beam. Energy dispersive X ray spectroscopy (EDX) was used in order to determine the elemental composition of TiN [15]. The EDX measurement was carried out with an Oxford Instruments INCA spectrometer, equipped with an INCA extension mounted on a Zeiss EVO50 scanning electron microscope (SEM).

For a first assessment of the microstructure of the as-deposited and annealed Ti(B,N) coatings, a Bruker AXS D8 Advance diffractometer in grazing incidence geometry (incidence

angle 2°) with Cu K_α radiation was used. TiN and TiB₂ coatings were annealed in an HTM Reetz vacuum furnace at a base pressure of 5×10^{-6} mbar and 1000 °C for 15 and 120 min. The morphology of as-deposited and annealed TiN and TiB₂ coatings was compared using a field emission gun SEM of type Zeiss Auriga.

HE XRD investigations were carried out at the P07 High Energy Materials Science Beamline of the Helmholtz Zentrum Geesthacht at DESY. For that purpose, samples with a size of $4 \times 4 \times 8$ mm³ were prepared by mechanical cutting. The experiments were conducted using a monochromatic synchrotron beam with an energy of 87.1 keV and a cross section of 400×100 μm^2 . Fig. 1 shows a schematic view of the test set up used for the determination of the temperature dependent phase evolution, lattice expansion and strain of the coatings. The chosen maximum temperature for all six samples was 1000 °C, as this is a realistic temperature arising during metal cutting. A coil heated the substrate inductively and the temperature was monitored with a thermocouple mounted to the substrate material. In order to prevent oxidation, heating was performed in Ar atmosphere. Debye-Scherrer rings were collected in transmission geometry on a Perkin Elmer XRD 1621 flat panel detector. The geometric relations between sample and detector were calibrated with a LaB₆ powder standard. The one dimensional data obtained through azimuthal integration over the entire angular range were used to compile temperature resolved phase plots of the coatings. Evaluation of the 2D diffraction data was conducted using the software DAWN 2 [16]. In addition to phase identification, the distortion of the obtained Debye Scherrer rings allowed the determination of the temperature dependent in-plane strain. The Debye Scherrer rings of the (200) reflection in case of the TiN and (101) in case of the TiB₂ phase were divided into cake segments of 10° and azimuthally integrated. Due to the low intensity of the reflections in the lower part of the Debye-Scherrer rings, resulting from the absorption of the cemented carbide substrate (compare Fig. 1), only the upper part was used for the evaluation. The peak positions were fitted applying a Pseudo-Voigt function. A custom made Python script allowed processing of the data following the $\sin^2\psi$ method to obtain the lattice strain.

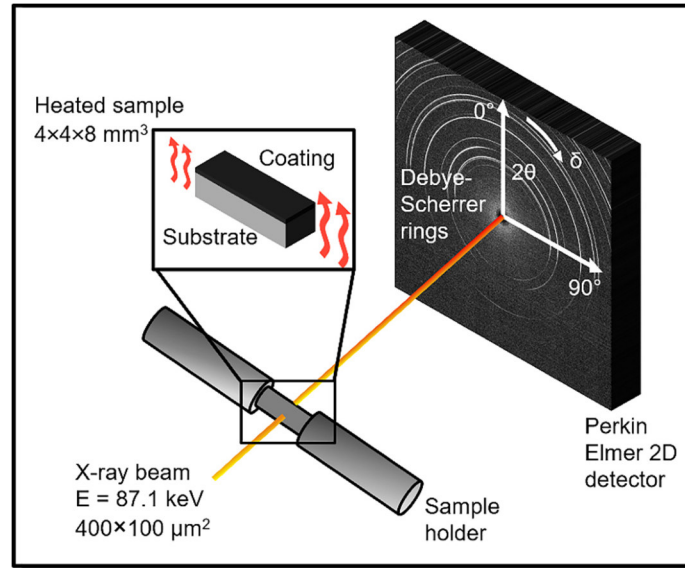


Fig. 1: Schematic of the measurement set-up used to determine the temperature dependent thermal expansion and in-plane strains of the $Ti(B,N)$ coatings. The respective sample was irradiated by a monochromatic X-ray beam perpendicular to the cross section of the sample. While the sample was heated, Debye Scherrer rings were collected in transmission geometry on a Perkin Elmer 2D detector located behind the sample.

Analysis of the thermal expansion of the coatings in the temperature range 25-860 °C was performed according to the method reported by James *et al.* [17]. 860 °C was chosen as the maximum temperature for this evaluation, as this was the lowest applied deposition temperature. The (200) reflection was used in case of fcc-TiN and the (101) reflection in case of h-TiB₂. h-TiB₂ exhibits a different thermal expansion in a and c direction [18]. Eq. (1) enables to calculate an averaged mean thermal expansion coefficient $\alpha_{a,c}$ by

$$\alpha_{a,c} = \frac{2\alpha_a + \alpha_c}{3} \quad [18] \quad (1)$$

For the ternary TiB_xN_y coatings, the expansion of both phases, fcc-TiN and h-TiB₂, was evaluated and averaged as a function of the actual B content to obtain α_m . The evaluation was conducted at the strain free azimuthal angles calculated by

$$\cos\delta_0 \cos\theta_0 = \sqrt{\frac{1-\nu}{1+\nu}}, \quad (2)$$

with ν representing the Poisson's ratio of the respective material, δ_0 the strain-free azimuthal angle and θ_0 the conducted Bragg angle [19,20]. A segment of $\pm 5^\circ$ from the respective strain-free azimuthal angle was evaluated in order to obtain a reasonable data volume for the subsequent fit. Poisson's ratios of 0.23 and 0.11 were used for the calculation of the fcc-TiN and h-TiB₂ phases, respectively [18,21]. The obtained data were validated by comparison with the thermal expansion determined for powdered TiN and TiB₂ of the corresponding deposition runs. Therefore, diffractograms of these powders were recorded at the high resolution powder diffraction beamline ID22 at the European Synchrotron Radiation Facility. The powders were encapsulated within a quartz capillary in Ar atmosphere and heated to 1000 °C. Pt powder served as standard for the temperature calibration. Detailed information on the measurement set up for the powdered samples are given in ref. [22]. The lattice parameters of both, the powdered and solid coatings, were fitted applying a polynomial of second order to obtain α_{av} . In case of the solid coatings, α_{av} was determined from an average of the data gained at the two respective strain-free angles.

The thermal conductivity of the coatings in as-deposited state was determined by time domain thermoreflectance (TDTR). For TiN and TiB₂, the annealed samples were also measured. TDTR measurements were conducted in out-of-plane direction and realized by a pulsed laser pump-probe system, as described in ref. [23]. The necessary laser pulses were generated by the Ti:Sapphire laser system Mai Tai from Spectra-Physics with a pulse width of 500 fs, a pulse repetition rate of 80 MHz, a wavelength of 785 nm and an average laser power (i.e. added average power of probe and pump beam) of 30 mW. The pump beam was modulated with a frequency of 11.1 MHz, resulting in an information depth between 0.25 and 0.64 μm [23]. The time delay between pump and probe beam was in the range of 0 to 3600 ps. As a transducer layer, 70 nm of pure Al were deposited on the samples prior to the measurement. Directly before the measurements on the samples, the measurement system was validated with two reference samples, namely a pure Si wafer and an oxidized one.

3. Results and discussion

The chemical composition of the coatings as determined by ERDA is shown in Fig. 2a. For the nomenclature, the B and N content in the coatings was normalized to the Ti content. All coatings are located on the quasi-binary tie line of TiN-TiB₂, except TiB_{1.2}N_{0.56}, which is slightly shifted beside this line [24]. XRD investigations (Fig. 2b) allowed the assessment of the microstructure of the coatings at room temperature (RT). With increasing amount of B in the coating, both, the intensity of the h-TiB₂ (101) reflection and the peak broadening gradually become more pronounced. The higher TiB₂ fraction explains the decrement in the Ti content with increasing B in the coating, as less Ti is needed for the formation of TiB₂ in comparison to TiN. The grain refinement is reflected in the evolution of the full width at half maxima (FWHM) shown in Fig. 2c. An increment of the FWHM correlates with the smaller size of coherently diffracting domains [25]. In case of TiB₂, the (101) reflection was applied for the evaluation of the FWHM, whereas for the TiN and TiB_xN_y coatings the (200) reflection of fcc-TiN was used. The pronounced peak broadening of TiB_{1.2}N_{0.56} had already been observed by other authors and is suggested to result from the distorted structure and the concomitant high micro strains of this coating [9]. From the lab scale X-ray diffractograms it may be assumed that only one peak is present at $2\theta \sim 42^\circ$, which seems to shift towards larger diffraction angles with increasing B content. However, the observed peak is comprised of the (101) h-peak of TiB₂ and the (200) fcc peak of TiN as can be seen from the results of the HE-XRD in Figure 3. Thus, for the evaluation of the FWHM of the TiB_xN_y coatings, the peak was deconvoluted into two peaks, which were fitted using the Pseudo-Voigt function.

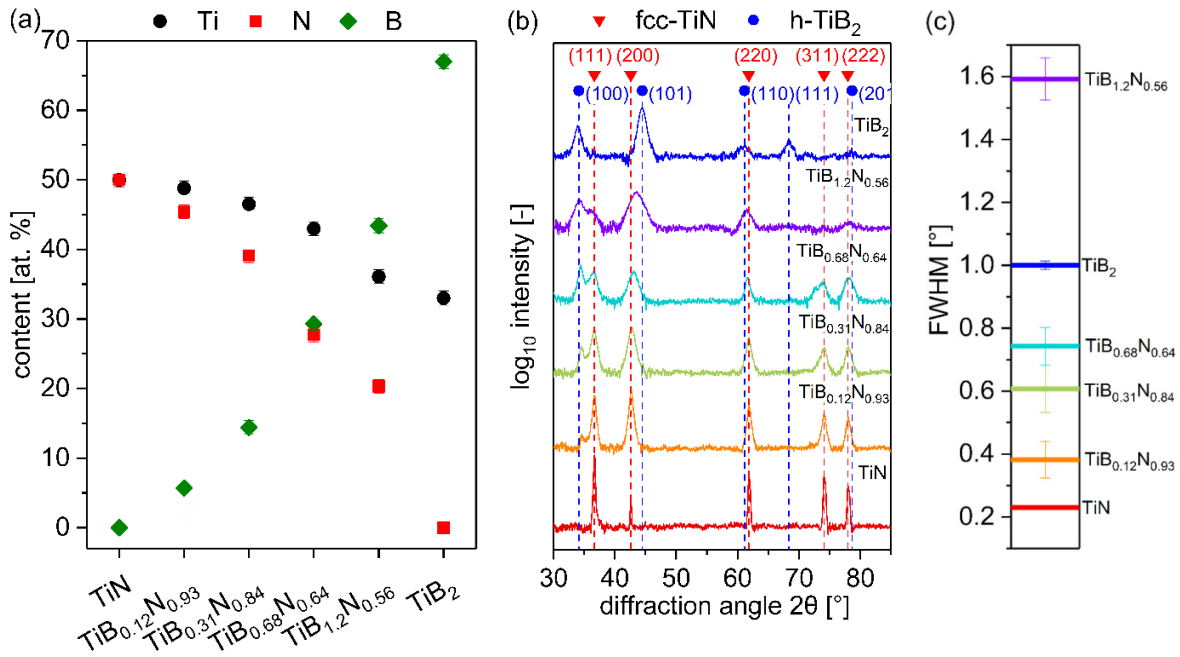


Fig. 2: (a) Chemical composition, (b) X-ray diffractograms, measured in grazing incidence geometry and (c) FWHM of the Ti(B,N) coatings.

The temperature dependent phase plots in Fig. 3 show a d-spacing range including the (200) fcc-TiN and (101) h-TiB₂ reflections. Standard d-spacings of these two phases at RT were taken from ICDD file # 00-038-1420 and # 01-071-0298 for fcc-TiN and h-TiB₂, respectively [26,27]. In agreement with the X-ray diffractograms given in Fig. 2, the phase plot of the TiN coating shows only fcc-TiN [26]. With increasing amount of B, a second phase with a d-spacing of 2.06 Å emerges, which is assigned to h-TiB₂. Other minor intensities stem from the Co binder in the substrate. The (200) peak of fcc TiN and the (101) peak of h-TiB₂ overlap in the lab-scale XRD (Fig. 2b), however, differentiation of these two reflections is possible by means of HE XRD. Up to TiB_{0.68}N_{0.64}, the signal of fcc-TiN is more pronounced than the one of h-TiB₂, which changes in case of TiB_{1.2}N_{0.56} in favor of h-TiB₂. None of the diffractograms show formation of additional phases at elevated temperatures. Temperature induced reactions between coating and substrate, as for instance the formation of brittle W-Co-B phases, can thus be excluded up to 1000 °C in protective atmosphere [28]. The ratio between fcc-TiN and h-TiB₂ in the ternary TiB_xN_y coatings seems to be, to a large extent, independent of the temperature. The position of the (200) peak of TiN is in reasonable good agreement with the one reported for fcc-TiN [26]. However, a slight peak shift is observable in case of the (101) reflection of

h-TiB₂, which is more pronounced at lower B contents. This observation suggests the formation of a sub stoichiometric h-TiB_{2-x}N_y structure, which converges to stoichiometric h-TiB₂ with increasing B content. At higher B contents there is less N incorporated in this h-phase, which is why the lattice expands less and thus the lattice parameter is smaller.

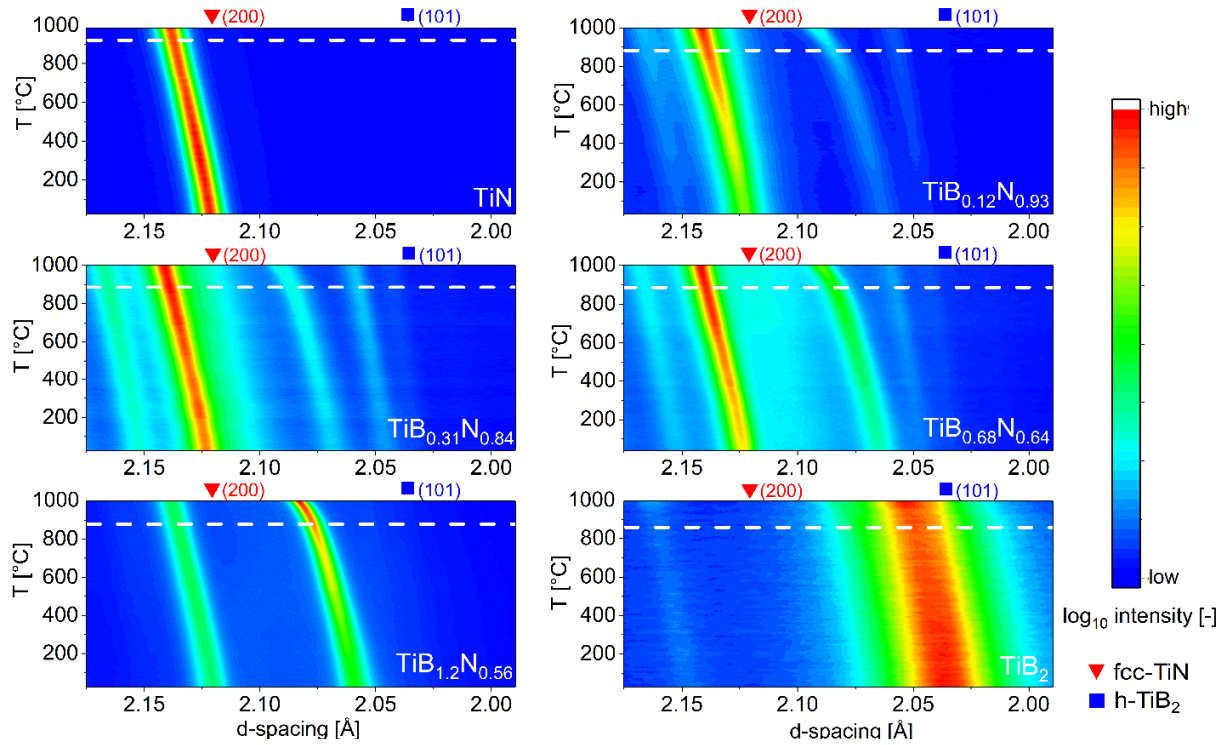


Fig. 3: Phase evolution of the $Ti(B,N)$ coatings as a function of the temperature. Literature d spacings of the (200) reflection of fcc-TiN and the (101) reflection of h-TiB₂ are indicated by the red rectangle and blue square, respectively. The white dotted lines mark the deposition temperatures of the respective coatings.

The temperature resolved HE-X-ray diffractograms allow the determination of the thermal expansion of the coatings. Fig. 4 shows the mean coefficient of thermal expansion α_m in the temperature range 25–860 °C of the investigated coatings. Additionally, the estimated phase fraction of h-TiB₂ used for the calculation of α_m is plotted. This fraction was calculated according to the B content in the coating available for the formation of h-TiB₂, neglecting a possible sub stoichiometric composition for this estimation. Further, it was assumed that no B is incorporated into the fcc-TiN lattice, which is in agreement with Nowotny *et al.* [24]. As can be seen in Fig. 3, the h-TiB₂ phase

shows a deviation from non-linear behavior when the deposition temperature (T_{dep}) is exceeded. In order to ensure that no effects other than the expansion of the lattice falsify the evaluation, the lowest applied T_{dep} was chosen as maximum temperature. The mean thermal expansion coefficient of the investigated coatings gradually decreases as a function of increasing B content. Thus, a lower mismatch of α_m between coating and the used cemented carbide substrate ($5.5 \times 10^{-6} \text{ K}^{-1}$) is achieved when applying protective coatings with high B contents [29]. Consequently, B rich coatings should be chosen in favor over TiN and B lean coatings in regard of the thermal expansion coefficient to possibly retard crack formation [13]. However, it should be noted that the deposition of B containing coatings onto cemented carbide always requires a base layer in order to prevent B diffusion into the substrate. Otherwise, the resulting formation of brittle W-Co-B phases causes decarburization of the substrate, which deteriorates the cutting performance [28]. Thus, commonly a TiN base layer is applied underneath TiB_2 . The adhesion problem between these two layers, which arises from the difference in crystal structure, stresses and grain size, can be overcome by using an additional graded TiB_xN_y transition layer. The ternary TiB_xN_y coatings investigated within this study were shown to be suitable for cutting applications as a graded interlayer stack between binary TiN and TiB_2 [9,14].

Commonly, the thermal expansion coefficient is determined by XRD using powdered samples [30,31]. Thus, the herein obtained values for α_{av} for solid coatings were validated through comparison with powders of TiN and TiB_2 coatings of the respective deposition runs. An excellent agreement between the TiN powder ($8.94 \times 10^{-6} \text{ K}^{-1}$) and the solid coating ($8.94 \times 10^{-6} \text{ K}^{-1}$) was found using the Poisson's ratio reported by Almer *et al.* [21]. This was also true in case of TiB_2 , when using the Poisson's ratio reported by Munro [18]. The powder exhibited a value of $\alpha_m = 7.40 \times 10^{-6} \text{ K}^{-1}$ and the solid coating $\alpha_m = 7.56 \times 10^{-6} \text{ K}^{-1}$, verifying the feasibility of determining the thermal expansion coefficient on intact coatings.

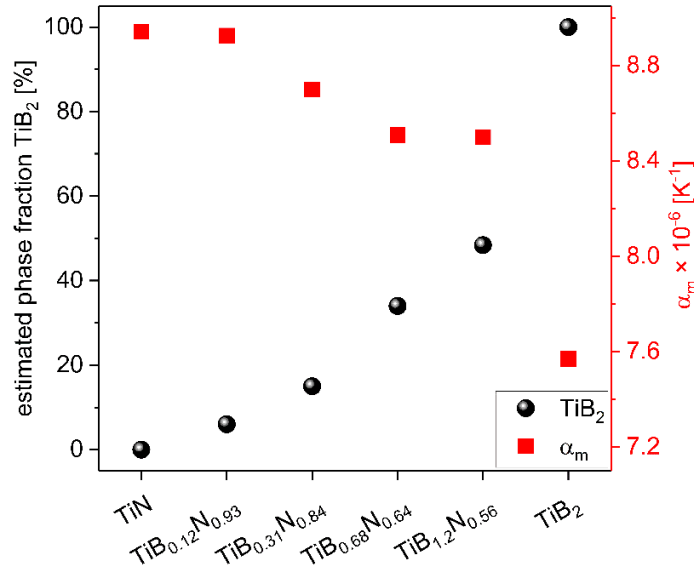


Fig. 4: Estimated phase fraction of h- TiB_2 based on the available B content and mean coefficient of thermal expansion in the temperature range 25-860 °C of the Ti(B,N) coatings.

The temperature dependent evolution of the in-plane strains of the investigated coatings is shown in Fig. 5. It should be pointed out that the calculation of the strain is based solely on one orientation for each phase, being (200) in fcc-TiN and (101) in h- TiB_2 . In case of $\text{TiB}_{0.12}\text{N}_{0.93}$ and $\text{TiB}_{0.31}\text{N}_{0.84}$, only the strain in the fcc-phase could be evaluated, due to the minor fractions and thus low signal intensity of h- TiB_2 within these coatings. In the ternary coatings with higher fractions of the h- TiB_2 phase, both the strain within the fcc- and the h-phase was investigated. Nevertheless, a reasonable evaluation could be achieved. The results in Fig. 5 demonstrate how different phases influence each other during thermal treatment. At RT, the strain in the fcc-phase within TiN and the ternary coatings (Fig. 5a) is tensile due to the higher thermal expansion coefficient of the coating in comparison to the substrate. With increasing fraction of h- TiB_2 in the coating, the tensile strain in the fcc-TiN phase at RT increases to its highest value in $\text{TiB}_{1.2}\text{N}_{0.56}$. It is assumed that the reason for that are coherency strains, which arise as a result of the coherent epitaxial relationship between fcc-TiN and h- TiB_2 [32]. The strain of the fcc phase within TiN and the ternary coatings changes from tensile at RT to unstrained or slightly compressive at the respective T_{dep} . This change becomes more pronounced with increasing fraction of the h- TiB_2 phase, as evidenced in Fig. 5b and c. Regarding the h-phase, a higher fraction of fcc-TiN in the coating is suggested to provoke both,

higher compressive strains at RT and stronger change of the strain during heating (Fig. 5b and c). With increasing temperature, the strain of the h-phase in the ternary coatings moves towards a tensile strained state, which is in contrast to binary TiB_2 , where the strain becomes more compressive up to T_{dep} . Afterwards, the coating strain of TiB_2 shows a pronounced relaxation up to the maximum test temperature of 1000 °C. This behavior was not observed for the h-phase in the ternary coatings. It may thus be suggested that the presence of the second phase impedes the relaxation. The reason for the compressive strains in CVD TiB_2 coatings is up to now not entirely understood. However, the higher Laplace pressure due to the high surface energy and nanocrystalline grain size of TiB_2 was suggested by Schalk *et al.* as a possible source for the compressive strains [33,34]. During cooling, the tensile strain of the fcc-phase increases again for TiN and the ternary coatings. TiN shows a deviation from the linear strain evolution in the cooling curve. The most plausible reason for this is formation of thermal cracks, as was reported by Bartosik *et al.* for CVD TiN coatings [35]. The presence of such cracks in the here investigated TiN was verified by SEM, as is shown below in Fig. 7. While a slight kink may also be suggested from the cooling curve of $\text{TiB}_{0.12}\text{N}_{0.93}$, the tensile strain of the fcc-phase within the other coatings do not display this feature. Otherwise, the TiB_xN_y coatings show only minor deviations of the strain during heating and cooling, which is true both for the fcc- and the h-phase. Therefore, the extent of relaxation of strains during heating is low. Contrarily, a major difference between the heating and cooling curve in pure TiB_2 is evident. The strain within this coating does not change noteworthy during cooling and the coating remains in a slightly tensile strained state. A further decisive aspect that has to be considered in the discussion of the strains is the texture of the coatings. The intensity of the peaks was largely invariant on the azimuth in case of the binary coatings and the (220) fcc-TiN reflection of the ternary ones. This was not the case for the (101) h- TiB_2 reflection in the TiB_xN_y coatings, which indicates the presence of a texture. However, the $\sin^2\psi$ plots were linear and thus the effect of the texture on the strains is suggested to be negligible.

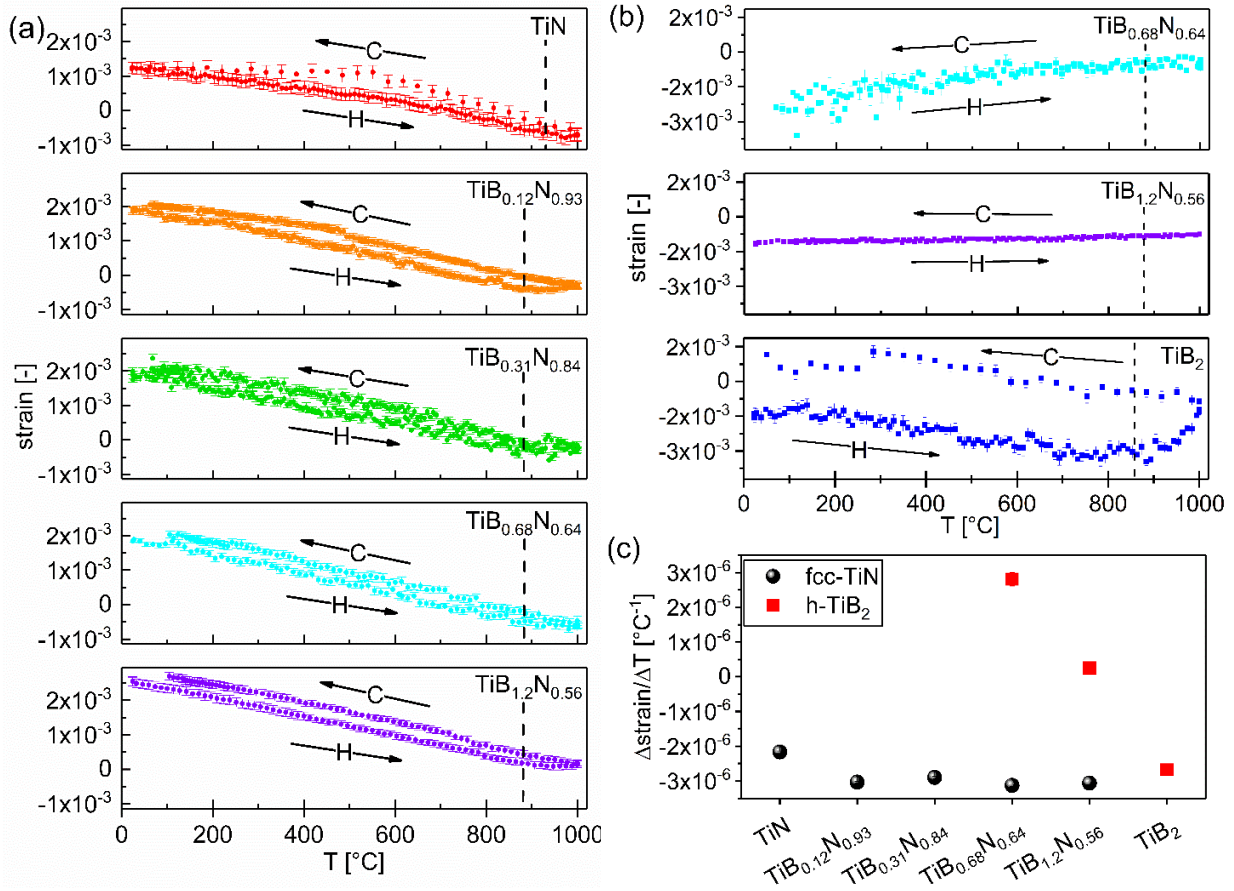


Fig. 5: Evolution of the in-plane strain as a function of the temperature within the $Ti(B,N)$ coatings. The (200) peak was evaluated in case of fcc-TiN phase (a), whereas for the h-TiB₂ phase the (101) reflection was used (b). Arrows with H depict the direction of heating, arrows with C the direction of cooling. The vertical dotted lines mark the respective deposition temperature. (c) $\Delta\text{strain}/\Delta T$ in the fcc and in the h-phase between RT and T_{dep} as a function of the B content.

Being a measure of the distribution of heat within a tool, the thermal conductivity is a decisive parameter when evaluating the suitability of a material for a given application [30]. Fig. 6 shows the estimated specific heat capacity c_p and the measured thermal conductivity λ of the investigated coatings. c_p of the TiB_xN_y coatings was averaged from the values of TiN and TiB₂ in dependence of the estimated fraction of the h-TiB₂ phase applying the rule of mixture [18,36]. Provided that the TiB₂ content in the sample is directly related to the B content, the specific heat capacity decreases when going from B poor to B rich samples. The thermal conductivity decreases inversely proportional with the B content. While the highest value was found for TiN (45 W/mK),

TiB_{1.2}N_{0.56} features the lowermost one with 7 W/mK. This behavior can be ascribed to the grain refinement through B addition. With decreasing grain size and concomitant higher defect density, the phonon scattering increases and consequentially the thermal conductivity declines. The fact that TiB₂ exhibits a higher thermal conductivity (14 W/mK) in comparison to TiB_{1.2}N_{0.56} is assigned to the alloy scattering in the ternary coatings. The thermal conductivity of TiB₂ in the present study is low in comparison to data reported in literature (96 W/mK). This discrepancy is most likely due to the difference in microstructure between the nanocrystalline TiB₂ in our study and the material in the reference with a grain size of 12 μm [18]. A similar situation applies to TiN. The columnar grains of TiN in our study partly extend over the whole coating thickness of ~6 μm. In comparison, Samani *et al.* report a thermal conductivity of 11 W/mK in a TiN coating with a thickness of 1.2 μm and thus smaller grain size in growth direction [37]. The larger grain size and thus less pronounced phonon scattering of TiN in our work explains the discrepancy. As the h-TiB₂ phase in TiB_{0.68}N_{0.64} and TiB_{1.2}N_{0.56} exhibited a texture, a possible anisotropy of the thermal conductivity cannot be fully excluded. However, as the TiB₂ is reported to be nanocrystalline and distributed between the larger TiN grains, the effect is assumed to be negligible [33,38]. It should be emphasized at this point that the thermal conductivity was determined in out-of-plane direction, while the strains and thermal expansion refer to the in-plane direction. Furthermore, the information depth was noteworthy lower in the TDTR measurements (between 0.25 and 0.64 μm) in comparison to the synchrotron experiments, where the whole coating thickness was probed. Thus, possible gradients in stress, grain size and texture over the coating thickness may affect the results of the two measurements in a different extent. The impact of annealing on the coatings' microstructure is reflected in the thermal conductivity. There is no major change of this parameter when annealing TiN for 15 or 120 min at 1000 °C. Contrarily, the annealing of TiB₂ results in an increase from 14 W/mK in the as-deposited state to 26 W/mK and 37 W/mK in the coating annealed for 15 and 120 min, respectively. These observations suggest that TiB₂ undergoes more pronounced grain growth and defect annihilation during annealing at 1000 °C compared to TiN.

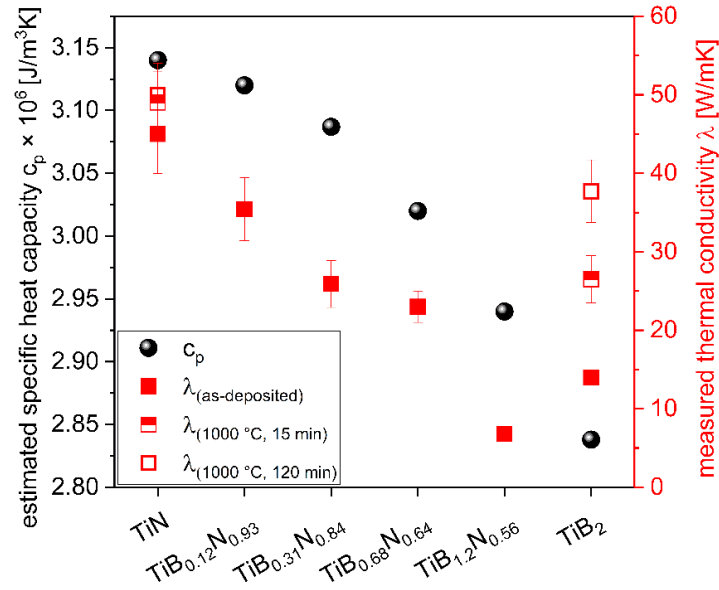


Fig. 6: Estimated specific heat capacity and measured thermal conductivity of the Ti(B,N) coatings. Partly filled symbols represent measurements of coatings annealed at 1000 °C for 15 min, open symbols indicate annealing for 2 hours at the same temperature.

The cross-section morphologies of TiN and TiB₂ in as-deposited and annealed state (Fig. 7) verify this presumption. While no major difference between the micrographs of as deposited and annealed TiN is visible, grain growth is unambiguously observable in the heat treated TiB₂ coatings. After 15 min of annealing, only a few larger grains are visible, however, grain growth becomes clearly evident after heat treatment for 120 min. The behavior of the FWHM follows the same trend: the peak broadening of TiN, determined on the (200) reflection, was invariant on the heat treatment. Contrarily, the FWHM of the (101) reflection of TiB₂ decreases from 1.00° in the as-deposited state to 0.73° and 0.35° after annealing for 15 and 120 min, respectively. Considering both, the cross-section morphology and FWHM, it may be concluded that the reduced FWHM in the TiB₂ coating annealed for 15 minutes is mainly related to defect annihilation. The reason for the pronounced grain growth in TiB₂ is due to its high number of grain boundaries. As they constitute defects in a perfect lattice, reduction of the grain boundary area results in a decrement of the Gibbs free energy [39]. The cross sectional crack depicted in the micrograph of as-deposited TiN (Fig. 7a) is representative for the morphology of this coating. These cracks arise in TiN during cooling after

the deposition, as was discussed above (compare also Fig. 5a). Cracks were not observable in case of TiB_2 , which is suggested to stem from the nanocrystalline grains and concomitant high strength according to the Hall-Petch effect [40,41]. Furthermore, the higher K_{IC} value of TiB_2 ($6.2 \text{ MPa}/\text{m}^{1/2}$) in comparison to TiN ($1.2 - 3 \text{ MPa}/\text{m}^{1/2}$) and thus better resistance to crack propagation explains the lower abundance of cracks in TiB_2 [18,42,43].

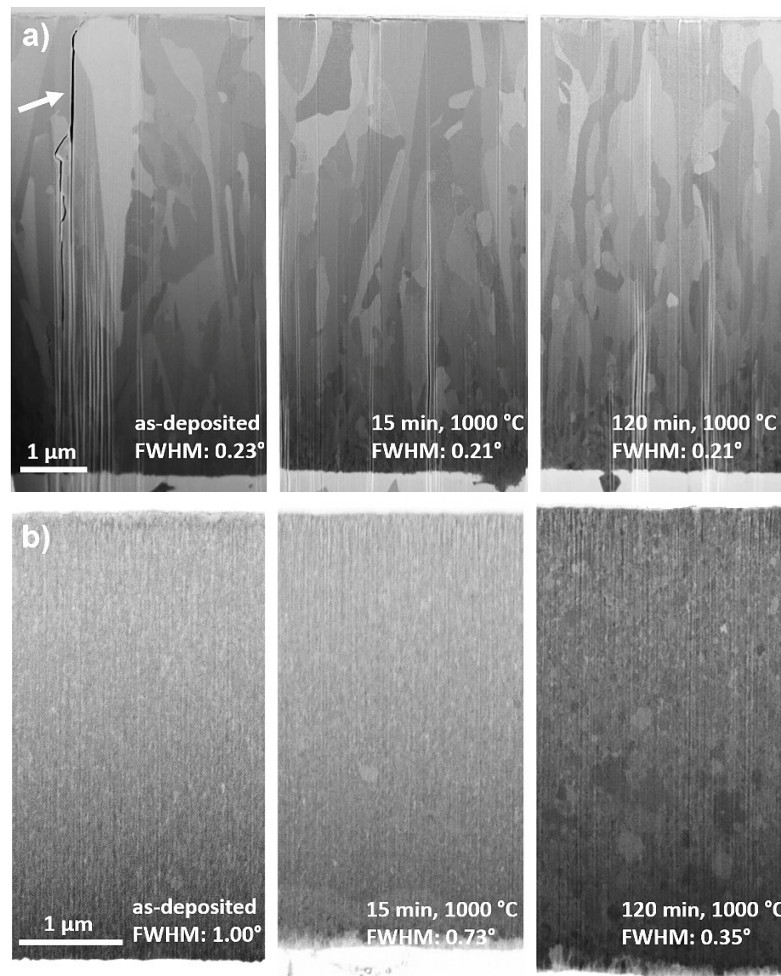


Fig. 7: Cross-sectional secondary electron micrographs of a) TiN and b) TiB_2 in as-deposited state (left) and annealed at 1000 °C for 15 (middle) and 120 min (right) with the corresponding FWHM. A cross-sectional crack is marked by a white arrow in the as-deposited TiN (a).

In order to summarize the findings gathered within this work, Table 1 gives the numerical values of the coating thickness, thermal expansion coefficient, specific heat capacity and thermal conductivity of the investigated coatings as a reference.

Table 1: Summary of thermo-physical properties of all investigated Ti(B,N) coatings.

	Coating thickness [μm]	α [10^{-6} K^{-1}] ¹	λ [W/mK] ²	c_p [$10^6 \text{ J/m}^3\text{K}$] ³
TiN	7.1	8.94	45	3.14
TiB_{0.12}N_{0.93}	5.0	8.93	35	3.12
TiB_{0.31}N_{0.84}	5.4	8.70	26	3.09
TiB_{0.68}N_{0.64}	5.9	8.51	23	3.02
TiB_{1.2}N_{0.56}	7.4	8.50	7	2.94
TiB₂	4.1	7.57	14	2.84

¹ mean coefficient of thermal expansion (25-860 °C), ² thermal conductivity, ³specific heat capacity

4. Conclusions

TiN, TiB₂ and TiB_xN_y coatings with varying B contents have been grown by thermally activated chemical vapor deposition and their thermo-physical properties have been studied. HE-XRD experiments showed that annealing the coatings in protective atmosphere between 25 and 1000 °C does not alter the phase composition. The thermal expansion, directly determined from the coatings on the substrate, declines as the B content increases. TiB₂ exhibits an increment of the in-plane compressive lattice strain during heating up to T_{dep} . The relaxation of the in-plane tensile strains during cooling in TiN is suggested to result from the formation of thermal cracks. In the ternary coatings, both the tensile strains in the fcc- and the compressive strains in the h-phase diminish as the thermal load increases to the deposition temperature. The thermal conductivity in the coatings decreases with increasing B content, which is ascribed to increased phonon scattering as a result of smaller grain size and higher defect density. The results gained within this work give an overview of selected thermo-physical properties of CVD coatings in Ti(B,N) system and thus allow for a better understanding of these application relevant materials.

Acknowledgements

The authors thank Bernhard Sartory (Materials Center Leoben) for FIB-SEM work. The financial support by the Austrian Federal Ministry for Digital and Economic Affairs and the National Foundation for Research, Technology and Development is gratefully acknowledged. The authors gratefully acknowledge the financial support under the scope of the COMET program within the K2 Center “Integrated Computational Material, Process and Product Engineering (IC MPPE)” (Project No 859480). This program is supported by the Austrian Federal Ministries for Transport, Innovation and Technology (BMVIT) and for Digital and Economic Affairs (BMDW), represented by the Austrian research funding association (FFG), and the federal states of Styria, Upper Austria and Tyrol.

References

- [1] P.H. Mayrhofer, C. Mitterer, High-temperature properties of nanocomposite TiBN and TiBC coatings, *Surf. Coat. Technol.* 133–134 (2000) 131–137.
- [2] P.H. Mayrhofer, C. Mitterer, Thermal Stability of Nanostructured TiN–TiB₂ Thin Films, *Mater. Res. Soc. Symp. Proc.* 845 (2005).
- [3] C. Mitterer, P.H. Mayrhofer, M. Beschliesser, P. Losbichler, P. Warbichler, F. Hofer, P.N. Gibson, W. Gissler, H. Hraby, J. Musil, J. Vlček, Microstructure and properties of nanocomposite Ti–B–N and Ti–B–C coatings, *Surf. Coat. Technol.* 120–121 (1999) 405–411.
- [4] L. Chaleix, J. Machet, Study of the composition and of the mechanical properties of TiBN films obtained by D.C. magnetron sputtering, *Surf. Coat. Technol.* 91 (1997) 74–82.
- [5] C.X. Tian, Z.S. Wang, C.W. Zou, X.S. Tang, X. Xie, S.Q. Li, F. Liang, Z.J. Li, Y.F. Liu, F.H. Su, Ternary and quaternary TiBN and TiBCN nanocomposite coatings deposited by arc ion plating, *Surf. Coat. Technol.* 359 (2019) 445–450.
- [6] C. Mitterer, M. Rauter, P. Rödhammer, Sputter deposition of ultrahard coatings within the system Ti–B–C–N, *Surf. Coat. Technol.* 41 (1990) 351–363.

- [7] J. Wagner, D. Hochauer, C. Mitterer, M. Penoy, C. Michotte, W. Wallgram, M. Kathrein, The influence of boron content on the tribological performance of Ti–N–B coatings prepared by thermal CVD, *Surf. Coat. Technol.* 201 (2006) 4247–4252.
- [8] H. Holzschuh, Deposition of Ti–B–N (single and multilayer) and Zr–B–N coatings by chemical vapor deposition techniques on cutting tools, *Thin Solid Films* 469–470 (2004) 92–98.
- [9] M. Tkadletz, N. Schalk, C. Mitterer, J. Keckes, M. Pohler, C. Czettl, Cross-sectional characterization techniques as the basis for knowledge-based design of graded CVD TiN–TiB₂ coatings, *Int. J. Refract. Met. Hard Mater.* 71 (2018) 280–284.
- [10] I. Dreiling, C. Raisch, J. Glaser, D. Stiens, T. Chassé, Characterization and oxidation behavior of MTCVD Ti–B–N coatings, *Surf. Coat. Technol.* 206 (2011) 479–486.
- [11] I. Krajinović, W. Daves, M. Tkadletz, T. Tepperneegg, T. Klünsner, N. Schalk, C. Mitterer, C. Tritremmel, W. Ecker, C. Czettl, Finite element study of the influence of hard coatings on hard metal tool loading during milling, *Surf. Coat. Technol.* 304 (2016) 134–141.
- [12] P.H.M. Böttger, L. Braginsky, V. Shklover, E. Lewin, J. Patscheider, D.G. Cahill, M. Sobiech, Hard wear-resistant coatings with anisotropic thermal conductivity for high thermal load applications, *J. Appl. Phys.* 116 (2014) 13507.
- [13] M. Gassner, N. Schalk, M. Tkadletz, C. Czettl, C. Mitterer, Thermal crack network on CVD TiCN/ α -Al₂O₃ coated cemented carbide cutting tools, *Int. J. Refract. Met. Hard Mater.* 81 (2019) 1–6.
- [14] C. Czettl, J. Thurner, U. Schleinkofer, Knowledge based coating design of CVD TiN–TiBN–TiB₂ architecture, *Int. J. Refract. Met. Hard Mater.* 71 (2018) 330–334.
- [15] N.P. Barradas, C. Jeynes, Advanced physics and algorithms in the IBA DataFurnace, *Nucl. Instrum. Methods Phys. Res B* 266 (2008) 1875–1879.
- [16] J. Filik, A.W. Ashton, P.C.Y. Chang, P.A. Chater, S.J. Day, M. Drakopoulos, M.W. Gerring, M.L. Hart, O.V. Magdysyuk, S. Michalik, A. Smith, C.C. Tang, N.J. Terrill, M.T. Wharmby, H. Wilhelm, Processing two-dimensional X-ray diffraction and small-angle scattering data in DAWN 2, *J. Appl. Crystallogr.* 50 (2017) 959–966.

- [17] J.D. James, J.A. Spittle, S.G.R. Brown, R.W. Evans, A review of measurement techniques for the thermal expansion coefficient of metals and alloys at elevated temperatures, *Meas. Sci. Technol.* 12 (2001) R1–R15.
- [18] R.G. Munro, Material Properties of Titanium Diboride, *J. Res. Natl. Inst. Stand. Technol.* 105 (2000) 709–720.
- [19] M. Bartosik, R. Daniel, C. Mitterer, I. Matko, M. Burghammer, P.H. Mayrhofer, J. Keckes, Cross-sectional X-ray nanobeam diffraction analysis of a compositionally graded CrN_x thin film, *Thin Solid Films* 542 (2013) 1–4.
- [20] M. Stefenelli, J. Todt, A. Riedl, W. Ecker, T. Müller, R. Daniel, M. Burghammer, J. Keckes, X-ray analysis of residual stress gradients in TiN coatings by a Laplace space approach and cross-sectional nanodiffraction: a critical comparison, *J. Appl. Crystallogr.* 46 (2013) 1378–1385.
- [21] J. Almer, U. Lienert, R.L. Peng, C. Schlauer, M. Odén, Strain and texture analysis of coatings using high-energy X-rays, *J. Appl. Phys.* 94 (2003) 697–702.
- [22] M. Tkadletz, C. Hofer, C. Wüstefeld, N. Schalk, M. Motylenko, D. Rafaja, H. Holzschuh, W. Bürgin, B. Sartory, C. Mitterer, C. Czettel, Thermal stability of nanolamellar fcc-Ti_{1-x}Al_xN grown by chemical vapor deposition, *Acta Mater.* 174 (2019) 195–205.
- [23] D.G. Cahill, *Rev. Sci. Instr.* 75 (2004) 5119.
- [24] H. Nowotny, F. Benesovsky, C. Brukl, O. Schob, Die Dreistoffe: Titan–Bor–Kohlenstoff und Titan–Bor–Stickstoff, *Monatsh. Chem.* 92 403–414.
- [25] P. Scherrer, Bestimmung der Größe und der inneren Struktur von Kolloidteilchen mittels Röntgenstrahlen., *Nachrichten von der Gesellschaft der Wissenschaften zu Göttingen, Mathematisch-Physikalische Klasse* 1918 (1918) 98–100.
- [26] International Centre for Diffraction Data, PDF–2 Release, Card number 00–038–1420, 2018.
- [27] International Centre for Diffraction Data, PDF–2 Release, Card number 03–065–1073, 2018.
- [28] R. Bonetti, H.E. Hintermann, *J. Electrochem. Soc.* 124 (1977) C298.
- [29] R. Kieffer, F. Benesovsky, *Hartmetalle*, Springer Verlag, Wien, 1965, p.157.

- [30] M. Tkadletz, N. Schalk, R. Daniel, J. Keckes, C. Czettel, C. Mitterer, Advanced characterization methods for wear resistant hard coatings: A review on recent progress, *Surf. Coat. Technol.* 285 (2016) 31–46.
- [31] C. Saringer, C. Kickinger, F. Munnik, C. Mitterer, N. Schalk, M. Tkadletz, Thermal expansion of magnetron sputtered $\text{TiC}_x\text{N}_{1-x}$ coatings studied by high-temperature X-ray diffraction, *Thin Solid Films* (2019).
- [32] F. Mei, N. Shao, L. Wei, Y. Dong, G. Li, Coherent epitaxial growth and superhardness effects of c-TiN/h-TiB₂ nanomultilayers, *Appl. Phys. Lett.* 87 (2005) 11906.
- [33] N. Schalk, J. Keckes, C. Czettel, M. Burghammer, M. Penoy, C. Michotte, C. Mitterer, Investigation of the origin of compressive residual stress in CVD TiB₂ hard coatings using synchrotron X-ray nanodiffraction, *Surf. Coat. Technol.* 258 (2014) 121–126.
- [34] W. Sun, H. Xiang, F. -Z. Dai, J. Liu, Y. Zhou, Anisotropic surface stability of TiB₂: A theoretical explanation for the easy grain coarsening, *J. Mater. Res.* 32 (2017) 2755–2763.
- [35] M. Bartosik, R. Pitonak, J. Keckes, In Situ High Temperature X-Ray Diffraction Reveals Residual Stress Depth Profiles in Blasted TiN Hard Coatings, *Adv. Eng. Mater.* 13 (2011) 705–711.
- [36] M.W. Chase, NIST-JANAF Thermochemical Tables: Fourth Edition, *J. Phys. Chem. Ref. Data*, Monograph 9, 1998, pp. 1–1951.
- [37] M.K. Samani, X.Z. Ding, N. Khosravian, B. Amin-Ahmadi, Y. Yi, G. Chen, E.C. Neyts, A. Bogaerts, B.K. Tay, Thermal conductivity of titanium nitride/titanium aluminum nitride multilayer coatings deposited by lateral rotating cathode arc, *Thin Solid Films* 578 (2015) 133–138.
- [38] P.H. Mayrhofer, H. Clemens, C. Mitterer, Interfaces in nanostructured thin films and their influence on hardness, *Z. Metallkd.* 96 (2005) 468–480.
- [39] M. Saber, C.C. Koch, R.O. Scattergood, Thermodynamic Grain Size Stabilization Models: An Overview, *Mater. Res. Lett.* 3 (2015) 65–75.
- [40] E.O. Hall, The Deformation and Ageing of Mild Steel: III Discussion of Results, *Proc. Phys. Soc. Lond.* 64 (1951) 747–753.

-
- [41] N.J. Petch, The Cleavage Strength of Polycrystals, *J. Iron Steel Inst. London.* 173 (1953) 25–28.
- [42] R. Daniel, K.J. Martinschitz, J. Keckes, C. Mitterer, The origin of stresses in magnetron-sputtered thin films with zone T structures, *Acta Mater.* 58 (2010) 2621–2633.
- [43] C. Kainz, N. Schalk, M. Tkadletz, C. Mitterer, C. Czettl, Microstructure and mechanical properties of CVD TiN/TiBN multilayer coatings, *Surf. Coat. Technol.* 370 (2019) 311–319

Publication IV

Microstructure, mechanical and thermo-physical properties of CVD $\text{TiC}_x\text{N}_{1-x}$ coatings on cemented carbide substrates grown with C_2H_6 as C feeding precursor

Christina Kainz, Nina Schalk, Michael Tkadletz, Markus Winkler,
Christoph Czettl

Surface & Coatings Technology 394 (2020) 125868



Microstructure, mechanical and thermo-physical properties of CVD $\text{TiC}_x\text{N}_{1-x}$ coatings on cemented carbide substrates grown with C_2H_6 as C feeding precursor

Christina Kainz¹, Nina Schalk¹, Michael Tkadletz², Markus Winkler³, Christoph Czettel⁴

¹ Christian Doppler Laboratory for Advanced Coated Cutting Tools at the Department of Materials Science, Montanuniversität Leoben, Franz-Josef-Straße 18, 8700 Leoben, Austria

² Department of Materials Science, Montanuniversität Leoben, Franz-Josef-Straße 18, 8700 Leoben, Austria

³ Department Thermal Energy Converters, Fraunhofer Institute for Physical Measurement Techniques IPM, Heidenhofstraße 8, 79110 Freiburg, Germany

⁴ Ceratizit Austria GmbH, Metallwerk-Plansee-Straße 71, 6600 Reutte, Austria

Keywords: CVD, $\text{TiC}_x\text{N}_{1-x}$, hard coatings, fracture, thermal conductivity

Abstract

The established industrial processes used for the growth of $\text{TiC}_x\text{N}_{1-x}$ coatings by chemical vapor deposition (CVD) suffer from substantial limitations, either in regard of brittle phase formation or restriction in the $\text{C}/(\text{C}+\text{N})$ ratio. Using the alternative C precursor C_2H_6 allows to overcome these issues. Thus, within this work, the microstructure, phase composition, micro mechanical and thermo-physical properties of CVD $\text{TiC}_x\text{N}_{1-x}$ coatings grown with C_2H_6 were investigated. Through adjustment of the C_2H_6 and N_2 flow in the feed gas, the $\text{C}/(\text{C}+\text{N})$ ratio in the coatings was varied between pure TiN and $\text{TiC}_{0.80}\text{N}_{0.20}$. All coatings are characterized by a single phase face centered cubic structure. The $\langle 110 \rangle$ fiber texture present in all coatings becomes more pronounced with increasing C content. None of the investigated coatings showed thermal cracks on the surface. The thermal conductivity decreases with addition of C from 45 ± 5 W/mK in TiN to 32 ± 3 W/mK in all ternary $\text{TiC}_x\text{N}_{1-x}$ coatings. $\text{TiC}_{0.47}\text{N}_{0.53}$ exhibits the highest hardness (30.0 ± 1.4 GPa), while $\text{TiC}_{0.63}\text{N}_{0.36}$ turned out as the stiffest coating with a Young's modulus of

576±23 GPa. The fracture stress σ_F and toughness K_{IC} are superior in coatings with moderate C and N content, with $TiC_{0.63}N_{0.37}$ being the strongest ($\sigma_F = 7.7\pm0.4$ GPa) and $TiC_{0.47}N_{0.53}$ ($K_{IC} = 4.4\pm0.3$ MPa m^{1/2}) the toughest within this series. Coatings with moderate to high C content were found to exhibit a microstructure provoking a lower thermal conductivity and improved mechanical properties compared to those with a low C/(C+N) ratio.

1. Introduction

α -Al₂O₃ deposited by chemical vapor deposition (CVD) is one of today's most important industrial hard coating materials for indexable carbide cutting tools. Owing to its reasonable hardness, good wear resistance and high oxidation stability, it is an ideal candidate for steel turning applications [1,2]. Al₂O₃ is commonly applied onto a multilayer stack of TiN/TiC_xN_{1-x}/TiC_xN_yO_{1-x-y}. The oxy-nitride layer is required for the deposition of the stable α -Al₂O₃ phase, TiC_xN_{1-x} provides an enhanced mechanical support and TiN serves as diffusion barrier [3]. The most commonly applied C feeding precursors for the synthesis of CVD TiC_xN_{1-x} are CH₄ and CH₃CN, which are used in the high (HT) and moderate temperature (MT) process, respectively [4]. Due to the high stability of CH₄, deposition temperatures exceeding 950 °C are necessary to obtain a sufficient deposition rate. The concomitant economic issues as well as higher tendency for thermal crack and brittle η -phase formation reason the substitution of this method by the MT process. However, the chemical bonding within CH₃CN limits the C/(C+N) ratio in the coatings to ~0.66, which is invariant on both temperature and feed gas composition [5–7].

Within layered materials, a high mismatch between the thermal expansion coefficient of the respective layers is reported to result in thermal cracks during cooling [8]. While Al₂O₃ features a mean thermal expansion coefficient α_{av} (25-1000°C) of 8.3×10^{-6} K⁻¹, α_{av} strongly depends on the C/(C+N) ratio in TiC_xN_{1-x} [9,10]. Similarly, α_{av} of the cemented carbide substrate depends on the Co content [11]. According to literature, the α_{av} mismatch between TiC_xN_{1-x} coatings and the cemented carbide substrate decreases with increasing C/(C+N) ratio [10]. Owing to the C/(C+N) ratio of ~0.66 in industrially prepared CVD TiC_xN_{1-x} coatings, these materials often exhibit a dense

crack network [8]. As the cracks provide diffusion paths and thus foster oxidation, prevention of them is reported to enhance their mechanical properties [12,13].

The possibility to combine the advantages of the MT and HT process, being moderate deposition temperature of ~ 900 °C and free variability of the C content, qualify C_2H_6 as feasible C source. Czettl *et al.* studied the microstructure and morphology of $TiC_{0.80}N_{0.20}$ grown with C_2H_6 as a base system for quaternary $TiB_xC_yN_{1-(x+y)}$ [14]. However, a variation of CVD TiC_xN_{1-x} coatings prepared with C_2H_6 over a broad $C/(C+N)$ range is still missing in literature. Thus, the aim of this study is to correlate the $C/(C+N)$ ratio and resultant microstructure with the micro mechanical and thermo-physical properties of CVD TiC_xN_{1-x} coatings. A fundamental characterization of the coatings was conducted by means of scanning electron microscopy (SEM), X-ray diffraction (XRD), Raman spectroscopy and nanoindentation. Micro-mechanical bending tests allowed insight into the fracture behavior of the materials. Finally, the thermal conductivity, which is a decisive parameter for heat management of materials, was evaluated by time-domain thermoreflectance (TDTR).

2. Experimental methods

All coatings investigated within this study were deposited in an industrial scale thermal CVD plant type SCT600 TH by Sucotec. The feed gas mixture contained C_2H_6 , $TiCl_4$, N_2 , H_2 and Ar. In order to obtain coatings with varying $C/(C+N)$ ratios, the C feeding precursor was varied between 0 and 1.52 vol.%. A temperature of 920 °C and a pressure of 160 mbar were chosen for the deposition. The coatings were grown onto substrates in SNUN geometry (according to ISO 1832), containing 76 wt. % WC, 12 wt. % Co and 12 wt. % mixed carbides. To avoid inter diffusion between coating and substrate, all C containing coatings were grown on a ~ 0.3 μm thick stoichiometric TiN base layer. The thickness of all coatings was between 5.1 and 6.7 μm .

The chemical composition of the coatings was determined using a glow discharge optical emission spectroscope (GDOES) of type JY10000 from Jobin-Yvon Horiba. Calibration of the elements of interest was conducted using pressed powder reference materials. An Ultra 55 plus scanning electron microscope (SEM) from Zeiss allowed visualization of the coating surface. Coating cross-sections were obtained by focused ion beam (FIB) milling on a crossbeam workstation of type

Nova200 Nanolab from FEI. The crystallographic structure of the coatings was studied by XRD using a Bruker AXS D8 Advance diffractometer operating with Cu-K α radiation. Phase identification was conducted in Bragg-Brentano geometry. Residual stress determination and acquisition of pole figures were realized on a Bruker AXS D8 Advance DaVinci diffractometer. The stress state of the coatings was determined applying the $\sin^2\psi$ method in χ mode [15]. Up to a C/(C+N) ratio of 0.63, the 422 reflection was used for the evaluation. ψ was varied between 0 and 58.5° in such a way that equidistant $\sin^2\psi$ steps were obtained. For the coating with a higher C content, the 420 reflection was chosen, due to the close vicinity of the 422 reflection to a substrate reflection at high C/(C+N) ratios. Here, ψ ranged from 0 to 48°. Elastic constants used to derive stress from strain were taken from ref. [16]. XRD pole figures of the 111, 200 and 220 reflections were collected to assess the texture of the coatings. The azimuthal and polar angle ranged from 0 to 360° and 0 to 80°, respectively, and the step size was 5° in both cases. Processing and visualization of the experimental XRD pole figure data was realized using the MTEX toolbox [17]. Raman spectroscopy complemented the investigation of the phase composition by XRD. The measurement was carried out on a Labram-HR800 spectrometer by Horiba Jobin-Yvon operating with a frequency-doubled Nd YAG laser ($\lambda=532$ nm).

Hardness and Young's modulus of the coatings were determined using a UMIS nanoindenter from Fischer-Cripps Laboratories with a diamond Berkovich tip. A load range between 30 and 12 mN with a decrement of 0.75 mN was applied. Data was analyzed according to the Oliver and Pharr method [18]. The fracture mechanical behavior of the TiC $_x$ N $_{1-x}$ coatings was evaluated by bending tests performed on free-standing micro cantilevers of the coatings. Specimen preparation was done by FIB milling on a DualBeam Versa 3D system by FEI. The dimensions of the micro cantilevers amounted to a bending length of ~9 μm and a cross-section of ~3 \times 3 μm^2 . Two sets of specimen were fabricated: the first set, for evaluation of the fracture toughness, exhibited a sharp notch located ~1.5 μm from the micro cantilever's support. The actual depth of the notch was measured post mortem by SEM. The second set without notch allowed determination of the fracture stress. For each set of notched and unnotched micro cantilevers, a minimum of three specimens was tested. A

FIB made circle facilitated the subsequent positioning with the indenter. A spheroconical tip, installed within a Hysitron TriboIndenter TI950 system, was subsequently used for imaging and loading of the specimen. Loading of the micro cantilevers was performed displacement controlled at a rate of 5 nm/s. The recorded load-displacement curve allowed determination of fracture stress and toughness according to the method of Matoy *et al.* [19].

TDTR experiments were conducted to determine the thermal conductivity of the coatings. The operational principle of this measurement follows a pump probe system realized with a pulsed laser [20]. Laser pulses with a pulse duration of 500 fs, a pulse repetition rate of 80 MHz, a wavelength of 785 nm and an average laser power of 28 mW were generated by the Ti:Sapphire laser system Mai Tai from Spectra-Physics. The pump beam modulation frequency amounted to 10.7 MHz. The time delay between pump and probe beam was in the range of 0 to 3600 ps. 70 nm of pure Al were deposited on the sample surface prior to the measurement to serve as transducer layer. Oxidized and un-oxidized Si wafers were used for validation of the measurement system, which was done prior to the actual sample measurement.

3. Results and discussion

In Fig. 1 the influence of the C_2H_6 flow rate on the elemental composition within the coatings is presented. A $C/(C+N)$ ratio of 0.63, which is comparable to the one of coatings prepared with CH_3CN [21,22], is obtained when applying a C_2H_6 fraction of 0.8 vol.%. At a fraction of 1.5 vol.%, a higher $C/(C+N)$ ratio of 0.80 is achieved. To the best of our knowledge, a C content that high is not realizable when using solely CH_3CN or a combination thereof with other hydrocarbons [4,21,23]. The moderate deposition temperature in comparison to the HT process with simultaneous lower mismatch in the theoretical stress of cemented carbide and coating are thus benefits of using C_2H_6 [24]. The GDOES composition profiles showed a constant $C/(C+N)$ ratio throughout the coating thickness in all ternary coatings (cf. Suppl. Fig. 1). Although the N and C content within the coatings changed significantly with the feed gas composition, all coatings exhibit the same Ti content of ~50 at.% according to the GDOES measurements. The deposition rate was ~0.8 $\mu\text{m}/\text{h}$ for TiN,

TiC_{0.32}N_{0.68} and TiC_{0.80}N_{0.20}, whereas it only amounted to ~ 0.68 $\mu\text{m}/\text{h}$ for the coatings with moderate C/(C+N) ratios.

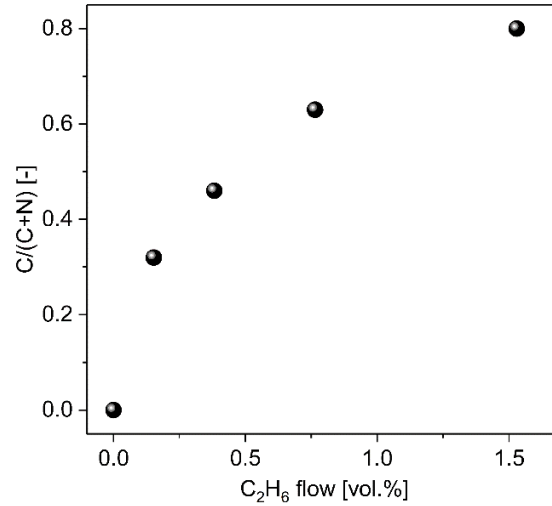


Fig. 1: C/(C+N) ratio of the TiC_xN_{1-x} coatings depending on the C₂H₆ flow rate.

The step wise change from N rich to N poor resulted in a pronounced difference of the surface and cross-sectional microstructure of the coatings as depicted in Figs. 2a-e. TiN exhibits faceted grains on the surface and columnar ones in the cross-section (Fig. 2a). The large grains partly extend over the whole coating thickness and display competitive growth. Up to a C/(C+N) ratio of 0.47, the addition of C results in a needle like surface structure (Figs. 2b and c), whereas TiC_{0.63}N_{0.37} and TiC_{0.80}N_{0.20} exhibit equiaxed grains on the surface. While TiC_{0.63}N_{0.37} shows both large and small grains on the surface (Fig. 2d), a more homogeneous grain size distribution is evident for TiC_{0.80}N_{0.20} (Fig. 2e). On the surface of TiC_{0.63}N_{0.37} and TiC_{0.80}N_{0.20}, twinned crystals are visible, which are commonly observed in CVD TiC_xN_{1-x} coatings over a broad compositional range [22,25,26]. The influence of the C content on the cross-sectional microstructure is less pronounced in comparison to the coatings' surface. After the small grained TiN base layer, the grains in the actual TiC_xN_{1-x} layer form V-shaped columns, which increase in size as the coating thickness increases. This microstructure is typical for the prevailing competitive growth [27,28]. It appears that the TiC_xN_{1-x} coatings with low amounts of C (Figs. 1b and c) also exhibit some small globular grains in addition to the columnar ones. Thus, TiC_{0.63}N_{0.37} and TiC_{0.80}N_{0.20} seem to display more pronounced features of competitive growth. The ternary coatings show a smaller column width compared to binary TiN. No cracks were

visible on the surface or in the cross section of the herein investigated coatings. Stylianou *et al.* investigated the effect of the Co content in the substrate on the thermal crack formation in CVD $\text{TiC}_x\text{N}_{1-x}$ coatings. The authors report on the absence of thermal cracks at Co contents exceeding 10 wt.% [11]. Thus, the absence of cracks in the here investigated coatings is presumably a result of the high Co content (12 wt.%) in the substrate. In accordance to the microscopic changes, also the color of the coatings is influenced by the chemical composition. TiN features the typical golden color, $\text{TiC}_{0.32}\text{N}_{0.68}$ is greyish red and the coatings with higher C content display a grey hue.

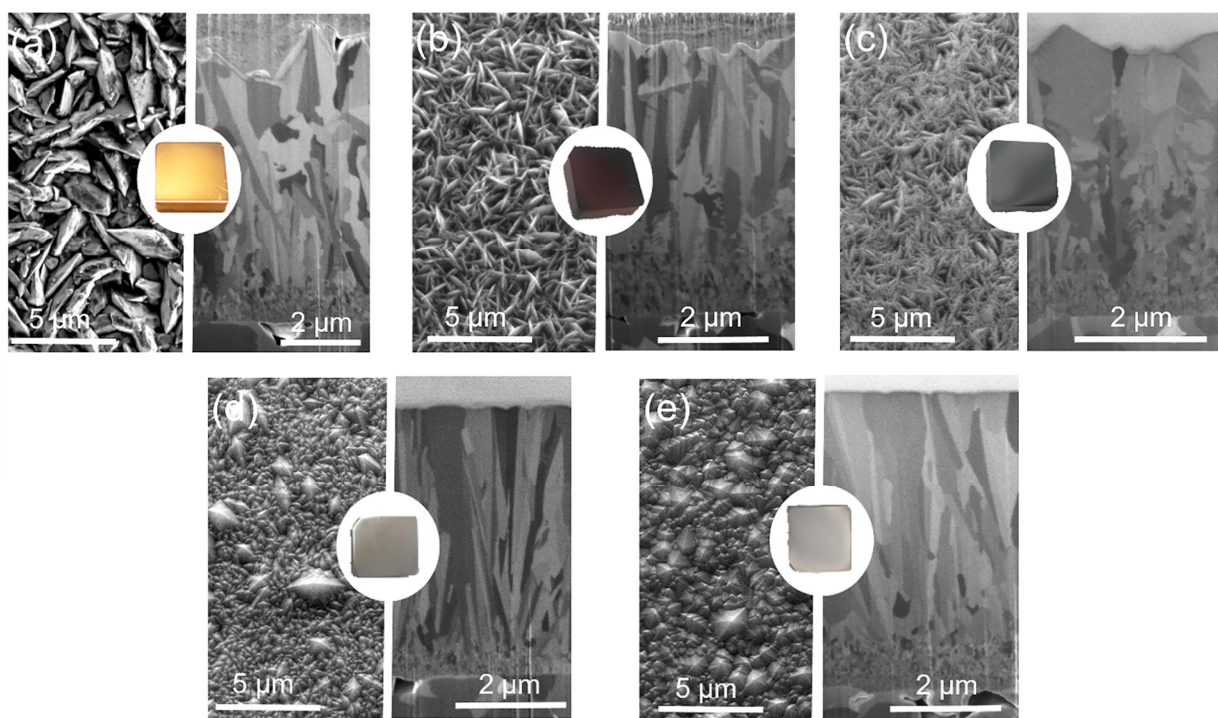


Fig. 2: Pictures and SEM images of the surface and cross-sectional microstructure of (a) TiN, (b) $\text{TiC}_{0.32}\text{N}_{0.68}$, (c) $\text{TiC}_{0.47}\text{N}_{0.53}$, (d) $\text{TiC}_{0.63}\text{N}_{0.37}$ and (e) $\text{TiC}_{0.80}\text{N}_{0.20}$.

The evolution of the crystallographic structure, from bottom to top with increasing $C/(C+N)$ ratio, is shown in Fig. 3a. The peak position of the 111 and 220 reflection of TiN is in good agreement with the reference ICDD file of face-centered cubic (fcc) TiN [29]. With increasing C content, the peaks shift towards the reported peak position of TiC at lower diffraction angles, while the crystallographic structure remains fcc [30]. This observation is in accordance to calculations by Ivashchenko *et al.*, who predicted miscibility of TiN and TiC over the whole compositional range

[16]. None of the diffractograms show any indication for the brittle η -phase in the substrate, which is commonly observed when applying the HT process [7]. Coarse grained TiN and C rich $\text{TiC}_x\text{N}_{1-x}$ coatings exhibit lower peak widths in comparison to the small grained $\text{TiC}_x\text{N}_{1-x}$ with a low $C/(C+N)$ ratio. Since both, a smaller size of coherently diffracting domains as well as enhanced micro strains contribute to XRD peak broadening [31–33], the observed differences in the peak widths are in good agreement with the microstructure of the coatings (Figs. 2a-e). From the X ray diffractograms, it can be seen that the intensity of the 220 reflection increases with increasing $C/(C+N)$ ratio. As the texture in TiN based coatings is reported to affect adhesion, hardness as well as tribological properties [5,34,35], the dominant texture in the investigated coatings was investigated through acquisition of pole figures. Fig. 3b shows the recalculated pole figures of the 220 reflection for all investigated samples. A summary of the 111, 200 and 220 pole figures of all samples, normalized to the highest intensity within one coating, is presented in Suppl. Fig. 2. All coatings exhibit a $\langle 110 \rangle$ fiber texture, which becomes more pronounced with increasing C content, as can be seen in Fig. 3c.

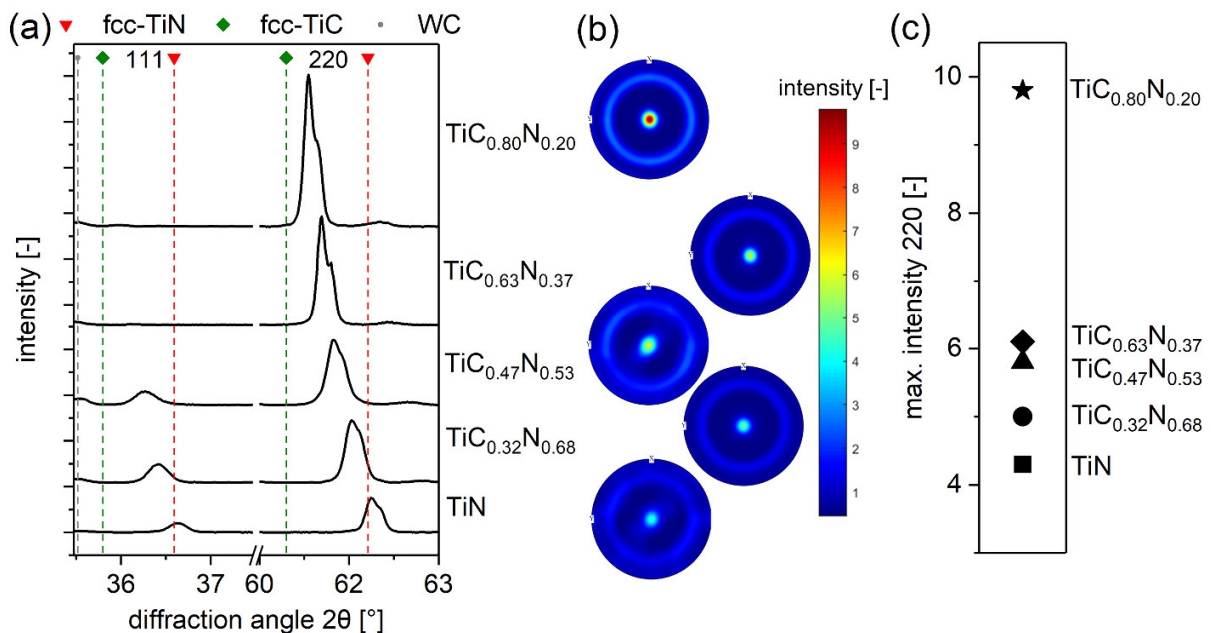


Fig. 3: (a) X-ray diffractograms and (b) recalculated 220 pole figures of the $\text{TiC}_x\text{N}_{1-x}$ coatings. (c) Comparison of the intensity maxima in the 220 pole figure of the respective coating.

Raman spectra of the coatings were recorded to complement the crystallographic phase investigation with special focus on possible amorphous phases. The obtained Raman spectra (Fig. 4a) are in good agreement with Dreiling *et al.*, who studied CVD $\text{TiC}_x\text{N}_{1-x}$ coatings grown with CH_4 and CH_3CN [21]. With increasing $\text{C}/(\text{C}+\text{N})$ ratio, the positions of the transversal acoustical and transversal optical modes shift closer towards each other, which was also observed by Saringer *et al.* [10]. None of the investigated coatings showed indications for amorphous C, which seems reasonable, considering the metal to non-metal ratio of 1:1 within all investigated samples [36].

The mechanical properties and residual stress of the investigated coatings are summarized in Fig. 4b. The formation of a $\text{TiC}_x\text{N}_{1-x}$ solid solution results in a pronounced hardness increase from 20.2 ± 1.4 GPa in TiN to 26.7 ± 1.6 GPa in $\text{TiC}_{0.32}\text{N}_{0.68}$. The maximum hardness of $\text{TiC}_{0.47}\text{N}_{0.53}$ (30.0 ± 1.4 GPa) among the ternary coatings is reasoned by both, the C content and the microstructure. On the one hand, an increasing $\text{C}/(\text{C}+\text{N})$ ratio is accompanied by a more pronounced covalent bonding character, which is reported to exhibit high hardness [37–39]. On the other hand, the hardness is positively affected by the small grained microstructure through Hall Petch hardening [40,41]. These concurring phenomena are assumed to be the reason for the hardness plateau after a moderate $\text{C}/(\text{C}+\text{N})$ ratio is reached. The Young's modulus increases stepwise with the addition of C to TiN up to $\text{TiC}_{0.63}\text{N}_{0.37}$ and afterwards slightly decreases. This evolution of the Young's modulus with increasing C content is in good agreement with calculations by Ivashchenko *et al.* They report on an increment of the Young's modulus with addition of C to TiN [16]. Within the investigated coatings, $\text{TiC}_{0.47}\text{N}_{0.53}$ exhibits the highest H^3/E^2 ratio, which allows a rough estimation on the resistance to plastic deformation [42]. In addition to hardness and Young's modulus, the effect of the $\text{C}/(\text{C}+\text{N})$ ratio on the determined residual stress σ is also shown in Fig. 4b. The $\sin^2\psi$ plots used for the evaluation are shown in Suppl. Fig. 3. All investigated samples exhibit tensile residual stress. As mentioned above, none of the coatings display cracks on the surface. The decrement of σ with increasing C content is in agreement with theoretical considerations, as α_{av} (25-1000°C) decreases with increasing C content from 9.59×10^{-6} K⁻¹ in TiN to 8.27×10^{-6} K⁻¹ in $\text{TiC}_{0.80}\text{N}_{0.20}$ [10]. As a consequence, the mismatch between α_{av} of coating and substrate decreases and thus the tensile residual stress is lower. For the coatings with $\text{C}/(\text{C}+\text{N})$ ratios ≥ 0.47 , the tensile residual stress

seems to approach a minimum of ~ 370 MPa, although the α_{av} mismatch between coating and substrate further decreases. In addition to residual stress arising from the aforementioned α_{av} mismatch, also intrinsic stress should not be neglected in the present discussion. As proposed by El Azhari *et al.*, defect incorporation during deposition and grain boundary relaxation may influence the intrinsic stress state of CVD TiC_xN_{1-x} coatings as well [43].

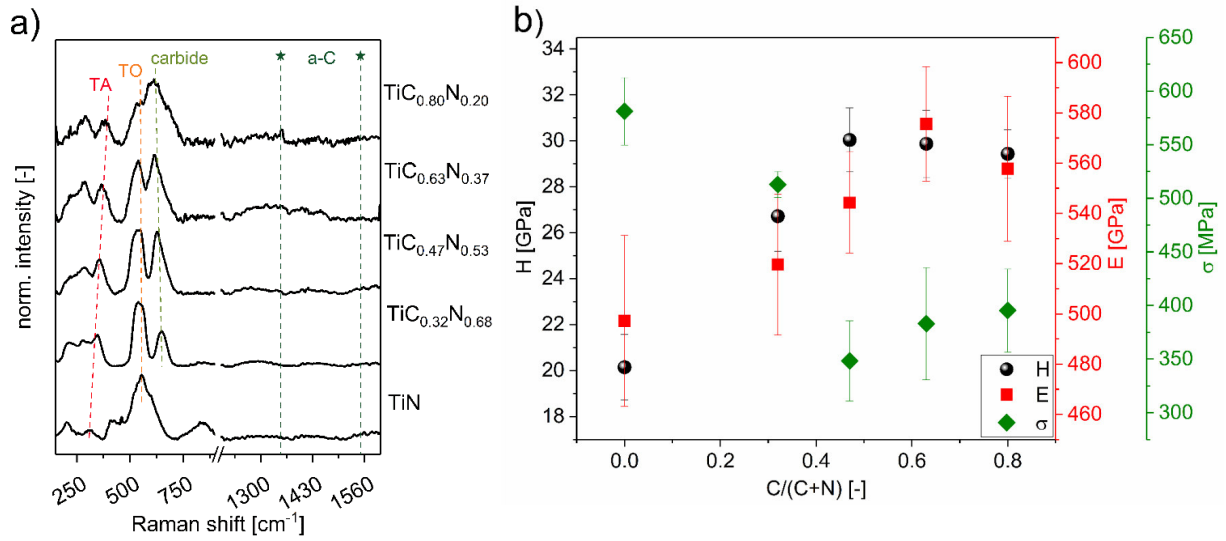


Fig. 4: (a) Raman spectra of the TiC_xN_{1-x} coatings. The position of the transversal acoustical (TA), transversal optical (TO) and carbide mode are depicted as well as the two positions of amorphous C (a-C) [21,36]. (b) Hardness, Young's modulus and residual stress of the TiC_xN_{1-x} coatings.

Micro-mechanical bending tests allowed to correlate the fracture behavior of the investigated coatings with their C content. An unnotched FIB made bending beam, which was used for the investigation of the fracture stress, is shown in Fig. 5b. Load-displacement curves recorded in the micro mechanical bending tests reveal a linear-elastic fracture behavior for all coatings, which is typical for ceramic materials. Failure occurred at the end of the respective curve by brittle fracture. The fracture stress increases gradually from 4.6 ± 0.4 GPa in TiN to 7.7 ± 0.8 GPa in $TiC_{0.80}N_{0.20}$ (Fig. 5a). The experiments are in agreement with theoretical considerations that a higher C/(C+N) ratio results in an increased strength due to the higher fraction of strong covalent Ti-C bonds [37-39]. Taking into account different C/(C+N) ratios, the obtained results are in good agreement with data reported in literature [44,45]. The fracture toughness, denoted by the critical stress intensity factor

K_{IC} , can be determined from notched bending beams [46]. Initially, the fracture toughness is hardly affected by the addition of C, as TiN ($3.1 \pm 0.3 \text{ MPa m}^{1/2}$) and $\text{TiC}_{0.32}\text{N}_{0.68}$ ($3.5 \pm 0.1 \text{ MPa m}^{1/2}$) exhibit a similar K_{IC} value. However, further addition of C results in a pronounced increase of the fracture toughness, with the highest K_{IC} value in $\text{TiC}_{0.47}\text{N}_{0.53}$ ($4.4 \pm 0.3 \text{ MPa m}^{1/2}$). A further increment in the $C/(C+N)$ ratio provokes a slight reduction of the fracture toughness. The behavior observed in case of the ternary $\text{TiC}_x\text{N}_{1-x}$ coatings is suggested to rely on a superimposition of two mechanisms. While $\text{TiC}_{0.32}\text{N}_{0.68}$ and $\text{TiC}_{0.47}\text{N}_{0.53}$ exhibit small grains and thus multiple crack deflection sites, the $\langle 110 \rangle$ texture is more prevalent in $\text{TiC}_{0.63}\text{N}_{0.37}$ and $\text{TiC}_{0.80}\text{N}_{0.20}$ (compare Fig. 3c) [47]. CVD TiN with a random orientation is reported to show a noteworthy lower K_{IC} value ($2.2 \pm 0.4 \text{ MPa m}^{1/2}$) compared to the $\langle 110 \rangle$ textured TiN in this study [48]. It may thus be suggested that a more pronounced $\langle 110 \rangle$ texture results in a better fracture resistance also in ternary $\text{TiC}_x\text{N}_{1-x}$ coatings. Post-mortem fracture cross sections of the investigated coatings (Fig. 5b) display the typical appearance of brittle fracture. According to Ivashchenko *et al.*, C_{12} is lower than C_{44} for all here investigated coatings [16]. The Pettifor criterion thus predicts that all $\text{TiC}_x\text{N}_{1-x}$ coatings are brittle [49]. The micrographs suggest an intergranular fracture, which is in good agreement with observations from other authors for similar materials [44,50].

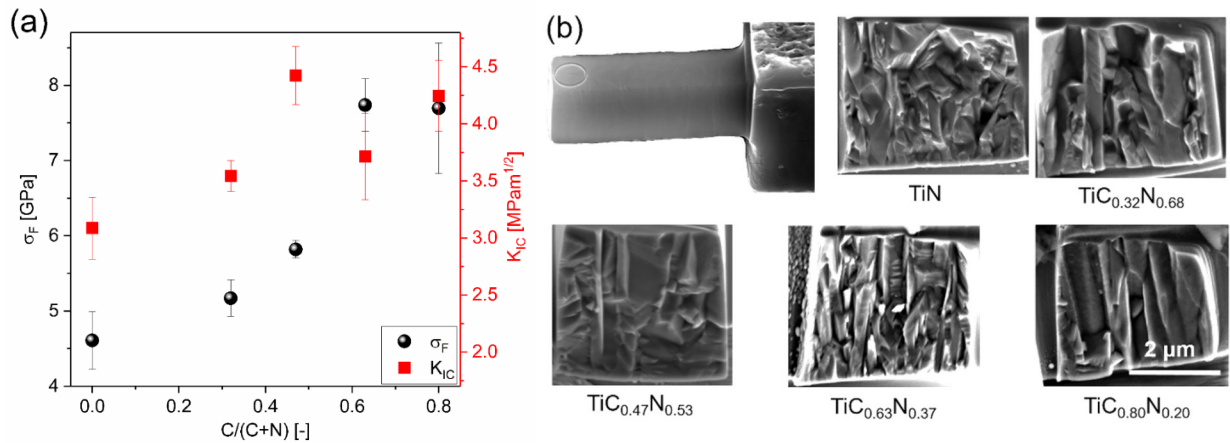


Fig. 5: (a) Fracture stress σ_F and toughness K_{IC} of the $\text{TiC}_x\text{N}_{1-x}$ coatings. b) SE micrograph of an unnotched bending specimen, as well as post-mortem fracture cross-sections of each investigated sample.

A lower thermal conductivity is reported to be beneficial for cutting applications as this allows a good protection of the substrate from overheating [51]. The thermal conductivity of the

coatings was thus assessed by means of TDTR and the results are summarized in Fig. 6. The specific heat capacity c_p and density of the $\text{TiC}_x\text{N}_{1-x}$ coatings was estimated from the values of TiN and TiC in dependence of the $C/(C+N)$ ratio according to a general rule of mixtures [39,52]. Following this estimation, the c_p of the coatings decreases linearly with increasing $C/(C+N)$ ratio. TiN exhibits a thermal conductivity of 45 ± 5 W/mK, which is higher in comparison to data reported in literature. Samani *et al.* measured a thermal conductivity of ~ 11 W/mK for a TiN coating deposited using the lateral rotating cathode arc method [53]. The discrepancy is most likely due to the difference in microstructure between the material investigated in literature and the one in our study. In contrast to a grain size of ~ 1.2 μm in the TiN coating studied by Samani *et al.*, the columnar grains of TiN in our work partly extend over the whole coating thickness of ~ 6 μm . Furthermore, CVD TiN coatings are reported to exhibit a lower defect density in comparison to the ones deposited by deposition techniques relying on arc evaporation [54]. Grain refinement and higher defect density result in a more pronounced phonon scattering, which provokes a decrement of the thermal conductivity [53]. All ternary coatings investigated here show a comparable thermal conductivity of ~ 33 W/mK. The lower thermal conductivity in comparison to TiN can be again explained by the smaller grain size and thus stronger phonon scattering of the C containing coatings. Furthermore, the scattering is more pronounced in ternary materials like $\text{TiC}_x\text{N}_{1-x}$ in comparison to binary ones due to the alloy scattering [55].

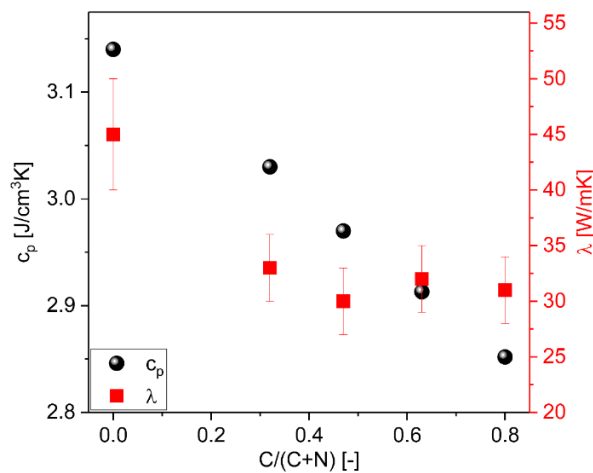


Fig. 6: Estimated specific heat capacity c_p and measured thermal conductivity λ of the $\text{TiC}_x\text{N}_{1-x}$ coatings.

4. Conclusions

A series of $\text{TiC}_x\text{N}_{1-x}$ coatings was grown by CVD with varying C_2H_6 fraction in the feed gas and their microstructure was correlated with the micro mechanical properties and thermal conductivity. Using C_2H_6 as C feeding gas allows to vary the (C/C+N) ratio freely and thus to increase the amount of incorporated C in comparison to CH_3CN . Thus, the present study confirms the feasibility to use C_2H_6 as C feeding precursor for the deposition of $\text{TiC}_x\text{N}_{1-x}$ coatings. The microstructure appeared large columnar grained in TiN, needle like in $\text{TiC}_{0.32}\text{N}_{0.68}$ and $\text{TiC}_{0.47}\text{N}_{0.53}$ and equiaxed in the coatings with high C content. All coatings exhibited an fcc-TiN based crystal structure with no indication for amorphous C. A higher C content resulted in a more pronounced $\langle 110 \rangle$ fiber texture. None of the investigated coatings featured cracks on the surface, which is ascribed to the low mismatch in α_{av} between coating and substrate. As the C/(C+N) ratio increased, the tensile residual stress decreased. The C/(C+N) ratio significantly affected the mechanical properties of the coatings: $\text{TiC}_{0.47}\text{N}_{0.53}$ was the hardest and toughest among the tested coatings, while $\text{TiC}_{0.63}\text{N}_{0.37}$ exhibited the highest fracture stress. The thermal conductivity decreased with addition of C to TiN, but was largely unaffected by the amount of C in the coating. In conclusion, the small grains in coatings with moderate C/(C+N) ratio and a stronger fracture resistant $\langle 110 \rangle$ fiber texture in those with a high C content, both positively affect the micro mechanical properties and thermal conductivity of the material.

Acknowledgements

The authors want to thank Marianne Penoy, MSc. (CERATIZIT Luxembourg s.à.r.l.) for the GDOES measurements. Further, we are grateful to Martina Dienstleder (Austrian Centre for Electron Microscopy and Nanoanalysis) for FIB/SEM work. The financial support by the Austrian Federal Ministry for Digital and Economic Affairs and the National Foundation for Research, Technology and Development is gratefully acknowledged.

References

- [1] C. Mitterer, PVD and CVD Hard Coatings, in: *Comprehensive Hard Materials*, Elsevier, 2014, pp. 449–467.
- [2] D. Hochauer, C. Mitterer, M. Penoy, C. Michotte, H.P. Martinz, M. Kathrein, Titanium doped CVD alumina coatings, *Surf. Coat. Technol.* 203 (2008) 350–356.
- [3] S. Rупpi, Enhanced performance of α -Al₂O₃ coatings by control of crystal orientation, *Surf. Coat. Technol.* 202 (2008) 4257–4269.
- [4] H. Holzschuh, Chemical-vapor deposition of wear resistant hard coatings in the Ti–B–C–N system: properties and metal-cutting tests, *Int. J. Refract. Met. Hard Mater.* 20 (2002) 143–149.
- [5] L. von Fieandt, K. Johansson, T. Larsson, M. Boman, E. Lindahl, On the growth, orientation and hardness of chemical vapor deposited Ti(C,N), *Thin Solid Films* 645 (2018) 19–26.
- [6] L. von Fieandt, T. Larsson, M. Boman, E. Lindahl, Texture formation in chemical vapor deposition of Ti(C,N), *J. Cryst. Growth* 508 (2019) 90–95.
- [7] S. Rупpi, Advances in chemically vapour deposited wear resistant coatings, *J. Phys. IV France* 11 (2001) Pr3 847–859.
- [8] M. Gassner, N. Schalk, M. Tkadletz, C. Czettel, C. Mitterer, Thermal crack network on CVD TiCN/ α -Al₂O₃ coated cemented carbide cutting tools, *Int. J. Refract. Met. Hard Mater.* 81 (2019) 1–6.
- [9] H.O. Pierson, *Handbook of chemical vapor deposition*, 2nd ed., Noyes Publications, Norwich NY, 1999.
- [10] C. Saringer, C. Kickingger, F. Munnik, C. Mitterer, N. Schalk, M. Tkadletz, Thermal expansion of magnetron sputtered TiC_xN_{1-x} coatings studied by high-temperature X-ray diffraction, *Thin Solid Films* 688 (2019) 137307.
- [11] R. Stylianou, D. Velic, W. Daves, W. Ecker, A. Stark, N. Schell, M. Tkadletz, N. Schalk, C. Czettel, C. Mitterer, Stress relaxation through thermal crack formation in CVD TiCN coatings grown on WC-Co with different Co contents, *Int. J. Refract. Met. Hard Mater.* 86 (2020) 105102.
- [12] X. Chen, H. Liu, Q. Guo, S. Sun, Oxidation behavior of WC–Co hard metal with designed multilayer coatings by CVD, *Int. J. Refract. Met. Hard Mater.* 31 (2012) 171–178.

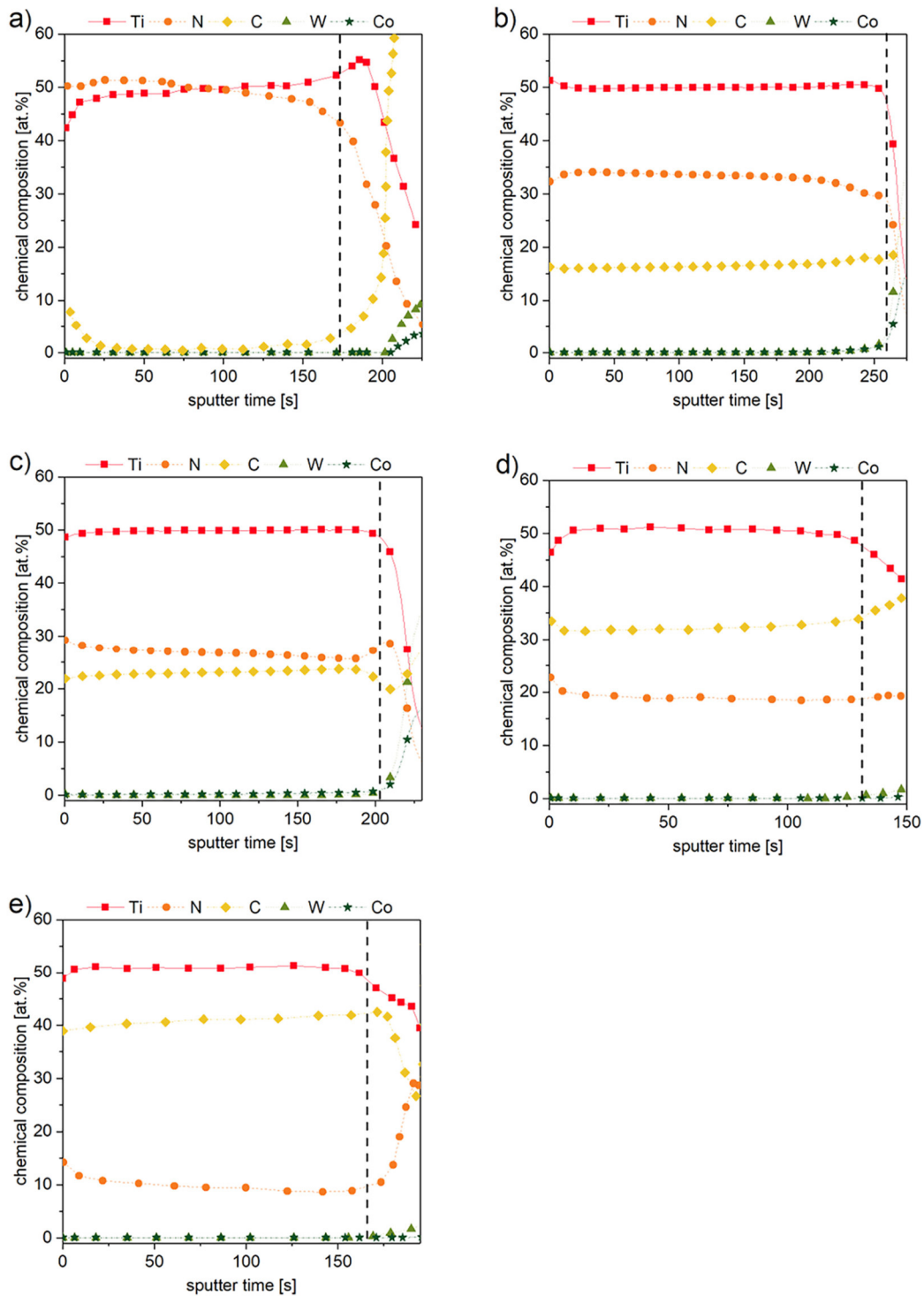
- [13] D. Hochauer, C. Mitterer, M. Penoy, S. Puchner, C. Michotte, H.P. Martinz, H. Hutter, M. Kathrein, Carbon doped α -Al₂O₃ coatings grown by chemical vapor deposition, *Surf. Coat. Technol.* 206 (2012) 4771–4777.
- [14] C. Czettel, C. Mitterer, M. Penoy, C. Michotte, M. Kathrein, C₂H₆ as precursor for low pressure chemical vapor deposition of TiCNB hard coatings, *Surf. Coat. Technol.* 215 (2013) 127–132.
- [15] U. Welzel, J. Ligot, P. Lamparter, A.C. Vermeulen, E.J. Mittemeijer, Stress analysis of polycrystalline thin films and surface regions by X-ray diffraction, *J. Appl. Crystallogr.* 38 (2005) 1–29.
- [16] V.I. Ivashchenko, P.E.A. Turchi, A. Gonis, L.A. Ivashchenko, P.L. Skrynskii, Electronic origin of elastic properties of titanium carbonitride alloys, *Metall. Mater. Trans A* 37 (2006) 3391–3396.
- [17] F. Bachmann, R. Hielscher, H. Schaeben, Texture Analysis with MTEX – Free and Open Source Software Toolbox, *Solid State Phenom.* 160 (2010) 63–68.
- [18] W.C. Oliver, G.M. Pharr, An improved technique for determining hardness and elastic modulus using load and displacement sensing indentation experiments, *J. Mater. Res.* 7 (1992) 1564–1583.
- [19] K. Matoy, H. Schönherr, T. Detzel, T. Schöberl, R. Pippan, C. Motz, G. Dehm, A comparative micro-cantilever study of the mechanical behavior of silicon based passivation films, *Thin Solid Films* 518 (2009) 247–256.
- [20] D.G. Cahill, Analysis of heat flow in layered structures for time-domain thermoreflectance *Rev. Sci. Instr.* 75 (2004) 5119–5121.
- [21] I. Dreiling, A. Haug, H. Holzschuh, T. Chassé, Raman spectroscopy as a tool to study cubic Ti–C–N CVD coatings, *Surf. Coat. Technol.* 204 (2009) 1008–1012.
- [22] C. Czettel, C. Mitterer, U. Mühle, D. Rafaja, S. Puchner, H. Hutter, M. Penoy, C. Michotte, M. Kathrein, CO addition in low-pressure chemical vapour deposition of medium-temperature TiC_xN_{1-x} based hard coatings, *Surf. Coat. Technol.* 206 (2011) 1691–1697.

- [23] A. Paseuth, H. Fukui, S. Okuno, H. Kanaoka, Y. Okada, Microstructure, mechanical properties, and cutting performance of $\text{TiC}_x\text{N}_{1-x}$ coatings with various x values fabricated by moderate temperature chemical vapor deposition, *Surf. Coat. Technol.* 260 (2014) 139–147.
- [24] R. Daniel, K.J. Martinschitz, J. Keckes, C. Mitterer, The origin of stresses in magnetron-sputtered thin films with zone T structures, *Acta Mater.* 58 (2010) 2621–2633.
- [25] A. Paseuth, H. Fukui, K. Yamagata, Improvement of mechanical properties and cutting performance of modified MT- $\text{TiC}_x\text{N}_{1-x}$ coating by moderate temperature chemical vapor deposition, *Surf. Coat. Technol.* 291 (2016) 54–61.
- [26] D. -J. Cheng, W. -P. Sun, M. -H. Hon, The morphology and structure of chemically vapour-deposited $\text{Ti}(\text{C},\text{N})$ coatings, *Thin Solid Films* 146 (1987) 45–53.
- [27] C.V. Thompson, Structure Evolution During Processing of Polycrystalline Films, *Annu. Rev. Mater. Sci.* 30 (2000) 159–190.
- [28] P.B. Barna, M. Adamik, J. Lábár, L. Kövér, J. Tóth, A. Dévényi, R. Manaila, Formation of polycrystalline and microcrystalline composite thin films by codeposition and surface chemical reaction, *Surf. Coat. Technol.* 125 (2000) 147–150.
- [29] International Centre for Diffraction Data, PDF-2 Release, Card number 00-038-1420, 2018.
- [30] International Centre for Diffraction Data, PDF-2 Release, Card number 00-032-1383, 2018.
- [31] B.D. Cullity, *Elements of X-ray Diffraction*, Addison-Wesley, Reading Massachusetts, 1978.
- [32] R.E. Dinnebier, A. Leineweber, J.S.O. Evans, *Rietveld refinement: Practical powder diffraction pattern analysis using TOPAS*, De Gruyter, Berlin, Boston, 2019.
- [33] H.P. Klug, L.E. Alexander, *X-ray diffraction procedures*, 2nd edition, John Wiley & Sons, Ltd, New York, 1974.
- [34] J. Wagner, C. Mitterer, M. Penoy, C. Michotte, W. Wallgram, M. Kathrein, The effect of deposition temperature on microstructure and properties of thermal CVD TiN coatings, *Int. J. Refract. Met. Hard Mater.* 26 (2008) 120–126.
- [35] S. Akkaya, B. Yıldız, M. Ürgen, Orientation dependent tribological behavior of TiN coatings, *J. Phys.: Condens. Matter* 28 (2016) 134009.

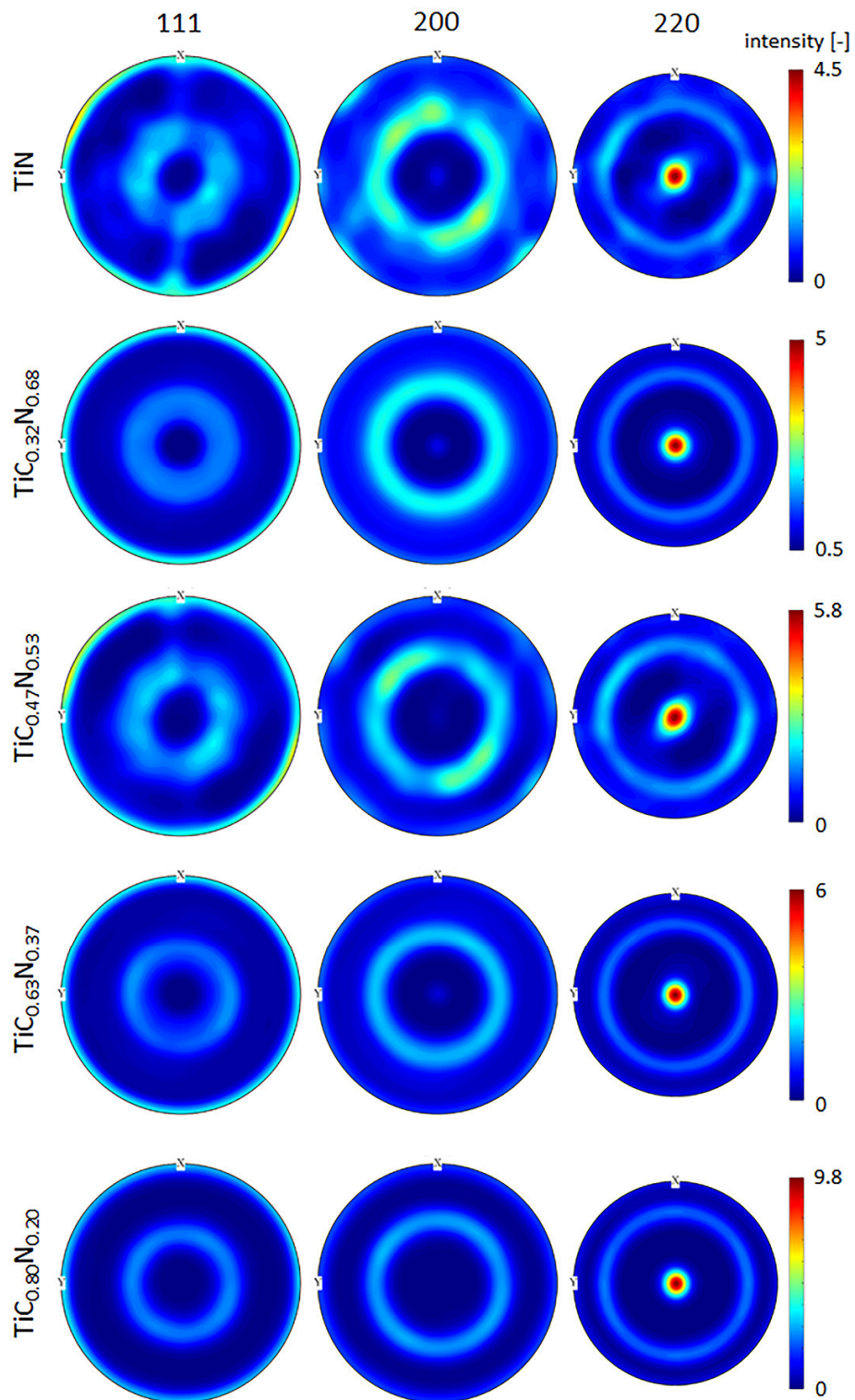
- [36] A.C. Ferrari, J. Robertson, Interpretation of Raman spectra of disordered and amorphous carbon, *Phys. Rev. B* 61 (2000) 14095–14107.
- [37] H. Holleck, Material selection for hard coatings, *J. Vac. Sci. Technol. A* 4 (1986) 2661–2669.
- [38] H. Holleck, Basic principles of specific application of ceramic materials as protective layers, *Surf. Coat. Technol.* 43/44 (1990) 245–258.
- [39] H.O. Pierson, *Handbook of refractory carbides and nitrides: properties, characteristics, processing, and applications*, Noyes Publications, New York, 1996.
- [40] E.O. Hall, The Deformation and Ageing of Mild Steel: III Discussion of Results, *Proc. Phys. Soc. Lond.* 64 (1951) 747–753.
- [41] N.J. Petch, The Cleavage Strength of Polycrystals, *J. Iron Steel Inst. London.* 173 (1953) 25–28.
- [42] A. Leyland, A. Matthews, On the significance of the H/E ratio in wear control: a nanocomposite coating approach to optimised tribological behaviour, *Wear* 246 (2000) 1–11.
- [43] I. El Azhari, J. García, F. Soldera, S. Suarez, E. Jiménez-Piqué, F. Mücklich, L. Llanes, Contact damage investigation of CVD carbonitride hard coatings deposited on cemented carbides, *Int. J. Refract. Met. Hard Mater.* 86 (2020) 105050.
- [44] I. El Azhari, J. Garcia, M. Zamanzade, F. Soldera, C. Pauly, L. Llanes, F. Mücklich, Investigations on micro-mechanical properties of polycrystalline Ti(C,N) and Zr(C,N) coatings, *Acta Mater.* 149 (2018) 364–376.
- [45] C. Kainz, N. Schalk, M. Tkadletz, C. Mitterer, C. Czettel, The effect of B and C addition on microstructure and mechanical properties of TiN hard coatings grown by chemical vapor deposition, *Thin Solid Films* 688 (2019) 137283.
- [46] T.H. Courtney, *Mechanical Behavior of Materials*, McGraw–Hill, Boston, 2000.
- [47] Y.X. Wang, S. Zhang, Toward hard yet tough ceramic coatings, *Surf. Coat. Technol.* 258 (2014) 1–16.
- [48] C. Kainz, N. Schalk, M. Tkadletz, C. Mitterer, C. Czettel, Microstructure and mechanical properties of CVD TiN/TiBN multilayer coatings, *Surf. Coat. Technol.* 370 (2019) 311–319.

- [49] D.G. Pettifor, Theoretical predictions of structure and related properties of intermetallics, *Mater. Sci. Technol.* 8 (1992) 345–349.
- [50] A. Zeilinger, J. Todt, C. Krywka, M. Müller, W. Ecker, B. Sartory, M. Meindlhumer, M. Stefanelli, R. Daniel, C. Mitterer, J. Keckes, In-situ Observation of Cross-Sectional Microstructural Changes and Stress Distributions in Fracturing TiN Thin Film during Nanoindentation, *Sci. Rep.* 6 (2016) 22670.
- [51] P.H.M. Böttger, L. Braginsky, V. Shklover, E. Lewin, J. Patscheider, D.G. Cahill, M. Sobiech, Hard wear-resistant coatings with anisotropic thermal conductivity for high thermal load applications, *J. Appl. Phys.* 116 (2014) 13507.
- [52] M.W. Chase, NIST-JANAF Thermochemical Tables: Fourth Edition, *J. Phys. Chem. Ref. Data*, Monograph 9, 1998, pp. 1–1951.
- [53] M.K. Samani, X.Z. Ding, N. Khosravian, B. Amin-Ahmadi, Y. Yi, G. Chen, E.C. Neyts, A. Bogaerts, B.K. Tay, Thermal conductivity of titanium nitride/titanium aluminum nitride multilayer coatings deposited by lateral rotating cathode arc, *Thin Solid Films* 578 (2015) 133–138.
- [54] S. Koseki, K. Inoue, S. Morito, T. Ohba, H. Usuki, Comparison of TiN-coated tools using CVD and PVD processes during continuous cutting of Ni-based superalloys, *Surf. Coat. Technol.* 283 (2015) 353–363.
- [55] T. Hori, J. Shiomi, Tuning phonon transport spectrum for better thermoelectric materials, *Sci. Technol. Adv. Mater.* 20 (2019) 10–25.

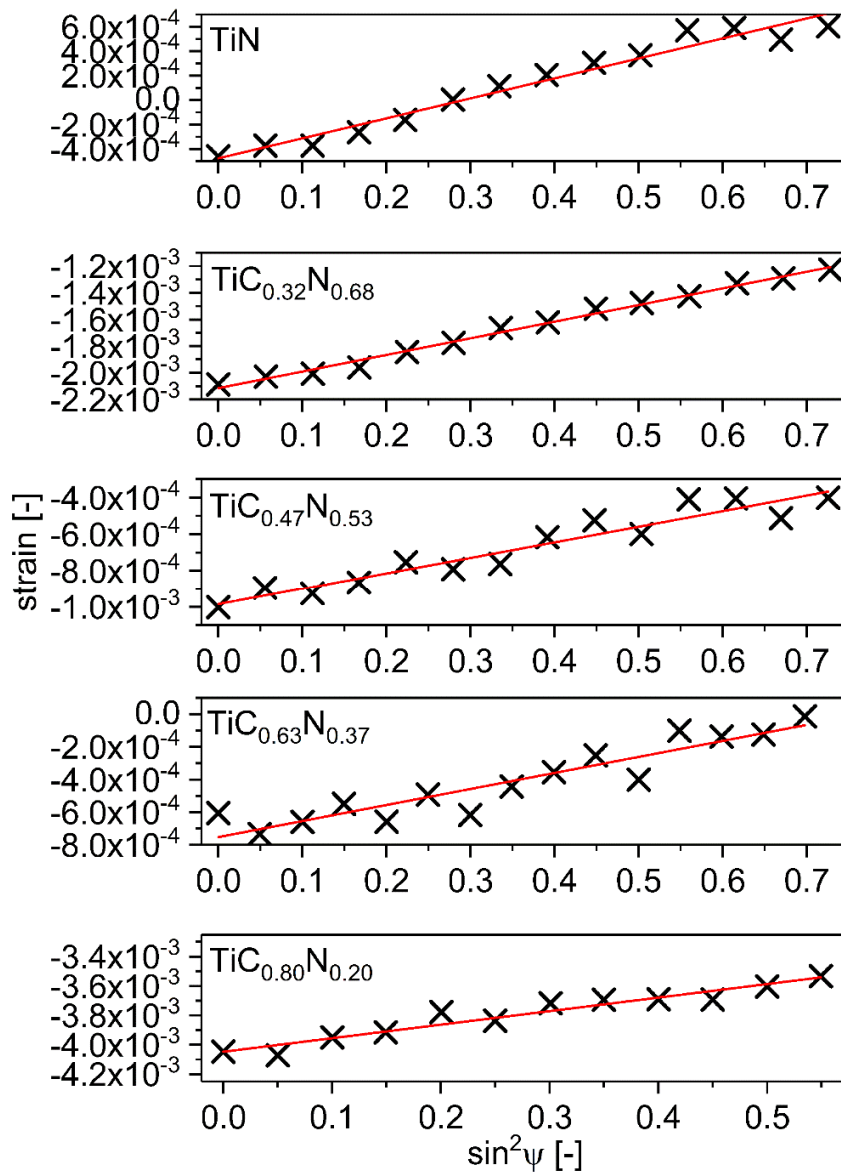
Supplementary material



Suppl. Fig. 1: Chemical composition versus sputter time as determined by GDOES for a) TiN, b) $TiC_{0.32}N_{0.68}$, c) $TiC_{0.47}N_{0.53}$, d) $TiC_{0.63}N_{0.37}$ and e) $TiC_{0.80}N_{0.20}$. The black dashed vertical line marks the interface between coating and substrate.



Suppl. Fig. 2: Pole figures of the 111, 200 and 220 reflections of the TiC_xN_{1-x} coatings quantified by multiples of random distribution (m.r.d).



Suppl. Fig. 3: $\sin^2\psi$ plots of the investigated coatings.